



UNIVERSIDAD DE INVESTIGACIÓN DE TECNOLOGÍA EXPERIMENTAL YACHAY

Escuela de Ciencias Físicas y Nanotecnología

TÍTULO: Fabrication and characterization of alumina/graphene-based ceramics via sol-gel and reactive spark plasma sintering method

Trabajo de integración curricular presentado como requisito para la obtención del título de Ingeniero en Nanotecnología

Autor:

Rios Andagoya Lady Jaqueline

Tutor:

Ph.D Vacacela Cristian

Co-Tutor:

Ph.D Zamora Ledezma Camilo

Urcuquí, Mayo 2020

SECRETARÍA GENERAL
(Vicerrectorado Académico/Cancillería)
ESCUELA DE CIENCIAS FÍSICAS Y NANOTECNOLOGÍA
CARRERA DE NANOTECNOLOGÍA
ACTA DE DEFENSA No. UITEY-PHY-2021-00008-AD

A los 2 días del mes de junio de 2021, a las 14:00 horas, de manera virtual mediante videoconferencia, y ante el Tribunal Calificador, integrado por los docentes:

Presidente Tribunal de Defensa	Dr. REINOSO CARLOS , Ph.D.
Miembro No Tutor	Dr. BRAMER ESCAMILLA , WERNER , Ph.D.
Tutor	Dr. VACACELA GOMEZ, CRISTIAN ISAAC , Ph.D.

El(la) señor(ita) estudiante **RIOS ANDAGOYA, LADY JAQUELINE**, con cédula de identidad No. **1719273011**, de la **ESCUELA DE CIENCIAS FÍSICAS Y NANOTECNOLOGÍA**, de la Carrera de **NANOTECNOLOGÍA**, aprobada por el Consejo de Educación Superior (CES), mediante Resolución **RPC-SO-13-No.156-2015**, realiza a través de videoconferencia, la sustentación de su trabajo de titulación denominado: **Fabrication and characterization of alumina/graphene-based ceramics via sol-gel and reactive spark plasma sintering method**, previa a la obtención del título de **INGENIERO/A EN NANOTECNOLOGÍA**.

El citado trabajo de titulación, fue debidamente aprobado por el(los) docente(s):

Tutor	Dr. VACACELA GOMEZ, CRISTIAN ISAAC , Ph.D.
Co - Tutor	Dr. ZAMORA LEDEZMA , CAMILO , Ph.D.

Y recibió las observaciones de los otros miembros del Tribunal Calificador, las mismas que han sido incorporadas por el(la) estudiante.

Previamente cumplidos los requisitos legales y reglamentarios, el trabajo de titulación fue sustentado por el(la) estudiante y examinado por los miembros del Tribunal Calificador. Escuchada la sustentación del trabajo de titulación a través de videoconferencia, que integró la exposición de el(la) estudiante sobre el contenido de la misma y las preguntas formuladas por los miembros del Tribunal, se califica la sustentación del trabajo de titulación con las siguientes calificaciones:

Tipo	Docente	Calificación
Presidente Tribunal De Defensa	Dr. REINOSO CARLOS , Ph.D.	8,7
Miembro Tribunal De Defensa	Dr. BRAMER ESCAMILLA , WERNER , Ph.D.	10,0
Tutor	Dr. VACACELA GOMEZ, CRISTIAN ISAAC , Ph.D.	10,0

Lo que da un promedio de: **9.6 (Nueve punto Seis)**, sobre 10 (diez), equivalente a: **APROBADO**

Para constancia de lo actuado, firman los miembros del Tribunal Calificador, el/la estudiante y el/la secretario ad-hoc.

Certifico que en cumplimiento del Decreto Ejecutivo 1017 de 16 de marzo de 2020, la defensa de trabajo de titulación (o examen de grado modalidad teórico práctica) se realizó vía virtual, por lo que las firmas de los miembros del Tribunal de Defensa de Grado, constan en forma digital.

RIOS ANDAGOYA, LADY JAQUELINE
Estudiante



Dr. REINOSO CARLOS , Ph.D.
Presidente Tribunal de Defensa

Digitally signed by CARLOS
 ALBERTO REINOSO JEREZ
 Date: 2021.06.02 15:20:29 COT

Dr. VACACELA GOMEZ, CRISTIAN ISAAC , Ph.D.
Tutor



Firmado electrónicamente por:
**CRISTIAN ISAAC
VACACELA GOMEZ**

Dr. BRAMER ESCAMILLA , WERNER , Ph.D.
Miembro No Tutor

WERNER
BRAMER
ESCAMILLA

Digitally signed by WERNER
BRAMER ESCAMILLA
Date: 2021.06.02 15:14:28
-05'00'

CIFUENTES TAFUR, EVELYN CAROLINA
Secretario Ad-hoc

EVELYN
CAROLINA
CIFUENTES
TAFUR

Digitally signed by
EVELYN CAROLINA
CIFUENTES TAFUR
Date: 2021.06.02
15:12:13 -05'00'

AUTORÍA

Yo, Lady Jaqueline Rios Andagoya, con cédula de identidad 1719273011, declaro que las ideas, juicios, valoraciones, interpretaciones, consultas bibliográficas, definiciones y conceptualizaciones expuestas en el presente trabajo; así cómo, los procedimientos y herramientas utilizadas en la investigación, son de absoluta responsabilidad de el/la autora (a) del trabajo de integración curricular. Así mismo, me acojo a los reglamentos internos de la Universidad de Investigación de Tecnología Experimental Yachay.

Urcuquí, mayo 2021.



Lady Jaqueline Rios Andagoya
1719273011

AUTORIZACIÓN DE PUBLICACIÓN

Yo, Lady Jaqueline Rios Andagoya, con cédula de identidad 1719273011, cedo a la Universidad de Investigación de Tecnología Experimental Yachay, los derechos de publicación de la presente obra, sin que deba haber un reconocimiento económico por este concepto. Declaro además que el texto del presente trabajo de titulación no podrá ser cedido a ninguna empresa editorial para su publicación u otros fines, sin contar previamente con la autorización escrita de la Universidad.

Asimismo, autorizo a la Universidad que realice la digitalización y publicación de este trabajo de integración curricular en el repositorio virtual, de conformidad a lo dispuesto en el Art. 144 de la Ley Orgánica de Educación Superior

Urcuquí, mayo 2021.



Lady Jaqueline Rios Andagoya
1719273011

Acknowledgement

At this point, I want to mainly thank God. For allowing me to achieve my dreams and be one of the first member in my family to get a third level degree. My parents and my sister, who were always believed in me and never let me give up. To my family in general, who was there motivating me. I want to thank all my teachers who were part of who I am, Dr. Sarah Briceño, Dra. Gema González, Dr. Werner Escamilla, Dr. Julio Chacón, Dr. Cristian Vacacela and especially my co-tutor Camilo Zamora Ledezma.

I reiterate my thanks to the University of Seville, Dr. Víctor Morales, Msc. Pedro Rivero for allowing me to be a part of this incredible work. Dr. Erick Anglaret, Dr. Juan Moreno who contributed their insights in Raman and XPS. And, Dr. Carlos Reinoso for having contributed to the XPS measurement.

Finally, thanks to all my friends for making university one of the best stages of my life, Dany Quiroz, Danna Castillo, Angie Changuán, Andrea Valenzuela, Cristina Picón, Carolina Ibarra.

Resumen

La fabricación de compuestos de matriz cerámica avanzada (CMC) con fases alótropas de carbono de baja dimensión es actualmente un tema de investigación abierto. Uno de los desafíos modernos permanentes para superar los problemas experimentales comunes, con respecto a la homogeneidad de la dispersión de nanocarbonos, su ubicación dentro de la matriz cerámica y el tipo de unión entre el relleno y la matriz. Este trabajo presenta la fabricación de compuestos de matriz cerámica de alúmina/grafeno completamente densos por la ruta sol-gel y sinterización de plasma de chispa reactiva, como una metodología alternativa para mejorar la dispersión de las capas de grafeno dentro del compuesto y promover la formación de enlaces de fuertes entre las capas de grafeno y la matriz cerámica, como los puentes de oxígeno Al-O-C. Las micro/nano estructuras son investigadas por: fisisorción de nitrógeno, espectroscopía Raman, microscopía electrónica y espectroscopía fotoelectrónica de rayos X (XPS). Las observaciones de SEM revelaron la ausencia de aglomeraciones de grafeno, lo que sugiere la eficacia de este método de fabricación. Los análisis Raman han confirmado la integridad del grafeno a lo largo del proceso de fabricación. Se midieron características mecánicas como la dureza y la tenacidad a la fractura por indentación para diferentes contenidos de grafeno. Nuestros resultados se comparan con los de las CMC convencionales de alúmina/grafeno y sugieren que el enfoque actual ofrecería una ruta atractiva para fabricar cerámicas reforzadas a base de alúmina/nanocarbono.

Palabras clave: Óxido de Grafeno, XPS, Raman, propiedades mecánicas, boehmita, $\alpha\text{-Al}_2\text{O}_3$

Abstract

The fabrication of advanced ceramic matrix composites (CMCs) with low-dimensional carbon allotropes phases is currently an open research topic. One of the modern challenges still remains to overcome common experimental issues, regarding the homogeneity of the nanocarbon dispersion, their location within the ceramic matrix, and the type of bonding between the filler and the matrix. This work introduces the fabrication of fully-dense alumina/graphene ceramic matrix composites by the sol-gel route and reactive spark plasma sintering, as an alternative methodology to improve the dispersion of the graphene flakes within the composite, and to promote the formation of strong bonds between graphene flakes and the ceramic matrix such as Al-O-C oxygen bridges. The micro/nano structures are researched by: nitrogen physisorption, Raman spectroscopy, electron microscopy and X-ray Photoelectron Spectroscopy (XPS). SEM observations revealed the absence of graphene agglomerations suggesting the efficacy of this fabrication approach. Raman analyses have confirmed the integrity of the graphene along the fabrication process. Mechanical features such as hardness, and indentation fracture toughness were measured for different graphene contents. Our results are compared with those from conventional alumina/graphene CMCs, and suggest that the current approach would offer an appealing route to fabricate reinforced alumina/nanocarbon based ceramics.

Keywords: Graphene oxide, XPS, Raman, mechanical properties, boehmite, $\alpha - Al_2O_3$.

Contents

List of Figures	ix
List of Tables	xv
1 Introduction	1
2 Theoretical Framework	5
2.1 Ceramics	5
2.1.1 Types of ceramics	6
2.1.2 Zirconia ceramics	7
2.1.3 Alumina ceramics	8
2.1.4 Mechanical properties of Zirconia and Alumina ceramics	10
2.1.5 Types of nanofillers in ceramic composites	11
2.1.6 Carbon nanotubes and graphene based ceramic matrix composites	12
2.2 Graphene	14
2.2.1 Graphene oxide and reduced graphene oxide	16
2.2.2 Electronic band structure of graphene	17
2.2.3 Graphene based materials functionalization	18
2.3 Characterization and sample preparation techniques	20
2.3.1 Sol-gel processing	20
2.3.2 Spark plasma sintering (SPS)	21
2.3.3 X-ray diffraction (XRD)	23
2.3.4 Thermogravimetry analysis (TGA)	24

2.3.5	<i>N</i> ₂ Physisorption	25
2.3.6	Density	26
2.3.7	Scanning Electron Microscopy (SEM)	27
2.3.8	Raman	29
2.3.9	X-ray Photoelectron spectroscopy (XPS)	35
2.3.10	Mechanical characterization	37
3	Methodology	39
3.1	Synthesis of alumina/graphene oxides composites	39
3.1.1	Materials	39
3.1.2	Graphene/Alumina Ceramics Matrix Composite (GCMC) Fabrication and Optimization	40
3.1.3	Sample preparation for mechanical properties analysis	41
3.2	Characterization techniques	42
3.2.1	X-ray Diffraction	42
3.2.2	Thermogravimetric Analyses	43
3.2.3	<i>N</i> ₂ Physisorption	43
3.2.4	Densities	43
3.2.5	Scanning Electron Microscopy	43
3.2.6	Raman spectroscopy	44
3.2.7	X-ray photoelectron spectroscopy	45
3.2.8	Mechanical properties	45
4	Results & Discussion	47
4.1	Characterization equipment	47
4.1.1	X-ray Diffraction	47
4.1.2	Thermogravimetric Analysis	49
4.1.3	Nitrogen physisorption analysis	51
4.1.4	Densities	53
4.1.5	Scanning Electron Microscopy	54
4.1.6	Raman spectroscopy	57
4.1.7	X-ray Photoelectron Spectroscopy	62

4.1.8 Mechanical properties	66
5 Conclusions & Outlook	69
A Short Appendix 1 Heading for the Table of Contents	71
Bibliography	79

List of Figures

2.1	Application of advanced ceramics ¹	6
2.2	Types of ceramics depending on the oxide group and their applications ²	7
2.3	Zirconia tetragonal phase, temperature is above 1170°C. (a) Tetragonal unit cell (b) Representation of two layers of ZrO_2 (Built with Avogadro editor).	8
2.4	(a) Conventional hexagonal unit cell of $\alpha-Al_2O_3$ (b) Representation of two layers of $\alpha-Al_2O_3$ (Built with Avogadro editor)	9
2.5	Common calcination routes of bohemite aluminum hydroxites and crystal phases of aluminum oxide toward to formation of corundum ^{3,4}	10
2.6	Schematic representation of nanofillers types. Modified sketch from Inam et al. ⁵ .	12
2.7	Schematic representation of graphene nanomaterial. At the top-left part, carbon with sp^2 hybridized orbitals at the x-y plane. At the top-right part, the graphene network using Avogadro to show the hexagonal arrangement and the unit cell . .	15
2.8	Schematic diagram of the lattice structure of Graphene, Graphene Oxide, and reduced Graphene Oxide using Avogadro ⁶	16
2.9	(a) Schematic diagram of lattice structure and valence/conductive Dirac cones at the K points of the hexagonal lattice in reciprocal space at the Fermi level using Avogadro and Mathematica program. (b) Energy band diagrams of Graphene, GO, and rGO using Avogadro. VB (valence band), CB (conduction band) ^{6,7} . .	18
2.10	Recent progress of Graphene based ceramic matrix composite (GCMC). Modified sketch from Markandan et al. ⁸	19
2.11	Schematic representation of sol-gel processing. Modified sketch from Dervin et al. ⁹	21
2.12	Diagram of spark plasma sintering	22

2.13	Schematic diagram of X-ray diffraction (XRD) Modified from Epp et al. ¹⁰ . X-ray diffraction image of crystallized DNA ¹¹	23
2.14	The principle of Brag’s law from lattice planes ¹⁰	24
2.15	Schematic representation of idealized physisorption model	25
2.16	Schematic representation of Archimedes method density measurements (a) sample weighed in the air (reference) (b) sample weighed in fluid. Modified from Arvieu et al. ¹²	26
2.17	Schematic diagram of scanning electron microscopy (SEM). Signals generated by electron beam-specimen interaction: EDX nergy-dispersive X-ray spectroscopy, BSE backscattered electrons, and SE secondary electrons Modified from Shah et al. ¹³	28
2.18	Basic principle of Raman spectroscopy (a) Schematic representation of Raman principle (b) Quantum Energy transitions diagram for Rayleigh and Raman scattering ¹⁴	30
2.19	Stokes and Anti-stokes Raman spectral lines of chloroform obtained with 514.5 nm excitation ¹⁵	31
2.20	Schematic diagram of Raman spectroscopy. Modified sketch from ¹⁶	32
2.21	Raman vibrational modes of graphene for G, D, and G’ peak ¹⁷	33
2.22	Schematic diagram of first order Raman scattering process (G band) and double resonance Raman scattering (D, D’, G’) in graphene	34
2.23	Schematic view of photoelectron emitted by incident x-ray photon.	35
2.24	Schematic diagram of X-ray photoelectron spectroscopy process.	36
2.25	Schematic representation of Vicker Indentation test and illustration of the two indentation diagonals d_1 and d_2 . Modificated from Alhashmy, Hasan ¹⁸	37
2.26	The optical image from Vickers identation,in which is observed the cracks emerging from print corners. "c" is the crack length for K_{Ic} ¹⁹	38
3.1	Schematic synthesis process of graphene ceramic matrix composite (GCMC), followed the procedure reported by Rivero-Antunez et al ¹⁹	41
3.2	Schematic representation of RCEP preparation protocol.	42
3.3	Raman equipment at Yachay Tech University	44
3.4	XPS equipment at Yachay Tech University	45

4.1	Selected X-ray powder diffraction patterns, from bottom to top: i.- as-received graphene oxide (Gs) and ii.- GRAL3-s sintered samples with 3 wt.% Gs content respectively. The stable crystalline phase $\alpha\text{-Al}_2\text{O}_3$ (corundum) is observed and follows the pattern diffraction file: $\alpha\text{-Al}_2\text{O}_3$, PDF: 00-043-1484	48
4.2	Typical Thermogravimetric analysis curves in (a-b) argon atmosphere and (c) under oxidative air atmosphere for: (a) as received graphene oxide flakes (Gs) at two different temperature rates of 2°C and 10°C respectively, (b) boehmite/graphene composites powder GRAL2-p and GRAL2@1050-p (where the label @1050 indicates that the sample was subjected to a pre calcination process at 1050°C in argon) and (c) boehmite/graphene composites GRAL2-p under oxidative atmosphere, where the weight losses due to the burnout of the carbon of the samples is observed and comparable to the expected carbon content.	50
4.3	Adsorption isotherms of N ₂ at 77 °C for the boehmite/graphene matrix composites powders (GCMC-p) series fabricated by the sol-gel method	52
4.4	Scanning Electron Microscopy (SEM) of representative scanning electron microscopy (SEM) images for (a) as received graphene oxide flakes (Gs) and (b) composite xerogel powder GRAL6-p fabricated by the sol-gel method	54
4.5	Representative scanning electron microscopy (SEM) images for sintered samples from top to bottom: (a) GRAL0-s, (b) GRAL2-s and (c) GRAL6-s with 0, 2 and 6 wt.% Gs content respectively. All samples exhibit fine-micro-grained-like characteristics of stable crystalline phase $\alpha\text{-Al}_2\text{O}_3$ (corundum).	56
4.6	Raman spectra for the composite powder GRALX-p series fabricated by the sol-gel method excited with both green and red laser lines (X denotes the graphene solid content percentage within the sample). Spectra were normalized with respect to the boehmite(AlO(OH)) peak. D, G and 2D bands are marked. All spectra were shifted along the Y axis for clarity.	58
4.7	Raman peak intensities I_G/I_{boeh} ratios as a function of the Gs wt.% in the boehmite/graphene powder composites GRALX-p for 532 nm and 633 nm excitation wavelengths laser	59

4.8	Raman spectra for the sintered ceramic GRALX-s series fabricated by the sol-gel method and reactive spark plasma sintering (rSPS), excited with both green and red laser lines (X denotes the graphene solid content percentage within the samples). Spectra were normalized with respect to the $\alpha - Al_2O_3$ peak. D, G and 2D bands and the relevant bands for $\alpha - Al_2O_3$ and Cr^{+3} ions (R1 and R2) are marked. All spectra were shifted along the Y axis for clarity	61
4.9	X-ray photoelectron spectroscopy spectrum for three precursor elements and the GCMC (a) general survey of the precursor and powder samples with different graphene content, (b) Al 2p spectrum of GRAL with 0% graphene (c) Al 2p spectrum of GRAL with 2% graphene, (d) O1s spectrum of GRAL with 0% graphene (e) O1s spectrum of GRAL with 2% graphene	63
4.10	X-ray photoelectron spectroscopy spectrum for sintered samples, (a) Al 2p spectrum of GRAL with 0% graphene (c) Al 2p spectrum of GRAL with 2% graphene, (d) O1s spectrum of GRAL with 0% graphene (e) O1s spectrum of GRAL with 2% graphene	65
4.11	Vickers hardness for the GCMC sintered samples series. Error bars correspond with the standard deviation.	66
4.12	Indentation fracture toughness of GCMC sintered samples series calculated with Shetty's equation using a Young's modulus of pure alumina from literature (E=400 GPa). Error bars correspond with the standard deviation.	67
A.1	Macroscopic pictures of boehmite/graphene composites powders: (a) before, (b) after calcination in argon atmosphere at 1200°C. Graphene oxide content in the sample researched corresponds with 1 wt.% and labeled as GRAL1-p	71
A.2	XRD patterns for alumina/graphene ceramic matrix composites (GCMC) series GRALX-s. (X denotes the Gs wt.%). The stable crystalline phase $\alpha - Al_2O_3$ (corundum) is observed and follows the pattern diffraction file: $\alpha - Al_2O_3$, PDF: 00-043-1484	72

A.3	Representative Raman powders spectra for: as received (a) Graphene Oxide flakes (Gs), (b) Boehmite and (c) Seeds of $\alpha\text{-Al}_2\text{O}_3$. For the sake of clarity in (d), Raman spectra of $\alpha\text{-Al}_2\text{O}_3$ on absolute wavelength is shown. D, G, G' and the relevant bands for Cr^{+3} ions (R1 and R2) are marked. All spectra were excited with both green and red laser lines ($\lambda = 532$ nm and $\lambda = 633$ nm), normalized either by the G band of graphene or the boehmite band, as well as shifted along the Y axis for clarity.	73
A.4	Typical Raman powders spectra for the composite xerogel powder GRAL0-p fabricated by the sol-gel method. Boehmite and the relevant bands for Cr^{+3} ions (R1 and R2) are marked. All spectra were excited with both green and red laser lines ($\lambda = 532$ nm and $\lambda = 633$ nm), normalized by the boehmite band and shifted along the Y axis for clarity.	74
A.5	XPS C1s spectrum for GRAL0-s and GRAL2-s.	75

List of Tables

2.1	Physical and mechanical properties Alumina and Zirconia- Y_2O_3 ^{20 21}	11
2.2	Theoretical and experimental properties of CNT and Graphene ^{22 23}	13
2.3	Theoretical and experimental properties of CNT and Graphene based ceramic matrix composites ^{22 23}	14
4.1	Specific surface area (S_{BET}), pore size diameter (D_p) and volume (V_p) obtained by nitrogen physisorption experiments for the boehmite/graphene matrix composites (GBMC-p) powders series fabricated by the sol-gel method	51
4.2	Theoretical bulk density and relative density of all synthered GCMC ceramics at different Gs content obtained through the Archimedes method	53
4.3	Intensities I_D/I_G and I_{2D}/I_G ratios for Raman peaks of Bohemite/graphene composites at 532 nm and 633 nm laser	59
4.4	Raman peak intensities I_G/I_{Alu} ratios as a function of the Gs wt.% in the alumina/graphene sintered composites ceramics GRALX-p for 532 nm excitation wavelengths laser	61
A.1	Atomic percentage of precursor elements	76
A.2	Atomic percentage of powders samples	76
A.3	Atomic percentage of sintered samples	77
A.4	Detail information of typical XPS results of Al2p, and O1s spectra of sintered samples: binding energy, peak width, and content percentage.	77

Chapter 1

Introduction

Advanced ceramics exhibits attractive properties to solve a wide number of modern challenges in areas ranging from power generation to aerospace, biomedical, electronical, industrial and military applications⁸. The majority of these applications require specific properties like high stiffness, strength and stability at high temperatures^{24,25}. To date, the characteristic features of bare ceramics such as their low fracture toughness, poor mechanical reliability, and low electrical conductivity have limited many of their potential applications and are the driving force behind research in this area^{24,26}, and they are the driving force of promoting further research on this area. Due to the intrinsic physico-chemical and mechanical characteristics, low density, inertness, biocompatibility, availability and its relatively inexpensive nature, Al_2O_3 is the most common and versatile existing oxide used in ceramics applications. The main fabrication routes of such materials will depend on their final useage. It may vary quite significantly and include the following: sinterization under high temperature and pressure conditions, extrusion, dry pressing, pressure casting, isostatic pressing among others^{25,24}. The final performance of such alumina-based materials ceramics strongly depends on the impurity content, which can be found on the initial precursor or added as special additives. In most cases, these additives lead to unprecedented physico-chemical improvements, decreases in sintering temperatures, simplifying the fabrication process and its associated costs. Depending on the application, additives such as: magnesium oxide (MgO), zirconium dioxide (ZrO_2), titanium dioxide (TiO_2) or synthetic nanoparticles such as nanocarbons had been used in the last decades, promoting the modulation of their final performance^{27,19}. However, their fabrication mechanism is still under debate, and

it has presented several obstacles regarding the serious difficulties for obtaining well-dispersed and homogeneously distributed additives within the matrix. The fabrication of ceramic materials based on aluminum oxides, with low dimensional carbon allotropes such as carbon nanotubes (CNT), graphene, and other 2D materials has also gained considerable attention in the last decade^{28,27,19}. It suffers as well, similar disadvantages regarding the dispersion and homogeneity of the carbonaceous phase during the ceramic processing. In fact, carbon nanotubes are highly hydrophobic, and spontaneously insoluble in organic solvents, due mainly to their strong Van der Waals interactions^{29,30}. In this context, ceramics matrix composites (CMC) through the sol-gel technique appear as a modern alternative and have proven to be an extremely useful route to produce novel ceramics with tailored physico-chemical properties^{24,27,19}. Rivero-Antunez et al. reported recently remarkable mechanical properties improvements by reinforcing CMC with carbon nanotubes (CNTs)^{27,19}. This reinforcement was attributed mainly to the intrinsic CNTs exceptional mechanical properties such as Young's modulus, or tensile strength combined with the intragranular location within the ceramic, allowing to overcome the previously mentioned fragility. Similarly, Leonov et al. reported well dispersed carbon nanotubes in alumina composites, which enhanced the fracture toughness and microhardness around 4.93 MPam^{1/2} and 23.26 GPa respectively³¹ if compared with 3.5 MPam^{1/2} of the bare alumina³². In the same context, Guo et al. reported homogenous dispersion of carbon nanotubes in alumina matrix composites, by controlling the interfacial bonding of hydroxyl and carbonyl groups between the tubes and the matrix. Mechanical properties comparable to those reported in the literature⁴. Likewise, graphene flakes have drawn special attention as additives in aluminum oxide based ceramic composites, due to their outstanding electrical, mechanical, and thermal properties²⁴. Furthermore, the dispersion and homogeneity of graphene could be readily controlled, thanks to their vast reactive surface area, avoiding the tendency to agglomerate during processing³³. In addition, the modern technological advances allow the production of large quantities of high-quality graphene nanoparticles at lower prices, making them more suitable for industrial applications³⁴. Thus, graphene not only offers better performance, but also affordable prices and lower health hazards compared to CNT which often possesses harmful catalyst residues used during their synthesis³⁵. These characteristic features make them suitable for a broad range of industrial and biomedical applications, such as sensors³⁴, ultracapacitors³⁶, shielding³⁷, and ceramic composites among others^{38,39,40,41,42,43}. Recently, Shah et al. reported the fabrication of graphene-reinforced Al_2O_3 -matrix by the physical

dispersion method. They reported substantial improvement of the mechanical properties at low content of graphene with densities approaching 98%, and discussed the strengthening and toughening mechanisms of graphene in the alumina matrix. However they focus only in a low graphene content regime⁴⁴ Moreover, Dasari et al. achieved homogeneous distribution of graphene in alumina composites via liquid phase mixing and powder metallurgy, obtaining mechanical properties comparable to those reported previously in the literature and mainly due to the strength and stiffness properties of graphene⁴⁵. For its part, Hrubovčáková et al. reported the preparation of conductive Al_2O_3 /few layer graphene composites. They use graphene synthesized onto the alumina particles by a one-step Chemical Vapor Deposition (CVD) method. They reported interesting electrical properties accompanied by a slight decrease of the mechanical properties such as elastic modulus and hardness⁴⁶. Zhou et al. very recently published an interesting review where they propose a fresh look about the current progress in the fabrication of ceramic matrix composites reinforced with graphene. They also devote an important part of this work to the processing methods to control the graphene dispersion throughout the ceramic matrices, and the reduction of the porosity through fully dense materials⁴⁷. Thus, there remain many challenges that should be addressed in the future, such as the improvement of the processing techniques in order to enhance the performance of graphene based ceramics.

In this work, we present the fabrication of fully-dense alumina/graphene ceramic matrix composites (GCMC), by the sol-gel (SG) route and reactive spark plasma sintering (rSPS), as an alternative methodology to improve the graphene flakes (Gs) dispersion within the composite, and to promote the formation of strong bonds between Gs and the ceramic matrix such as Al-O-C oxygen bridges. The micro/nano structure of these composites are researched by: nitrogen physisorption, Raman spectroscopy, electron microscopy and X-ray Photoelectron Spectroscopy (XPS). Mechanical features such as hardness, Young's modulus and indentation fracture toughness are studied for different graphene contents.

Chapter 2

Theoretical Framework

2.1 Ceramics

Ceramics are defined as inorganic, nonmetallic materials made up of ionic, covalent, or mixed bonds⁴⁸. In comparison with metals and allied materials, ceramics can exhibit exceptional properties in terms of low density, hardness (according to Mohs scale, the hardness of corundum is around 9), thermal stability, corrosion and wear resistance⁴⁹, high stiffness and strength, low thermal expansion coefficient (high-temperature resistance), and high resistance against moisture⁵⁰. Making useful in a variety of technologies and in very different industrial sectors²⁷. Specifically, they are considered as a material for aerospace, biomedical, electronic, automotive¹, and other high-temperature applications like advanced tactical missiles for military defense⁵⁰ as shown in Fig.2.1.

Ceramics are expected for usages at medium to high temperatures (often $>550^{\circ}\text{C}$) in high stresses and oxidizing or corrosive atmosphere^{49,48}. Among this group of high temperature ceramics, those with melting point $>3000^{\circ}\text{C}$ is called Ultra High Temperature Ceramics (UHTCs)^{48,51}. These kinds of ceramics are used at temperatures above $\sim 2000^{\circ}\text{C}$ in air, and under aggressive aerodynamic conditions^{48,51}.

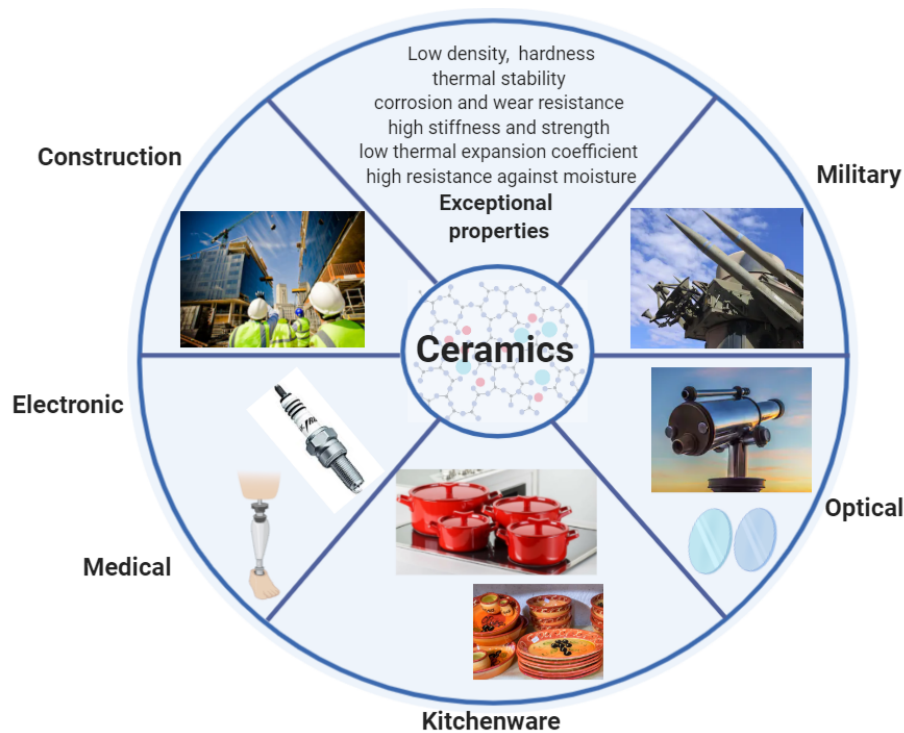


Figure 2.1: Application of advanced ceramics¹.

2.1.1 Types of ceramics

As shown in Fig. 2.2, we could have seven types of ceramics². During this work, we are discussing inert oxides ceramics. An inert ceramic is employed as a biomaterial for medical devices, due to it not form bonding to the bone. These kinds of ceramics present high mechanical properties as compressive and tensile strengths, hardness, toughness, low wear, and good corrosion resistance against the biological medium. They are used in total hip and knee replacements, dental implants, dental crowns, etc.². In this group of inert ceramics, we may find zirconia and alumina ceramics. Zirconia bioceramics are partially stabilized by additional oxides, e.g. yttrium oxide, calcium oxide, or magnesium oxide, whereas alumina bioceramics are in the pure aluminum oxide form⁵². Alumina or aluminum oxide-based composite are most used for joint replacement due to their better compatibility with human cells²¹. Nowadays, most commercial medical devices are alumina stabilized with zirconia-based composite².

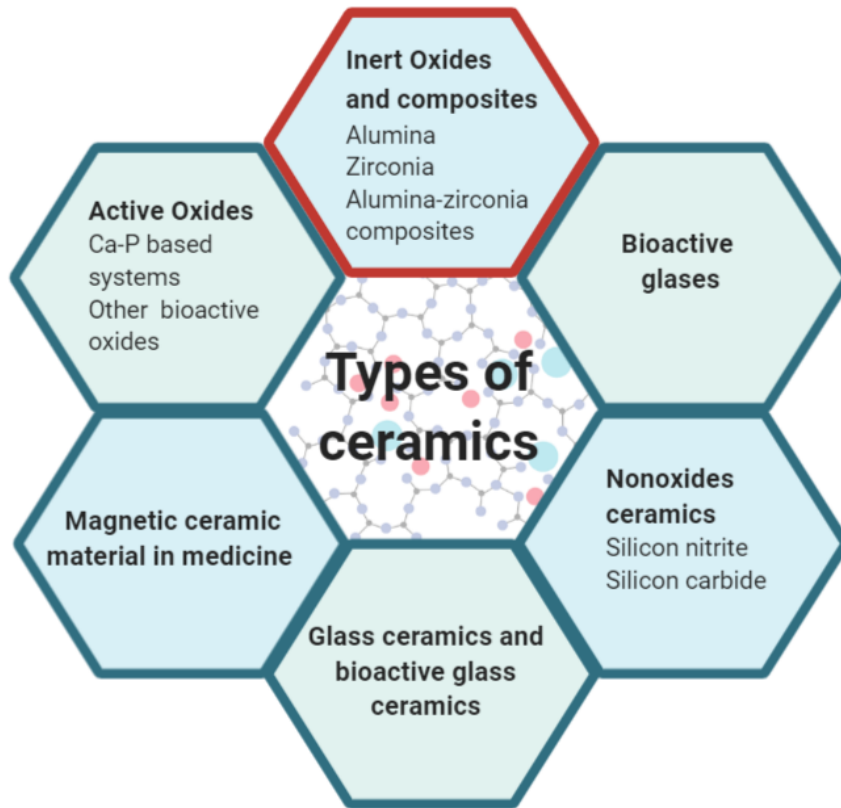


Figure 2.2: Types of ceramics depending on the oxide group and their applications²

2.1.2 Zirconia ceramics

Zirconia, the crystalline dioxide of zirconium (ZrO_2) was discovered in 1789 by the German chemist Martin Heinrich Klaproth. This ceramic has a good chemical, dimensional stability²⁰, and the highest mechanical properties that are very similar to other metals². The origin of using zirconia as a ceramic biomaterial is due to it has mechanical properties similar to stainless steel alloys. The compression resistance of ZrO_2 is about 2000 MPa²⁰. ZrO_2 represented a new generation of implants, the first use for medical purposes was made in 1969. ZrO_2 was proposed as a new material for hip head prostheses⁵³. Also, it is proposed for medical devices like orthodontic brackets, dental implants, or dental restoration². In order to understand the mechanical properties of zirconia, it is essential to describe its atomic structure. At atmospheric pressure, zirconia

crystal can be organized in three different patterns depending on temperature, (i) monoclinic (*m*) at room temperature (ii) tetragonal (*t*) above 1170°C and (iii) cubic above 2370°C. The sintering temperature is $\sim 1400\text{-}1450^\circ\text{C}^2$. ZrO_2 stabilized with Y_2O_3 , called Tetragonal Zirconia Polycrystals (Y-TZP), it has better mechanical performance than other combinations⁵³, which exhibits the highest strength (1000-1200 MPa) and toughness (9MPa). It has a better subcritical crack propagation resistance than alumina².

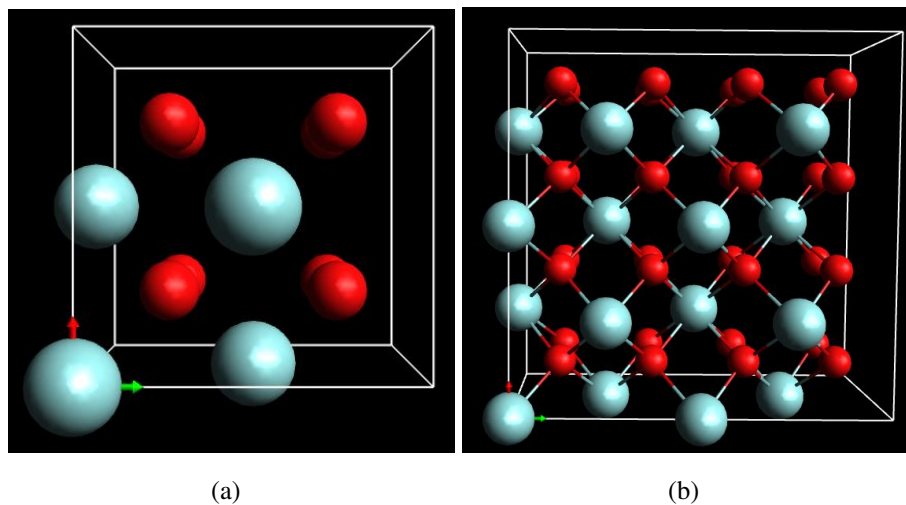


Figure 2.3: Zirconia tetragonal phase, temperature is above 1170°C. (a) Tetragonal unit cell (b) Representation of two layers of ZrO_2 (Built with Avogadro editor).

2.1.3 Alumina ceramics

Alumina is the first oxide material developed for medical devices². In 1970, Dr Pierre Boutin implanted the first hip prostheses with Al_2O_3 ceramics bearings²¹. His success led to include some patents of Al_2O_3 , recognizing this polycrystalline bioceramic as a viable orthopedic material^{54, 55, 56}.

Aluminum oxide (boehmite) has various crystal types, such as α -, γ -, ρ -, η -, σ -, θ -, κ -, χ - Al_2O_3 . Among of them, the mainly used in industries are γ -, ρ - and α - types⁴.

Depending on the crystal phase, we can have different applications. For example, the γ phase provides a large surface due to its porous structure and we may use it in the reduction of automotive

pollutants, absorbents, and oil refining³. In this case, we will emphasize the α -crystallographic phase of aluminum oxide ($\alpha\text{-Al}_2\text{O}_3$) called corundum³. Corundum has low electrical conductivity⁵⁷, high electrical and temperature resistance, high wear and corrosion resistance³, excellent biocompatibility⁵⁸, and good mechanical properties such as high hardness (superior 20 GPa)². It is one of the most important ceramics for technological and biomedical applications like spark plugs⁵⁹, brine pumps⁶⁰, thermocouple tubes⁶¹, and prostheses⁵⁸. Unfortunately, the slow crack growth in alumina with time in service was reported as a significant in-vivo failure by the orthopedic community⁵⁸. As we can see in the Figure.2.4, $\alpha\text{-Al}_2\text{O}_3$ is linked to its close-packed hexagonal crystal structure with strong ionic and covalent bonds between atoms². This structure induce a high melting temperature and consequently a fabrication of parts by sintering at relatively high temperatures (1500-1600°C)².

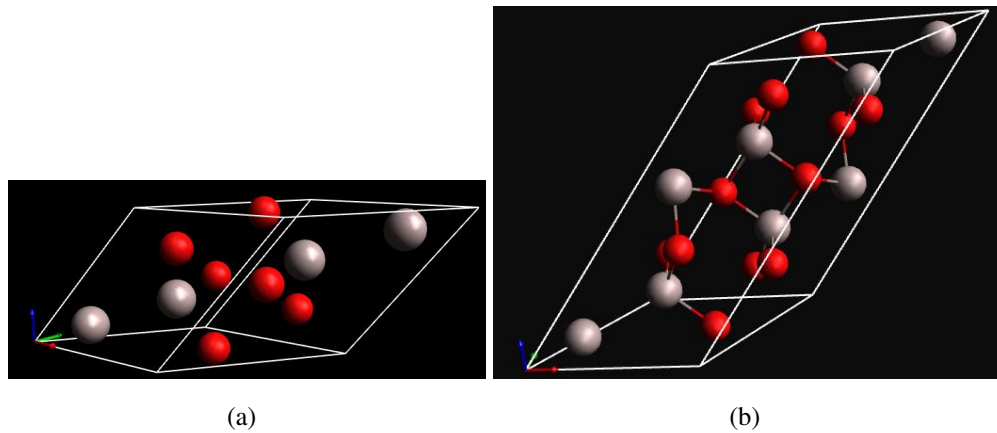


Figure 2.4: (a) Conventional hexagonal unit cell of $\alpha\text{-Al}_2\text{O}_3$ (b) Representation of two layers of $\alpha\text{-Al}_2\text{O}_3$ (Built with Avogadro editor)

Is important to mention that, different crystal types of Aluminium oxide came from thermal dehydration of aluminum hydroxides ($\text{Al}(\text{OH})_3$) at specific temperatures for each case⁴. Aluminum hydroxides has a family of seven compounds. akdalaite (tohdite), bayerite, boehmite, diaspore, doyleite, gibbsite and nordstrandite³. In the present work, we are going to obtain $\alpha\text{-Al}_2\text{O}_3$ from aluminum hydroxides bohemite ($\gamma\text{-AlO}(\text{OH})$).

Bohemita sol-gels

The fabrication of $\alpha\text{-Al}_2\text{O}_3$ from bohemite ($\gamma\text{-AlO(OH)}$) sol gels has been studied for many years⁶². Bohemite behaves as precursor of alumina α phases which are formed during calcination process³, as we can see in the Figure.2.5:

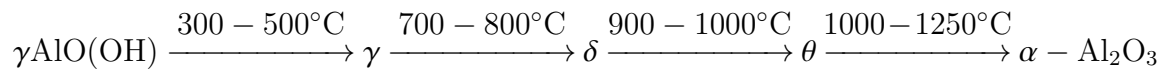


Figure 2.5: Common calcination routes of bohemite aluminum hydroxites and crystal phases of aluminum oxide toward to formation of corundum^{3,4}.

We need to employ thermal dehydration of Al(OH)_3 at high temperature (1000-1250°) to obtain the dense and stable $\alpha\text{-Al}_2\text{O}_3$ ^{63,64}. In order to improve the transformation from γ to $\alpha\text{-Al}_2\text{O}_3$ we may use an additive of $\alpha\text{-Al}_2\text{O}_3$ seeded bohemite sol-gel. A number of researchers report that each $\alpha\text{-Al}_2\text{O}_3$ seed provide multiple nucleation sites for the θ to $\alpha\text{Al}_2\text{O}_3$ transformation. These exhibit the formation of a uniform, fine grained $\alpha\text{Al}_2\text{O}_3$ microstructure, which sinters uniformly at reduced temperatures and times compared to unseeded transitional aluminas⁶².

2.1.4 Mechanical properties of Zirconia and Alumina ceramics

Now, if we made a comparison of the mechanical properties between Zirconia and Alumina from inert oxides using Table.2.1 We observe that TZP may perform better than Al_2O_3 for medical purposes. Alumina has relatively modest fracture strength and toughness, both of these increase the risk of brittle failure²¹.

Despite the fact that Alumina is not good for biomedical applications, it is a promising structural material with wear and corrosion resistance, high strength, and stiffness at high temperatures⁶⁵. They are still brittle, low electrical conductivity⁸, and fracture toughness³¹. However, to our knowledge, there is some report on the use of nanofillers additives to improve the mechanical properties of bulk ceramics.

Property	Units	Tetragonal Zirconia Polycrystal (TZP)	Alumina (Al_2O_3)
Chemical composition		ZrO_2 +3 mol% Y_2O_3	99.9 % Al_2O_3 +MgO
Density	$g\ cm^{-3}$	≥ 6	3.98
Porosity	%	<0.1	<0.1
Bending strength	M Pa	900-1200	>500
Compression strength	M Pa	2000	4100
Young modulus	G Pa	210	380
Fracture toughness	M Pa m^{-1}	7 - 10	4
Thermal expansion coeff.	K	11×10^{-6}	8×10^{-6}
Thermal conductivity	W mK^{-1}	2	30
Hardness	GPa	11 - 12.5	18 - 23

Table 2.1: Physical and mechanical properties Alumina and Zirconia- Y_2O_3 ^{20,21}

2.1.5 Types of nanofillers in ceramic composites

Over the last two decades and with the worldwide interest in nanotechnology, scientific and commercial communities are fascinated by nanocomposites and nanofillers applications.

Nanofillers are defined as fillers with particle sizes in the 1–100 nm range⁶⁶. Which are dispersed into the composite matrix to improve the functional properties of the composite. They have been widely researched for their addition in polymers⁶⁷, ceramic⁶⁸ and metal⁶⁹ nanocomposites. Nanofillers are mainly classified according to their dimensions, as we can see in Fig. 2.6 Nanoplates are restricted to one nano dimension. Those with two dimensions are described as nanofibers, and finally, those with three dimensions as nanoparticles. As far as we know, ceramic matrix composite (CMCs) are especially filled with carbon nanofillers in previous works¹. Which are researched for emerging applications like electronics, sensors, photovoltaic devices⁷⁰, aerospace, transportation, and infrastructure sectors⁵. Particularly, CNTs and graphene have been reported in the last decade to significantly improve mechanical, thermal, and electrical properties in ceramic composites⁵.

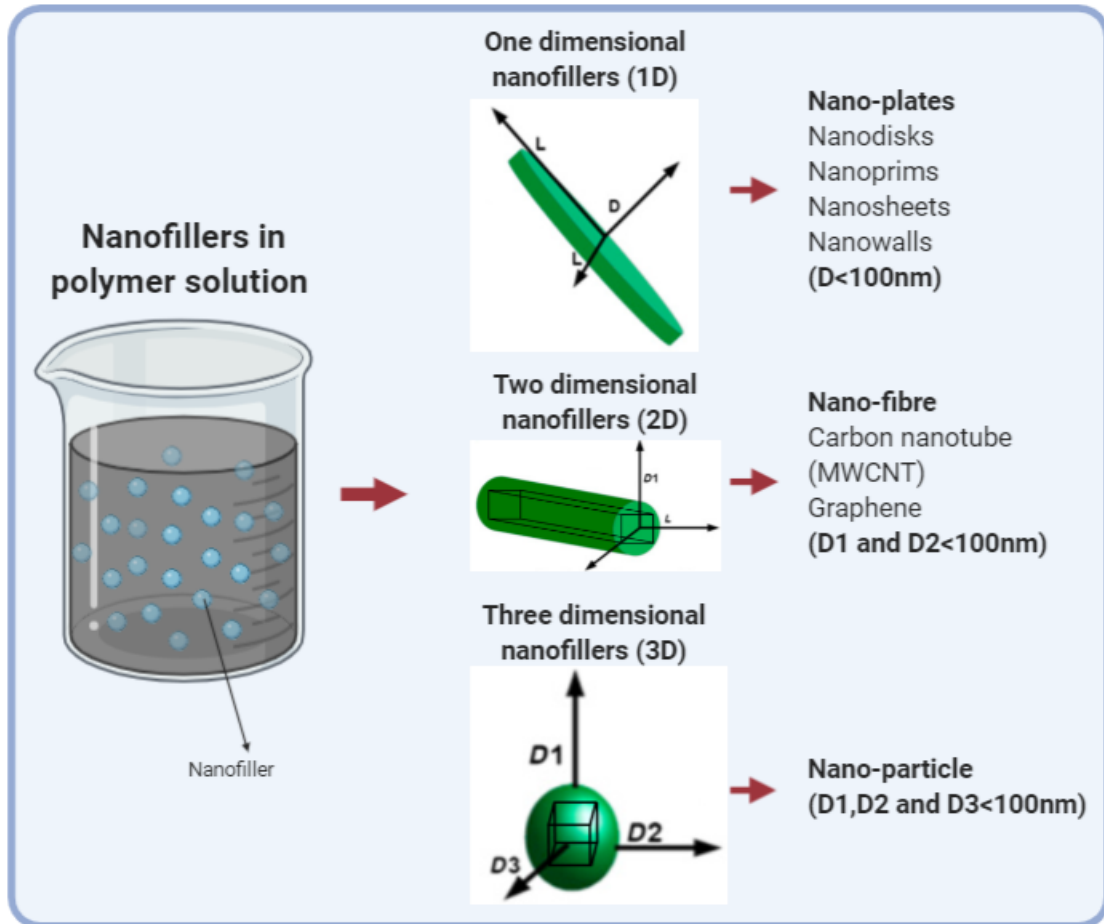


Figure 2.6: Schematic representation of nanofillers types. Modified sketch from Inam et al.⁵

2.1.6 Carbon nanotubes and graphene based ceramic matrix composites

Carbon nanotubes and graphene are widely used in ceramics to improve their mechanical and functional properties. As we can see in the Table. 2.2 CNT and graphene are an ideal candidate for reinforcement of CMCs because of small size, low density, and outstanding mechanical, electrical, and thermal properties³¹. For example, CMCs doped with multiwalled carbon nanotubes (MWCNT) have been reported to improve mechanical properties (fracture and wear resistance), thermal, and electrical properties¹⁹. CNTs are achieving a lot of attention as reinforcement candi-

dates do their thermal stability up to (1800°C)³¹, this factor is crucial for sintering with alumina. CNTs connect the alumina grain boundaries and retard grain growth resulting in the grain refinement during the sintering at elevated temperatures which help in the improvement of fracture toughness, Young's, and shear modulus^{31, 71}. This toughening mechanism is attributed to crack deflection, crack bridging at CNT-alumina interface, and CNT pull-out alumina grains^{31, 72}. Nevertheless, the dispersion of CNT is difficult due to the strong Van der Waals interactions, which form the presence of non-dispersed CNTs, that contribute to the residual pores and defects that reduced the mechanical resistance¹⁹. In general, the weak bonds between carbon allotropes in a ceramic matrix are the main reason for unsuccessful reinforcement⁷³. In this regard, the synthesis strategy to achieve homogeneous and stable dispersion of carbon allotropes is currently a major challenge in material science⁸.

Properties	Units	SWCNTs	MWCNTs	Graphene
Young's Modulus	TPa	~1	~0.3-1	~1
Fracture Strength	GPa	50-500	10-60	130
Thermal Conductivity	$Wm^{-1}K^{-1}$	3000	3000	~5000
Thermal Stability	°C	>700 (in air) 2800 (in vacuum)	>700 (in air) 2800 (in vacuum)	450-650
Specific Surface Area	m^2g^{-1}	400-900	200-400	~2630
Melting Point	K	3550	3550	3800

Table 2.2: Theoretical and experimental properties of CNT and Graphene^{22,23}

On the other hand, the main advantage of using graphene over CNTs is a higher specific surface area. It means graphene has less tendency to tangle, which is easier to disperse into CMCs. According to Shin, graphene is more easily to dispersed in ceramic matrix composites than CNT due to the agglomeration factor²⁸. In terms of production, some researchers have reported easy and inexpensive production of graphene⁸, also graphene has fewer hazards compared to CNTs¹.

As we can observe from Table 2.3, the fracture toughness using carbon allotropes, graphene, and CNT, show similar values of improvement. According to the previous discussion, we can conclude that the remarkable properties of graphene (cost of production, mechanical properties)

Nanofiller type	Nanofiller content	Processing route	Measured density (gcm^{-3})	Investigated properties (% improvement compared to monolith)
Reduced GO ⁷⁴	2 wt-%	Colloidal/SPS	3.81(96%)	Fracture toughness: 5.21 MPam ^{1/2}
Graphene (liquid phase exfoliation) ¹	0.8 vol-%	Powder/SPS	396 (99.9%)	Young's modulus: 373 GPa Hardness: 21.6±0.55 GPa Fracture toughness: 3.9±0.13m ^{1/2}
Reduced GO ⁷⁵	1.69 wt-%	Molecular level mixing/SPS	Flexural strength: 424 MPa Hardness: 22.5 GPa Fracture toughness: 10.5MPam ^{1/2}
Graphene platelet ⁷⁶	0.38 vol-%	Powder/SPS	3.95(99.5%)	Flexural Strength: 523 MPa Fracture toughness: 4.49 MPam ^{1/2}
CNT ³¹	3 wt-%	Powder/SPS	98.60%	Hardness: 23.26 GPa Fracture toughness: 4.93 MPam ^{1/2}
CNT ¹⁹	5 wt-%	Sol-gel/SPS	85.4±2.2%	Young's modulus: 260±97 GPa Hardness: 16±6 GPa Fracture resistance: 5.7±0.5 MGf

Table 2.3: Theoretical and experimental properties of CNT and Graphene based ceramic matrix composites^{22 23}

make this material attractive to reinforced alumina (Al_2O_3) ceramics.

2.2 Graphene

Graphene was discovered in 2004. It is an allotrope of carbon, based on a monolayer of carbon atoms arranged in a two-dimensional honeycomb sp^2 lattice in a plane of 120° angles. The electronic structure of a carbon atom is $(1s)^2(2s)^2(2p)^4$, which means that 2s and 2p are electrons that can be hybridized. The C-C bonds in graphene are 1.42\AA , and the lattice constant is 2.46\AA . As we can observe in Fig. 2.7 carbon atoms (C) are binding with σ and π bonds that contribute to the stability of graphene⁷⁷. Each atom in the graphene network is connected to three carbons

neighbors by σ bonds ($sp^2 - sp^2$ overlap). In this case, the sharing of electrons pairs between carbon atoms involves a covalent bond, which converts graphene into a very strong material (tensile strength is 200 times higher than steel). The $2p_z$ orbital contributes one electron to a conduction band and also contributes to the extended sheet to form graphite through Van der Waals bonds and the interplanar distance is about 0.34 nm ⁷⁸. Due to the periodicity and well-ordered structure, graphene is considered a 2D (two dimensions) material, which means that graphene can grow only in x and y-direction.

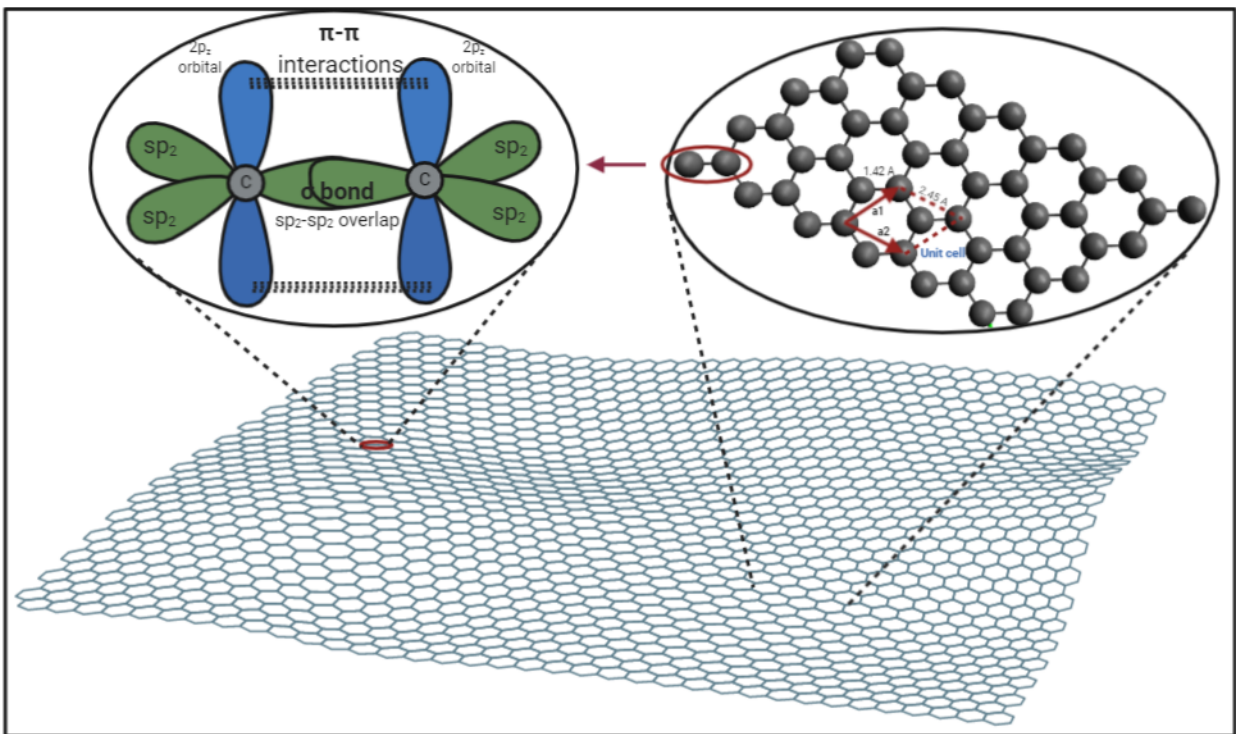


Figure 2.7: Schematic representation of graphene nanomaterial. At the top-left part, carbon with sp^2 hybridized orbitals at the x-y plane. At the top-right part, the graphene network using Avogadro to show the hexagonal arrangement and the unit cell

In recent years, graphene has attributed remarkable industrial applications such as lithium-ion batteries, supercapacitors, nanoelectronics, photovoltaic cells, sensors, hydrogen storage, nanocomposites⁷⁹. The quality and quantity of work on graphene have attracted worldwide

attention⁸. Due to this, material is the strongest and flexible and it's one of the best thermal and electrical conductors, exhibits high charge mobility, and has a high specific surface area⁶. In this work, we report the incorporation of graphene in CMC to enhance the mechanical strength of the composite. There are different types of graphene (i) pristine graphene (ii) graphene oxide (GO) and (iii) reduced graphene oxide (rGO)⁸⁰.

2.2.1 Graphene oxide and reduced graphene oxide

In general, GO and rGO are graphene derivatives. As shown in Fig. 2.8. Chemical and structural properties of GO and rGO are different, which means that, depending on the type of graphene that we want to obtain, it will be the chemical composition treatment. The most remarkable differences are distinguishable in electrical conductivity, hydrophilic behavior, mechanical strength, and homogeneous dispersion of this material. GO can be obtained from graphite oxide by sonication, usually, it was synthesized by oxidation and exfoliation of graphite in presence of water or proper organic solvents⁸⁰. One of the most useful top-down synthesis is the Hummers method.⁸¹. It's commercially available obtained from graphite power¹. Also, it represents eco-friendly synthesis⁸². High-quality graphene can be obtained using bottom-up approach such as chemical vapor deposition (CVD).

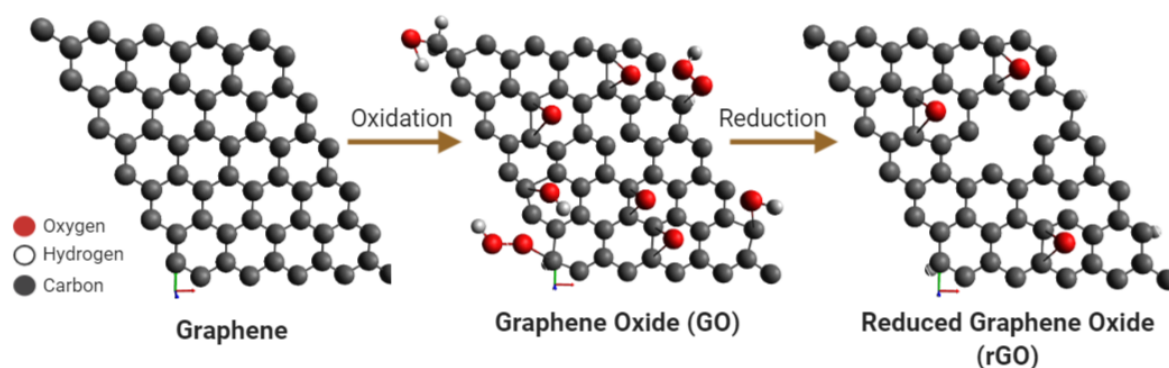


Figure 2.8: Schematic diagram of the lattice structure of Graphene, Graphene Oxide, and reduced Graphene Oxide using Avogadro⁶.

The GO contains functional groups such as hydroxyl, or epoxy groups at the basal plane with a

smaller amount of carboxyl, carbonyl, phenol, lactone, and quinone at the sheet edges⁸⁰ making it easier to disperse in the polymer solution. GO was employed to enhance the electrical, mechanical, and thermal properties of nanocomposites, but GO does not have the same prominent physical and electronic features of pristine graphene. rGO appears as a solution. As we can observe from Fig.2.8 It is synthesized from graphene oxide (GO), the main idea is to reduce the oxygen content present in GO, making the flakes more similar to pristine graphene. The bandgap in GO is ~ 2.2 eV and for rGO, the bandgap can vary from ~ 1.00 to 1.69 eV depending on the degree of reduction⁶. rGO is obtained by chemical or thermal methods to produce a higher degree of reduction, increasing electrical conductivity⁸³. Chemical and thermal reduction of GO is the most attractive methodology due to its simplicity, low cost, and reliability⁸⁴. It's important to mention that the thermal reduction occurs at high temperatures ($300-2000^{\circ}\text{C}$), this damages the flakes, we could have the breaking flakes or the presence of defects within the structure. Nevertheless, chemical reduction presents lower defects due to the degree of reduction is less in comparison to thermal reduction⁸⁰.

2.2.2 Electronic band structure of graphene

In order to obtain information about the electronic band structure of graphene quantum mechanics theory. Graphene is the most typical 2D material with Dirac cones⁷⁷. Dirac cones are proposed by Paul Dirac. It provides information on the electron transport properties of the material. According to Fig. 2.9 (a), graphene possesses an unusual electronic band structure, the valence, and conduction band of graphene near to the Fermi level arises a shape of the upper and lower halves of a conical surface in momentum space, touching at Dirac point. When two bands touch at the Dirac points a Dirac cone is formed. Graphene is considered as a zero bandgap material, due to graphene possessing no bandgap (valence and conduction band are touching). Pz orbital overlaps the neighboring C-atom Pz orbital to form a filled π -orbital (valence band) and empty π^* -orbital (conduction band)⁸⁵. On the other hand, in graphene oxide energy band Fig. 2.9 (b), we can notice the formation of a gap between the valence and conduction band. In oxidized graphenes, the π and π^* orbital of graphene is disrupted which contributes to the formation of a bandgap. A carbon atom is substituted by an oxygen-containing functional group. This semimetal feature is appropriated for the materials that require a specific bandgap which provides unique electronic characteristics. Reduce graphene oxide exhibits an electrical conductivity that can be

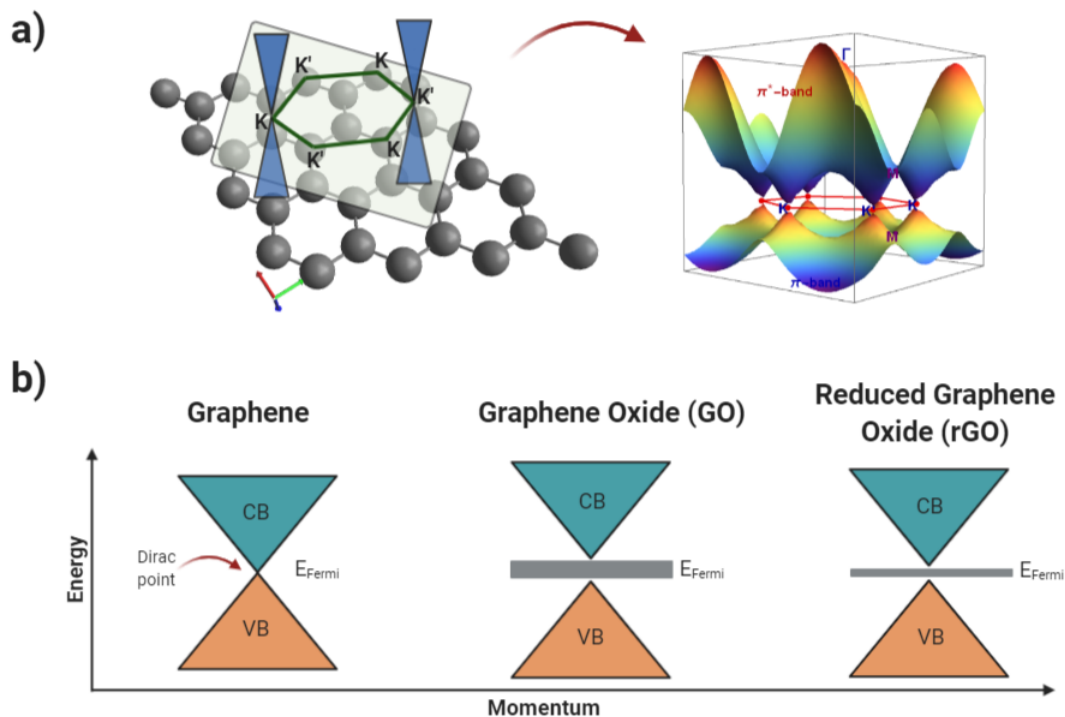


Figure 2.9: (a) Schematic diagram of lattice structure and valence/conductive Dirac cones at the K points of the hexagonal lattice in reciprocal space at the Fermi level using Avogadro and Mathematica program. (b) Energy band diagrams of Graphene, GO, and rGO using Avogadro. VB (valence band), CB (conduction band)^{6, 7}

tuned by controlling its oxygen content⁶.

2.2.3 Graphene based materials functionalization

The surface properties of graphene can be modified via structural alteration including chemical doping, chemical functionalization, and controlled reduction⁸⁵. Depending on the synthesis methodology, we can reach semiconducting materials with different electronic characteristics. According to Fig 2.10 there are some factors that affect the development of graphene ceramic matrix composites during processing. For example, (i) Dispersion technique of graphene (ii)

Dispersion techniques of GCMC (iii) Alignment of the graphene sheet into CMC (Sintering). Depending on the manufacturing process of GCMC, we can achieve well-dispersed and homogeneously graphene inside the matrix composite, increasing the electrical, mechanical, and thermal properties of nanocomposites.

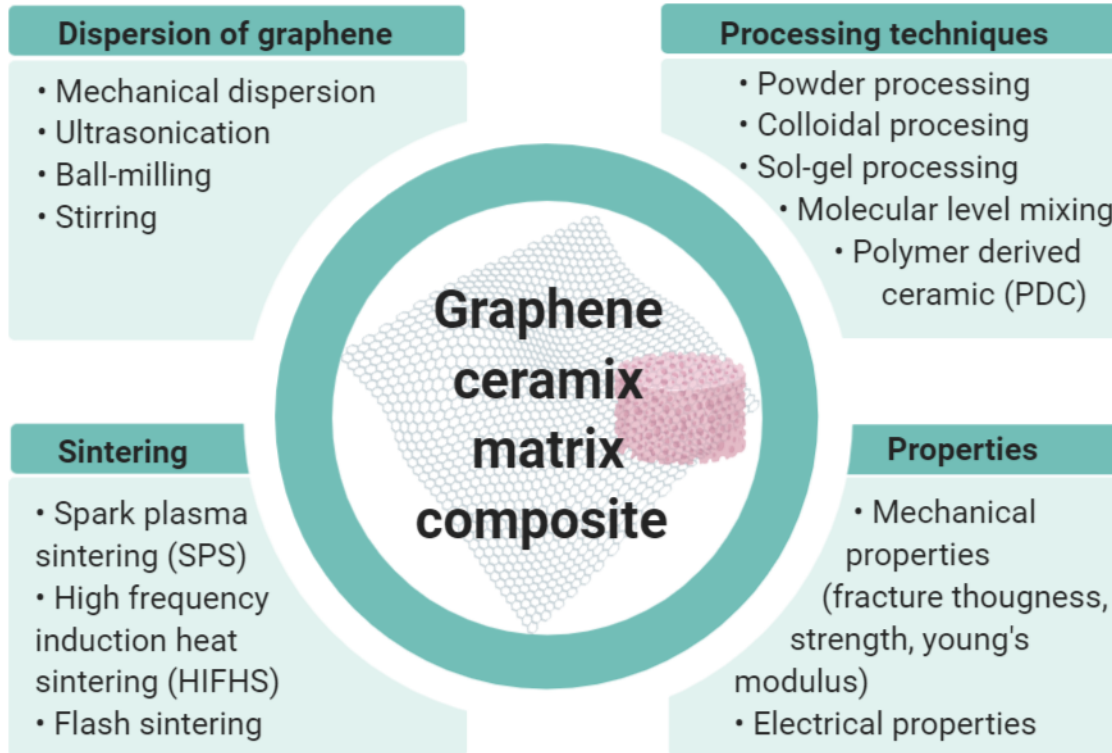


Figure 2.10: Recent progress of Graphene based ceramic matrix composite (GCMC). Modified sketch from Markandan et al.⁸

For the purpose of this investigation, we consider (i) ultra-sonication to mixed of precursors, (2) sol-gel processing to obtain good dispersion and to promote the intragranular location of graphene²⁷ and (iii) reactive Spark plasma sintering (SPS) for consolidated this nanopowders into nanostructured bulk materials⁸⁶. Discussed in the next section.

2.3 Characterization and sample preparation techniques

2.3.1 Sol-gel processing

Sol-gel processing is a technique that provides a remarkable route to create a homogeneous dispersion of graphene in ceramic composites⁸. This method has been reported and is easy to control throughout the synthesis process⁹. Sol is a stable suspension of colloidal solid particles in the liquid phase. In general, the sol-gel process involves the transition between liquid “sol” to solid “gel” phase⁸⁷. There are three main advantage of the sol-gel process: (i) It uses relatively low temperatures, (ii) It can create very fine powders, and (iii) It produces compositions not possible by solid-state fusion⁸⁸. As we can observe in Fig. 2.11 First step is mixing the precursor. Second, we add the solvent, which means that a colloidal suspension is formed. Sol becomes stable due to the forces between the particles are repulsive and prevent the agglomeration and hence coagulation⁸⁷, as a result, we obtain a good dispersion of solid particles into precursor material. Third, the wet gel is formed (gelation process). Sol passed to gel transition under the addition of a base or acid catalyst. Crosslink and branching particles occur (forming a 3D interconnected porous network)⁹. The solid particles present in the network can be crystalline, amorphous, or macromolecules.

The final stage, it's related to the processing of the gels. Xerogel is formed with thermal drying treatment (evaporation of a solvent), under a sintering process the gel is converted into a dense ceramic. Aerogel is formed when the liquid phase is removed from wet gel under supercritical drying (extraction of a solvent). Aerogels are the lowest density materials⁸⁹. Cryogel is formed under freeze-drying conditions (sublimation). For the purpose of the investigation, we follow the route of xerogel.

The starting materials of sol-gel are oxides (silica), metal oxides, organic materials (metal alkoxide/inorganic metal salts), polymers (cellulose), and carbon materials (graphene, CNT)⁹. The main focus of this investigation will be graphene dispersion into the boehmite/ $\alpha\text{Al}_2\text{O}_3$ seeds ceramic matrix through the sol-gel technique followed by the use of reactive Spark Plasma Sintering methodology.

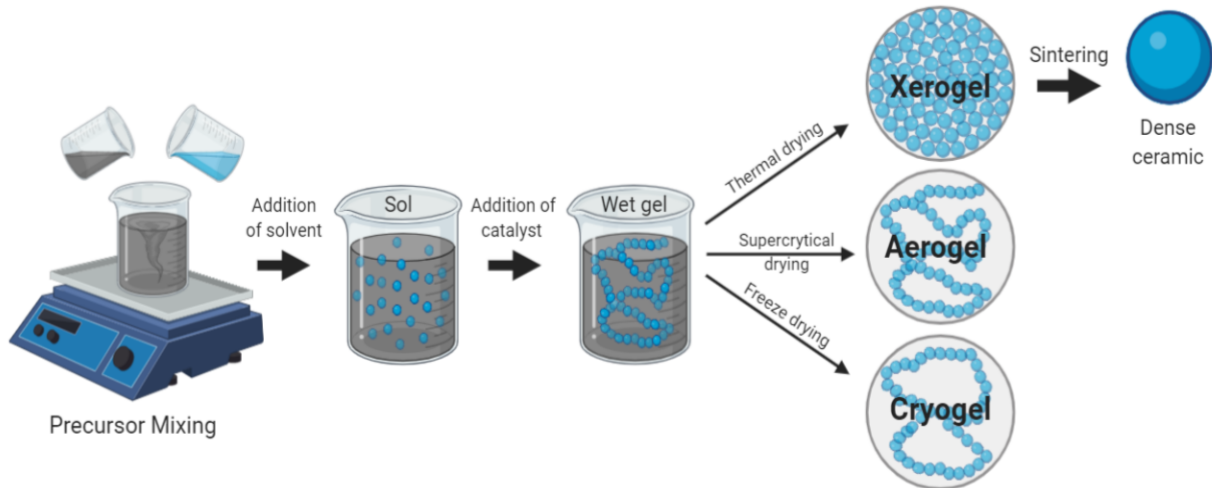


Figure 2.11: Schematic representation of sol-gel processing. Modified sketch from Dervin et al.⁹

2.3.2 Spark plasma sintering (SPS)

Sintering techniques require long processing times and high temperatures to prepare densified ceramics. These factors contribute to the grain growth and simultaneous degradation of the nanofillers²⁴. As if today, the degradation of two-dimensional carbon nanofillers (CNT, graphene) using conventional sintering has been reported in the literature due to the relatively long time sintering (hours)^{90,73}. In order to avoid these issues, there are novel sintering techniques that reduce the sintering temperature and the processing time. Spark plasma sintering (SPS) is a conventional processing method used for graphene ceramic composites. SPS is one of the most significant and effective sintering techniques, it allows the compaction or densification of ceramics at temperatures lower than their melting point with short holding time⁹¹. As a reference, It will use quickly sintering time in a matter of minutes (3-10 min) instead of hours²⁴. However, the rapid densification, grain-growth rate, and mechanical properties (hardness and fracture toughness) are been influenced by some parameter like (i) mechanical pressure (ii) heating rate (iii) applied current (iv) pulse sequence, and (v) holding time⁹¹. The SPS mechanism involves pressure and electric field simultaneously through a graphite die containing ceramic powders to be sintered. The pulse generates sparks discharge and also plasma between the powder composites⁸.

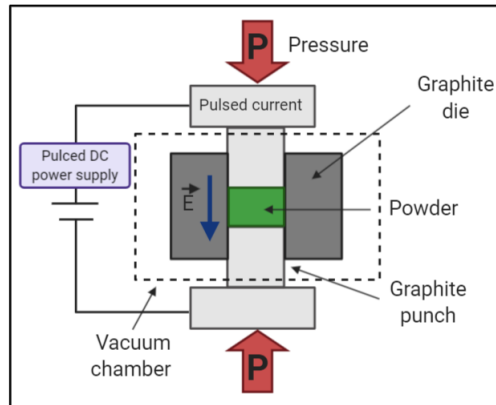


Figure 2.12: Diagram of spark plasma sintering

As we can see in Fig. 2.12 the precursors are loaded in a die and graphite punches containment under a uniaxial pressure ($>100\text{MPa}$). Graphite punches provide a direct pulse current (up to 10V and 10kA) through the powders⁹². Die as well conductive powder acts as a heating source, a pulse direct current passed through it⁹¹. For example, GCMC sintering the sample is heated from the inside and the outside due to graphene being conductive. The pulsed direct current produces an electric field during the sintering process⁹³. The mechanism involved during the densification and grain growth has not yet been well explained. But generally, the application of uniaxial pressure enhanced the diffusion through the removing pores of the sample. One of the advantages of SPS is that GCMC can rapidly achieve isothermal conditions, enabling densification to be studied over a wide range of densities¹. Also, this technique can lead us to process the high-temperature material with poor deformability into configurations that in the past were impossible⁹³. In order to produced a dense nanomaterial by SPS technique. It can follow two possibilities: (i) simultaneous reaction and densification (ii) complete reaction followed by densification⁸⁶. The first one is the best situation, dense nanostructured product require a chemical reaction within a narrow temperature range accompanied by shrinkage of the sample⁸⁶. If we combine the advantages of carbothermal reduction (GO) and SPS technique, we are employing a reactive spark sintering (rSPS)⁹⁴.

In this work, we are using Reactive SPS to enhance densification and grain growth of graphene ceramic matrix composites (GCMC). Reducing the sintering temperatures, within a shorter time.

2.3.3 X-ray diffraction (XRD)

X-ray diffraction (XRD) is a non-destructive and powerful technique for the characterization of structure matter (crystalline or amorphous), phases, orientation, grain size, and strain⁹⁵. This technique was introduced by von Laue's discovery in 1912. He was recorded successfully the diffraction pattern of copper sulfate crystal⁹⁶. Later on, Henry Brag was able to explained mathematically, the interaction between the crystal and the incident wavelength. As shown in Fig. 2.13 X-ray are produced from x-ray tube enclosed in a vacuum chamber. The electrons are produced by heating the tungsten filament of the cathode through a high potential field. After that, the electron hit the anode and the loss energy of electrons is manifested as x-rays⁹⁷. Normally, XRD depiction is done by x-ray source of Cu $k\alpha$ radiation ($\lambda=1.54\text{\AA}$)⁹⁸. XPS employed a high voltages (20-50 kV), and also, the general shape was chosen depend on the analytical requirements. Divergence and soller slits reduce the angular beam divergence in parallel and perpendicular directions to the diffraction plane, respectively¹⁰. The accuracy of this technique depend on the homogeneity of the solution, properly folded and stability.

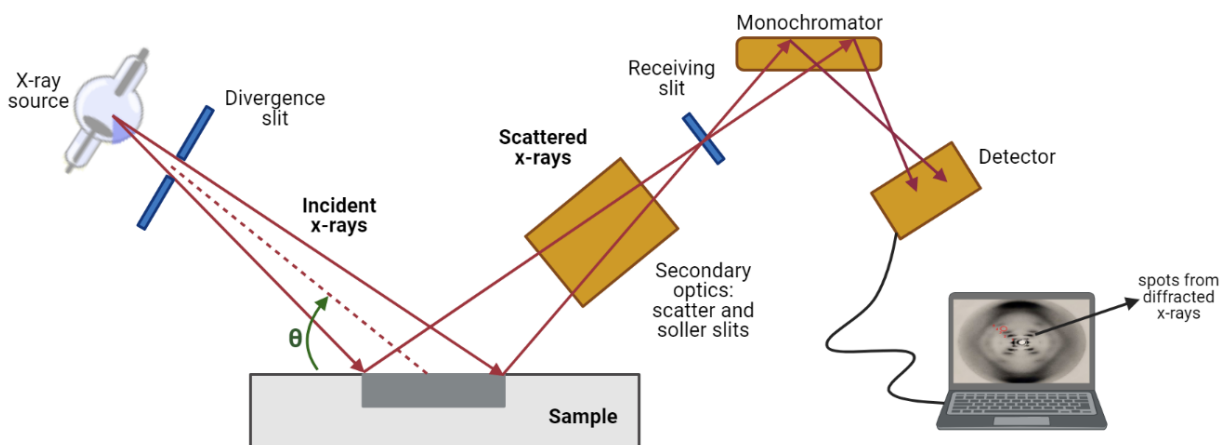


Figure 2.13: Schematic diagram of X-ray diffraction (XRD) Modified from Epp et al.¹⁰. X-ray diffraction image of crystallized DNA¹¹

At the moment that x-rays photons hits the matter, an elastic occurs (Rayleigh scattering) between the photons and the electrons surrounding the atomic nuclei¹⁰. However, as shown in Fig.2.14 depending on periodic nature of the crystal structure, we could have constructive or

destructive scattering. Bragg gives a geometrical interpretation of the XRD technique using the constructive interference⁹⁹.

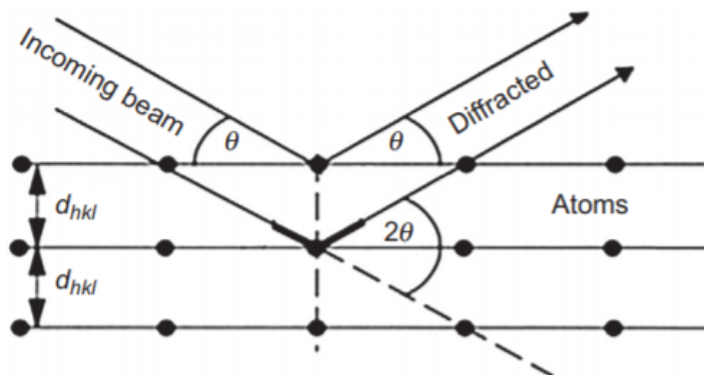


Figure 2.14: The principle of Bragg's law from lattice planes¹⁰.

These reflection only take place under specific geometrical conditions satisfying the Bragg's law given in the following equation:

$$n\lambda = 2d_{hkl}\sin(\theta) \quad (2.1)$$

Where n is an integer number of diffraction order, λ is the wavelength, d is the distance between the lattice, and θ is the diffracted beam angle (degree)¹⁰. This equation is used to explain the interference pattern of x-rays scattered by the crystals.

2.3.4 Thermogravimetry analysis (TGA)

Thermogravimetric analysis (TGA) is a thermal analysis technique. This instrument measures the amount and rate of change in the weight of a material as a function of temperature or time in a controlled atmosphere¹⁰⁰. These techniques were first introduced back in 1887 by Henry Le Chatelier¹⁰¹. Nowadays, we can use this technique to characterize materials, food, pharmaceutical and petrochemical applications¹⁰⁰. The commercial TGA temperature was in the range of 1000°C or more¹⁰². The inert, oxidizing and reducing atmosphere are created by the gas flowing through the balance¹⁰². TGA thermal curve is plotted time or temperature vs

weight (mg) or weight percentage (%). It is displayed from left to right. The descending behavior indicates a weight loss occurred¹⁰⁰.

2.3.5 N_2 Physisorption

N_2 physisorption analyses were undertaken by Brunauer and Emmet. This technique allows us to determine the surface area and the pore distribution of various porous materials¹⁰³. As shown in Fig. 2.15, when the nitrogen gas is in contact with a clean solid surface at 77 K, a specific number of gas molecules will be attracted to the surface of the solid by van der Waals forces¹⁰⁴. This process is called adsorption or physisorption. Which is thermodynamically reversible at isothermal conditions.

BET theory by Brunauer, Emmett and Teller¹⁰³ contribute with a mathematical model that explains the gas sorption process. In order to estimate the specific surface area of a material, we need to take account the amount of nitrogen (N_2) gas absorbed in equilibrium with relative pressure (P/P_o). (P/P_o) is the ratio between absolute gas and saturation pressure. In this method, we assumed that the surface is homogeneous. At low pressures ($p/p_o < 0.2$), micropores are filled with N_2 ; as pressure increases mesopores fill; and from $p/p_o = 0.96$, macropores are filled. Theoretically, at $p/p_o = 1$ all pores are filled¹⁰⁴.

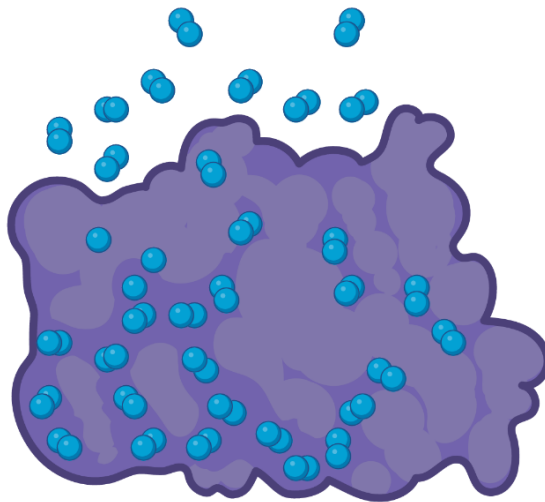


Figure 2.15: Schematic representation of idealized physisorption model

2.3.6 Density

Archimedes' principle states that a body immersed in a fluid is subjected to an upwards force (buoyant force) equal to the weight of the displaced fluid (gravity force)^{105, 106}. This mechanism explained the equilibrium of a body floating in water. In this case, Archimedes method was used to measure the theoretical density and relative density. As shown in Fig. 2.16, a single sample is weighed in two different fluids: (i) air (as a fluid reference) (ii) water, acetone or ethanol¹². If we used water as a second fluid, it's important to prevent the formation of air bubbles, due to the surface tension of water is too high that inhibits the full penetration of water inside the lattice structures¹².

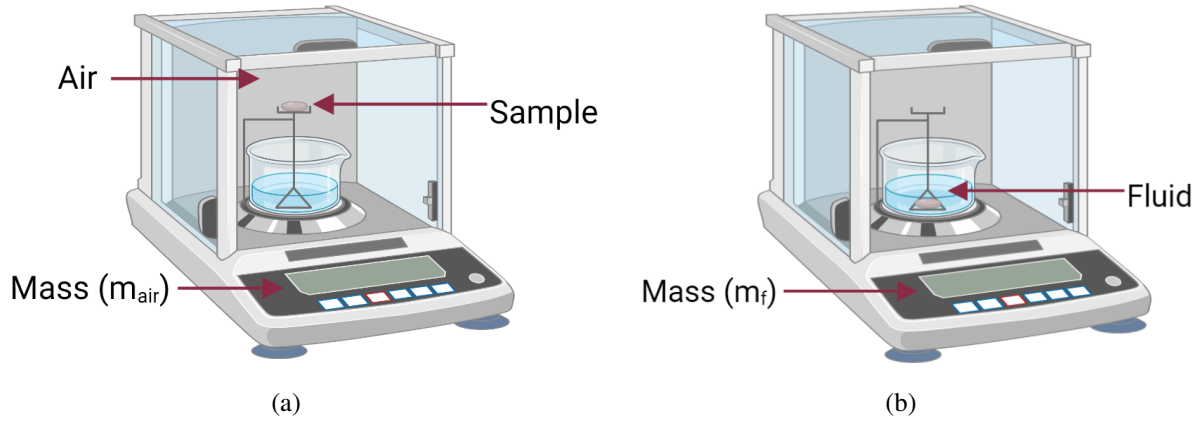


Figure 2.16: Schematic representation of Archimedes method density measurements (a) sample weighed in the air (reference) (b) sample weighed in fluid. Modified from Arvieu et al.¹²

Theoretical density of biphasic composite (Alumina/GO) is calculated weighting the two densities as shown in following equation:

$$\rho_{theoretical} = \frac{\rho_1 \rho_2}{\rho_1 \frac{\chi}{100} + \rho_2 (1 - \frac{\chi}{100})} \quad (2.2)$$

Where ρ_1 (3.985 g/cm³) and ρ_2 (2.1 g/cm³) are the theoretical densities of graphene¹⁰⁷ and alumina respectively, and χ is the wt.% of secondary phase in the composite¹⁹. Moreover, knowing the density of the fluid, that in this case is water (0.9973g/cm³), we can calculate the relative densities of the sample according to the eq.2.3

$$\rho_{measured} = \frac{M_{air}}{M_{air} - M_{fluid}} \times (\rho_{fluid} - \rho_{air}) + \rho_{air} \quad (2.3)$$

Where, ρ_{sample} is the sample density (g/cm^3). M_{air} is the mass of the sample in air (g) as show in Fig.2.16 (a). M_{fluid} is the mass of the sample in fluid (g) as show in Fig. 2.16 (b). ρ_{air} is the air density (g/cm^3), and ρ_{fluid} is the fluid density (g/cm^3)¹⁰⁸

If we compared the Theoretical density and relative density results, we can calculate the rate of porosity in the sample:

$$\%porosity = 100 - \left(\frac{\rho_{measured} * 100}{\rho_{theoretical}} \right) \quad (2.4)$$

2.3.7 Scanning Electron Microscopy (SEM)

Scanning Electron Microscopy (SEM) is a technique that provides surface images of solid objects using a beam of focused electrons instead of light. These important microscope allows us to characterize the materials from nanometer to micrometer scale¹⁰⁹. SEM provides prominent information about micro-structure morphology (crystalline and orientation structure), and chemical composition¹¹⁰. After the discovery that these electrons can be deflected under the magnetic field in 1980. The scientist start to use electron microscopy by replacing the light source with high energy electron beam¹¹¹. In order to understand the Scanning electron microscopy we need to examine the electron beam interaction with the sample, resolution limitation and signal generation.

As show in Fig. 2.17, the equipment has an electron gun source (filament) that generated an electron beam with a specific intensity. Normally is a Tungsten filament lamps, which is heated to over 2500°C to produce thermal emission of electrons from its tip. Inside the chamber it required a ultra-high vacuum conditions (10^{-10} to 10^{-11} Torr) in order to prevent the oxidation environment form contaminant particles¹¹². The anode and cathode increase the velocity of the electrons from the electron beam using high voltage system (1 to 30kV), knowing as accelerating voltage. Condenser lenses and objectives lenses enhance the focal point and controlled the intensity of beam current. Finally a narrow electron beam hits the sample. Producing a large number of signals such us backscattered electrons, secondary electrons and x-ray radiation¹¹³. Which are collected by a specific detector.

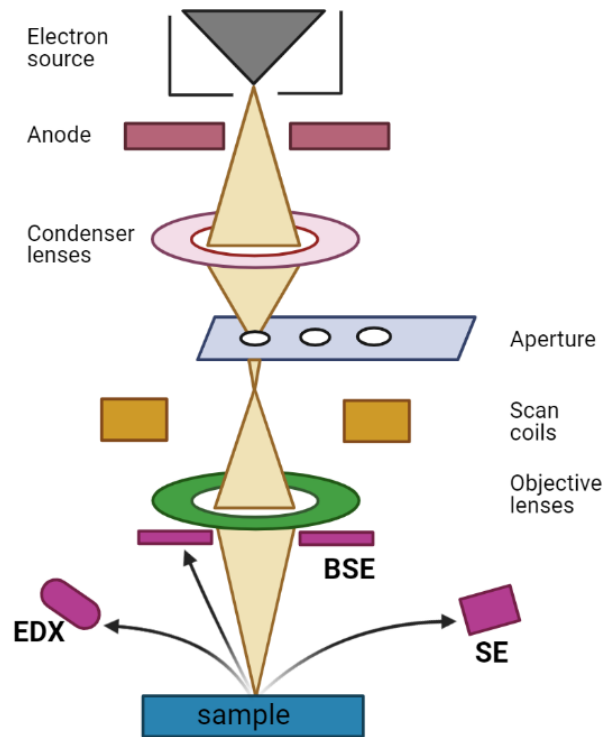


Figure 2.17: Schematic diagram of scanning electron microscopy (SEM). Signals generated by electron beam-specimen interaction: EDX nergy-dispersive X-ray spectroscopy, BSE backscattered electrons, and SE secondary electrons Modified from Shah et al.¹³

- Secondary Electrons (SE), are electrons resulting from inelastic interactions between the electron beam and the sample. Inelastic scattering is characterized by energy loss during the collision¹¹¹. Which exhibit low energies (less than 50 eV). Typacally, the resolution of SE is $\sim 100\text{\AA}$ ¹¹⁴. It provides superficial information of the sample.
- Back-scattered Electrons (BSE), are high-energy electrons reflected back after elastic interactions between the beam and the sample. Elastic scattering is characterized by negligible energy loss during the collision¹¹¹. It has a resolution of $\sim 500\text{\AA}$ ¹¹⁴. It provides information of chemical composition and topographic information.
- Energy dispersive X-ray analysis (EDS) show a semi-quantitative chemical composition.

The resolution in SEM can be describe mathematically by Abbe's equation, as shown below:

$$d = \frac{0.612\lambda}{n\sin(\alpha)} \quad (2.5)$$

Where, d is resolution, λ wavelength of radiatio, n is the index refraction of medium between point source and lens, and $n\sin(\alpha)$ is the numerical aperture¹¹¹.

The preparation of samples in SEM require very short time in comparison to other techniques such us TEM. TEM specimen preparation is more complex and time consuming¹¹⁵.

2.3.8 Raman

Raman scattering was discovered in 1928 by Krishna and Raman. As if today, this technique has been used in many research papers applying for quantitative and qualitative chemical analysis. Raman is a spectroscopy technique that provides a non-destructive, non-contact chemical analysis through the vibrational modes of molecules. This vibration is created by the interaction of light with chemical bonds. Typically, in Raman, we employ a monochromatic light (laser in visible, near-infrared, or near ultraviolet range), which stimulates the molecules to reach the high-energy states of excitation "virtual states". As we can observe in Fig 2.18 (a) when monochromatic light ($h\nu_o$) interacts with a matter (gas, solid, or liquid) molecular vibration begins in different energy levels¹⁵. As a result, the energy of the laser photons ($h\nu_{vib}$) will shift to lower or higher frequency. If the scattered wavelength ($\lambda_{scatter}$) of the molecule is at the same wavelength that the laser source (λ_{laser}) is Rayleigh scatter. It does not provide useful information. In contrast, if the scattered wavelength is different than the wavelength of the laser is called Raman scatter¹¹⁶. Depending on the chemical structure of the analyte we could have Stokes Raman scattering or Anti-Stokes Raman scattering. Virtual states are considered a very short-lived distortion of the electron cloud caused by the oscillating electric field of the light¹⁵.

In Fig. 2.18 (b) we observe that raman spectroscopy is the inelastic scattering of a photon. It depends on the vibrational energy transition. For example, If the photon reaches a higher vibrational energy state (loss energy) in comparison to the original state or to a lower vibrational energy state (gain energy), it is stokes or anti-stokes Raman scattering respectively. Stokes and anti-stokes are symmetrically positioned about the Rayleigh peak but the main difference comes from their intensities at low vibrational energies¹⁵ as shown in Fig. 2.19.

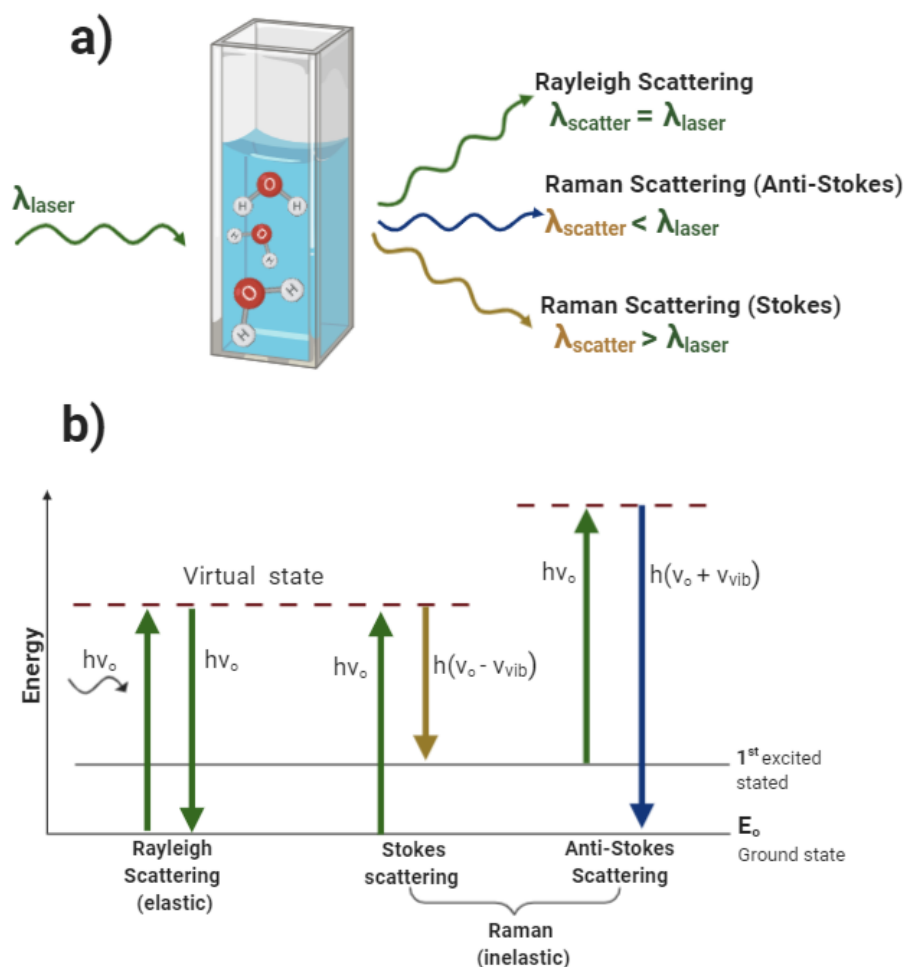


Figure 2.18: Basic principle of Raman spectroscopy (a) Schematic representation of Raman principle (b) Quantum Energy transitions diagram for Rayleigh and Raman scattering¹⁴.

The intensity of Raman spectrum is proportional to the concentration and each peak corresponds to a specific Raman shift, which provides a particular vibrational frequency used as a chemical fingerprint that describes a distinct molecule or material. Raman shift is defined as the frequency difference ($\Delta\nu$) between the excitation radiation and the Raman scattered. Raman shifts are typically in wavenumbers (cm^{-1}). It is defined as:

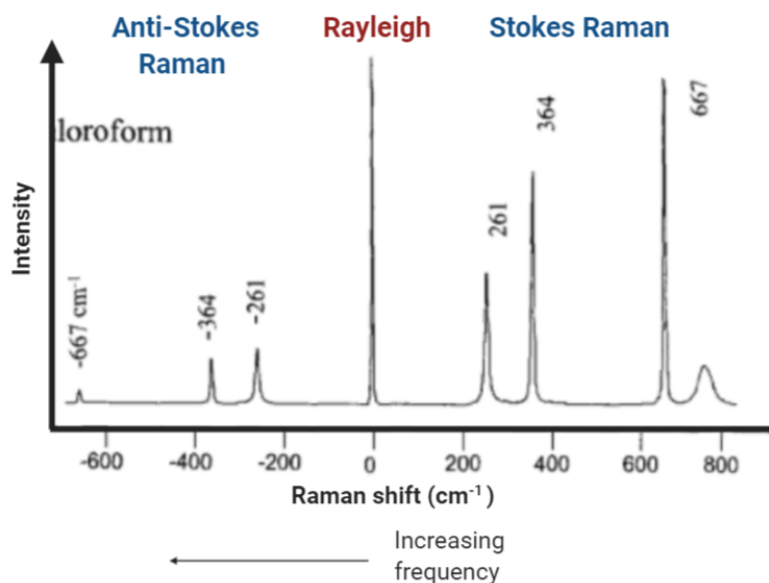


Figure 2.19: Stokes and Anti-stokes Raman spectral lines of chloroform obtained with 514.5 nm excitation¹⁵.

$$Raman\ Shift[cm^{-1}] = \frac{10^7}{\lambda_o[nm]} - \frac{10^7}{\lambda_{vib}[nm]} \quad (2.6)$$

where λ_o is the laser wavelength and λ_{vib} is the raman peak wavelength. In order to convert wavenumbers to wavelength, we get the following equation:

$$\lambda_o[nm] = \frac{1}{\frac{1}{\lambda_{vib}[nm]} - \frac{Raman\ Shift[cm^{-1}]}{10^7}} \quad (2.7)$$

Using wavelength values, we can plot an absolute wavelength scale. In contrast, using wavenumber, we plot a relative wavenumber scale. As shown in Fig. 2.20 The mechanism of Raman spectroscopy is governed by (i) laser source (ii) optical path and (iii) detector. The sample is illuminated with a single frequency light source. For example, UV lasers (244nm - 325nm) are used for biological, catalysts samples. Visible laser (488nm - 541nm, 633nm) is employed for semiconductors, catalysts. biological, mineral, and polymers samples. NIR laser (785nm, 830nm) is used for polymers and biological samples¹¹⁷. The light is collected with

optical components and finally, it is reached by the detector. In this case, we employ bandpass and rayleigh filters to prevent the pass of undesired wavelengths that do not provide useful information for the chemical analysis¹⁶. Bandpass filter is used to control the frequency stay within a certain range and rejects the other. The beam splitter, as the name said, it split a beam of light in two. One path goes to the sample and the other path is the light that comes from the optical microscope to the CCD detector. A diffraction grating is like a super prism, it separates the light in different wavelengths, and it has a high resolution.

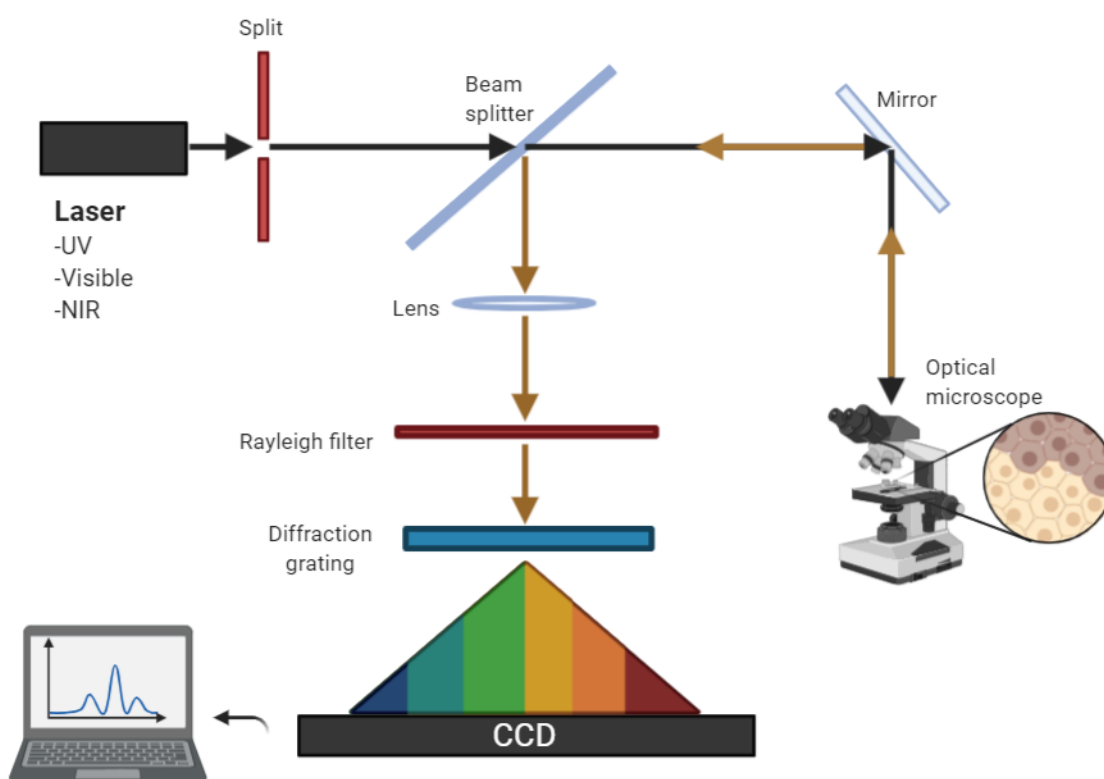


Figure 2.20: Schematic diagram of Raman spectroscopy. Modified sketch from¹⁶

Raman spectroscopy of graphene

According to Malard¹¹⁸, there are some researches that have developed experimental and theoretical studies to explain the characterization of graphitic materials. Raman spectroscopy technique

is one of the most powerful tools for graphene characterization. This allows us to understand the behavior of electrons and phonons in graphene¹¹⁸. In these words, we identify vibrational modes and phonons in the sample to determine features like disorder, edge, thickness, doping, grain boundaries, strain, and thermal conductivity of graphene¹¹⁹. The characteristic peaks of graphene in the Raman spectrum are four: D (1350 cm^{-1}), D' (1620 cm^{-1}), G (1580 cm^{-1}), 2D (2690 cm^{-1}), resulting from the shift of Stokes phonon energy caused by laser interaction with the sample¹¹⁹. 2D peak is also called as G' peak in order to avoid the confusion of the notation of two dimensional (2D). In this work we referred to 2D peak. The spectrum will change depending on the number of graphene layers, G peaks shifts linearly as a function of the number of layers¹¹⁶. Using the ratio peak intensity I_{D}/I_G we are able to detect the level of disorder in other words the quality of graphene. If the disorder increases it creates more elastic scattering¹¹⁸. On the other hand, I_{2D}/I_G ratio is an indicator of the crystallinity of graphene. The defects reduced the G' peak²⁷. For Raman spectra of graphene is essential to understand the phonon dispersion of graphene. Unit cell of graphene contains two carbon atoms (A and B), there are six phonon dispersion bands. Three are acoustic branches (A) and the other three are optic (O). The phonon modes are two: longitudinal (L) and transversal (T). Depending on the phonon vibration we can have six dispersion curves LO, iTO, oTO, LA, iTA and oTA phonon modes.

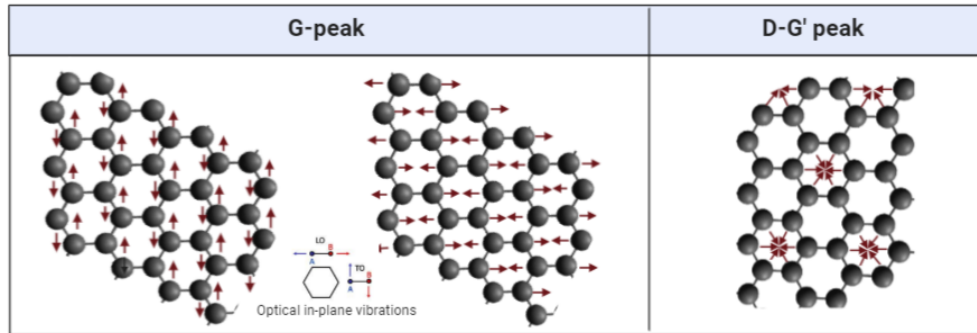


Figure 2.21: Raman vibrational modes of graphene for G, D, and G' peak¹⁷

As we can see in Fig. 2.21 the main vibrational modes of graphene for G peak is associated with iTO and LO phonon mode at the Brillouin zone center. For two acoustic and two optic phonon branches, the vibrations are in-plane¹¹⁸. The vibrational mode of D and G' peak result from the carbon hexagons breathing in graphene lattice. If we analyse those vibration modes

employing first order Raman and double resonance Raman scattering concepts shown in the Fig. 2.22 we notice that, G band, comes from a normal first-order Raman scattering and D and 2D band emerge from second-order process. For D band it involves one iTO phonon and one defect. There is one elastic scattering caused by a defect and one inelastic scattering by a phonon. The G' involves two iTO phonons near the K point without any kind of disorder or defect. Both processes are inelastic scattering, which scatters from k and k' point (intervalley)¹¹⁹. The notation of D' is for weak disorder, in this case the mechanism involved is called intra-valley due to it connecting two points in the same circle around k or k' point¹¹⁸.

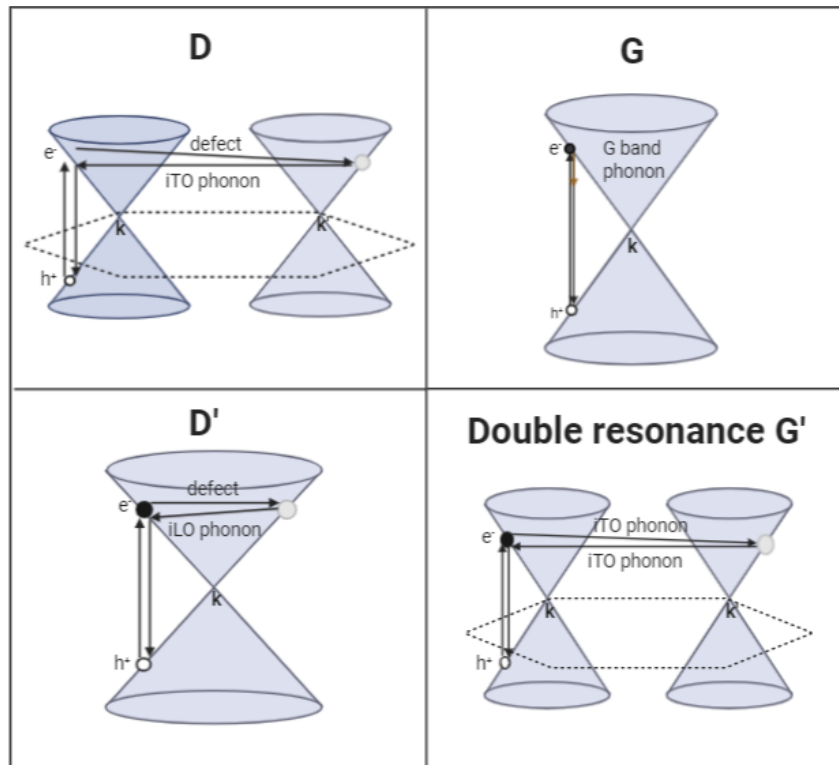


Figure 2.22: Schematic diagram of first order Raman scattering process (G band) and double resonance Raman scattering (D, D', G') in graphene

2.3.9 X-ray Photoelectron spectroscopy (XPS)

XPS is a non destructive, surface-sensitive and powerful technique that provide information about the chemical composition of the sample.

Photoelectron spectroscopy was experimental observed by Heinrich Hertz in 1887¹²⁰ and later was explained by Albert Einstein in 1905 as a photoelectric effect, earning the Nobel Prize in Physics¹²¹. The mechanism involve in XPS is carried out by exciting a sample surface under ultra high vacuum (10^{-9} Torr) with a single-energy X-ray photon. Normally, XPS has an average depth of 5 nm. When the electrons absorb enough energy it star to ejected from the sample with a maximum Kinetic energy (photoelectric effect). By definition the maximum kinetic energy is given by:

$$E_k = h\nu - E_B - \Phi \quad (2.8)$$

Where $h\nu$ is the energy of the photon, E_B is the electron binding energy and Φ is the work function. Basically, as shown in Fig. 2.23 E_B gives an idea about the minimum energy that required an electron to remove from the surface of a metal. Work functions is defined as the potential barrier, which prevent the escape of valence electrons.

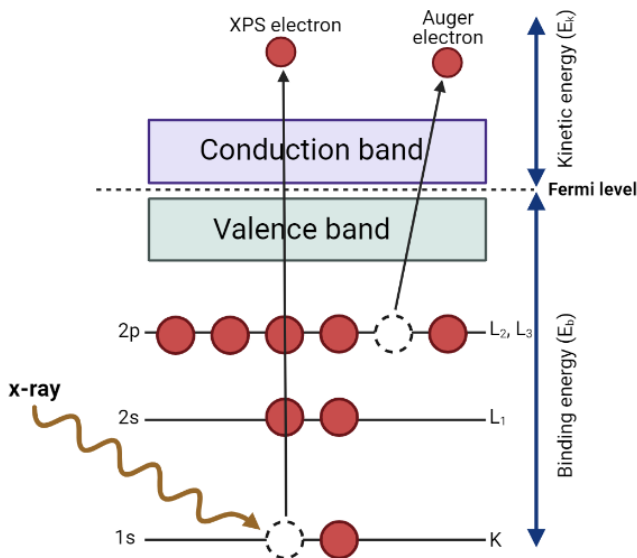


Figure 2.23: Schematic view of photoelectron emitted by incident x-ray photon.

In this process, the free electrons generated has a certain Kinetic energy E_k that are specific for each type of atom. These unique feature of XPS allow us to use for determine the chemical state information of the elements in the surface¹²².

Experimental set-up of XPS

In Fig. 2.24 A typical XPS works under ultrahigh vacuum to avoid the scattering electron in gases. Inside the chamber, It has an electron gun, anode, monochromator, sample holder, hemispherical kinetic energy analyzer, and electron detector. First, the electron source hit the anode which produce come X-ray photons. Aluminum and magnesium material are most used, providing Al $K\alpha$ and Mg $K\alpha$ x-rays¹²³. Second, X-ray is selected inside the monochromator to enhance a stable signal. Third, the x-ray beam hit the sample and excite the electron form the material surface. When the electrons are emitted by the photons. It was considered as photoelectrons. Fourth, those photoelectrons are collected by hemispherical electron analyzer that measure their kinetic energy. And finally, the electrons reach a detector that generates a signal. XPS spectrum provides the information about the energy distribution in a material. Intensity (number of photo-ejected electrons versus time) versus Binding energy¹²⁴.

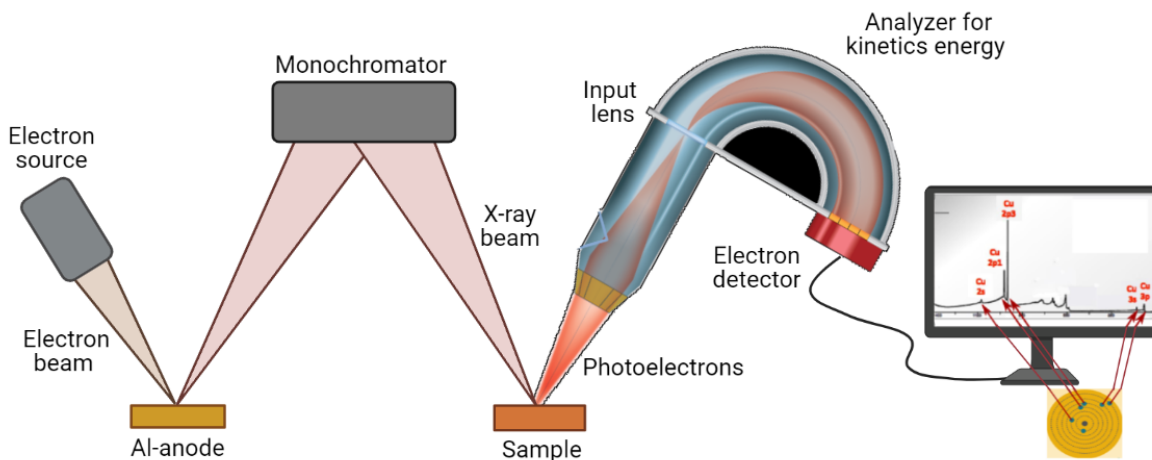


Figure 2.24: Schematic diagram of X-ray photoelectron spectroscopy process.

2.3.10 Mechanical characterization

At today, the two most popular techniques for the measurement of the fracture toughness for brittle ceramics, namely Single-Edge Notched Beam (SENB) and Vickers Indentation Fracture (VIF)^{19,125}. Indentation test is an easy, inexpensive and non-destructive method to evaluate the basic properties for small volumes of materials¹²⁶. In this case, we have used VIF test to estimated the fracture toughness, through initiation and propagation of cracks¹²⁵ created by hardness indentation. As shown in Fig. 2.25 the hardness indentation test consists of loading with diamond indenter or any other hard material with square base (136° between the opposite faces). Which pressing it into the surface of a softer material to be examined normally applied for 10 to 15 seconds. Sharp indenters are usually in the shape of pyramids with 4 different types bases (i) square base (Vickers), (ii) triangular base (Berkovich), (iii) rhomboid base (Knoop), (iv) or in conical shape (Rockwell)¹²⁶.

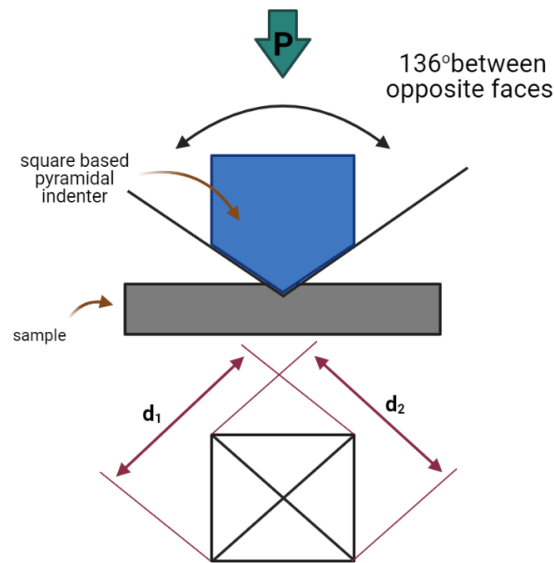


Figure 2.25: Schematic representation of Vicker Indentation test and illustration of the two indentation diagonals d_1 and d_2 . Modified from Alhashmy, Hasan¹⁸

VIF method assesses the indentation fracture resistance (K_{IFR}), a value absolutely correlated with fracture toughness (K_{Ic})¹⁹. The fracture toughness values can be estimated by Shetty's model equation:

$$K_{Ic} = 0.0223(E/H)^{\frac{1}{2}}P/c^{\frac{3}{2}} \quad (2.9)$$

Where, E is the elastic modulus in GPa, H is the hardness in GPa, P is the applied load indentation in N and c is the distance from the center of the print to crack in m^{127, 19} shown in Fig. 2.26

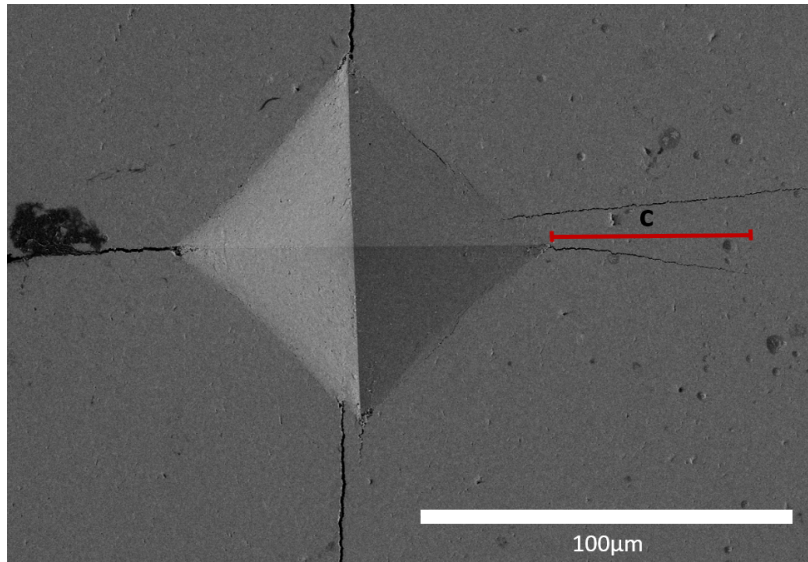


Figure 2.26: The optical image from Vickers indentation, in which is observed the cracks emerging from print corners. "c" is the crack length for K_{Ic} ¹⁹

For determination of vickers harness, we employ empirical exponential model:

$$H = H_o e^{-bp} \quad (2.10)$$

Where H is the hardness for a given porosity fraction p, H_o is the hardness at porosity zero, and b is a material constant that should be adjusted from the study of different porosities¹⁹ In this case, we can assume that H_o would be between 18.5 and 24.4 GPa, using the minimum and maximum reported values of b = 5.5 and b = 7.35 respectively¹⁹.

Chapter 3

Methodology

3.1 Synthesis of alumina/graphene oxides composites

3.1.1 Materials

Colloidal dispersions of boehmite (AlOOH - AL20) were acquired from Nyacol Nano Technologies, Inc. It has density = 1.14 g/cm^3 , dispersed sizes of 70-80 nm at 20 wt.% Al_2O_3 and up to 500 ppm of Na content. The sol is chloride-free with a very low percentage of impurities. Graphene Oxide flakes (Gs) were purchased from Graphenea Inc. and synthesized by oxidizing natural graphite powder throughout a modified Hummers method which involves two oxidation stages to guarantee single layer graphene exfoliation. The as-received 4 wt.% Gs wet-cake has a monolayer content greater than 95 % and is diluted in water to form stable dispersions to the desired Gs wt.% content. The pH of the solution is acid (around ~ 2.5), with average lateral size of the flakes smaller than 10 m, and a chemical composition of 49-56 % of carbon, 41-50 % of oxygen with a remanent sulfur content about 2-4 % for the three main elements. The aqueous Gs dispersions tend to slightly agglomerate with time. Thus, samples were systematically bath sonicated prior to use, to guarantee the highest percentage of monolayer flakes. Aqueous ammonia (NH_3) 28-30%, pH = 11.6, was acquired from Panreac. Powder of $\alpha - Al_2O_3$ seeds with 30-40 nm particle size, 99% purity, were supplied by NanoAmor, Inc. All the samples were fabricated using distilled water.

3.1.2 Graphene/Alumina Ceramics Matrix Composite (GCMC) Fabrication and Optimization

In order to optimize the dispersion and homogeneity of Gs within the material during the GCMC fabrication, we used the methodology described below and denoted as maximum volume (MV) from now on. In a typical procedure, 350 ml of water was poured into a 500 ml beaker followed by the addition of the specific amount of Gs wet-cake to obtain the desired graphene wt.% content based on the solid components. The precedent mixture was homogenized by a pulsed tip-sonication Ultrasonic Cell Disruptor (Kontes KT600), 100 W, which delivered pulses of 1.4 s separated by 0.6 s rest intervals. It is worth mentioning, that this volume was calculated in order to ensure the maximum volume in which boehmite will form a physic gel but with the lowest graphene concentration to guarantee the homogeneous distribution and stabilization of the flakes throughout the whole volume. Separately, 50 ml of commercial boehmite (AlOOH) sol was mixed with $\alpha - Al_2O_3$ seeds (2 wt.%) and homogenized under magnetic stirring during 24 hours at room temperature. This sol is labeled as (B α A) from now on. The $\alpha - Al_2O_3$ seeding promoted crystallization of alumina gel to $\alpha - Al_2O_3$ through the multiple nucleation sites⁽⁶²⁾. The B α A/Gs hidrogel was obtained upon the addition of the previously prepared BA-sol to the Gs suspension under high power tip sonication, followed by drop-by-drop addition of aqueous ammonia (NH₃) with a 50 ml burette. Gelation time occurred within 20 to 25 minutes. All dispersions and gels were kept in an ice reservoir during tip-sonication to avoid undesired sample overheating. The obtained wet gel was dried at 40 °C into an oven for 2 days. Then, dry xerogel was ground in an agate mortar, and sieved (<212 μ m). Samples were labeled according to GRALX-p for the powder samples series, where X denotes the wt.% of graphene.

The densification of these powders were carried out through reactive Spark Plasma Sintering (rSPS) using a Dr. Sinter Lab Inc. device (Model 515 S, Kanagawa, Japan, pulsed high DC current, 0–1500 A) at 1300 °C for 5 min with 75 MPa of constant uniaxial pressure (heating ramp: 100 °C/min, cooling ramp: 50 °C/min), following a previously reported recipe²⁷. The reactive sinterization process would offers a cost-effective route to produce alumina/Gs ceramics avoiding time-and-money-consuming intermediate steps, such as pre-calcination under inert atmosphere strategies, often used to promote: i.- the dehydroxylation of the aluminum hydroxides, ii.- the formation of intermediate metastable crystalline phases, iii.- the removal of moisture and undesirable traces, and iv.- the development of the stable crystalline phases of $\alpha - Al_2O_3$ ^{25,27}.

Samples were labeled according to GRALX-s for the sintered samples series, where X denotes the wt.% of graphene. The Graphene Oxide flakes content in the GCMC series varies from 0 to 6.0 wt.% in the final solid composite. Fig. 3.1 shows the schematization of the experimental process used to fabricate alumina/graphene ceramic matrix composites (GCMC) by the sol gel route combined with reactive spark plasma sintering.

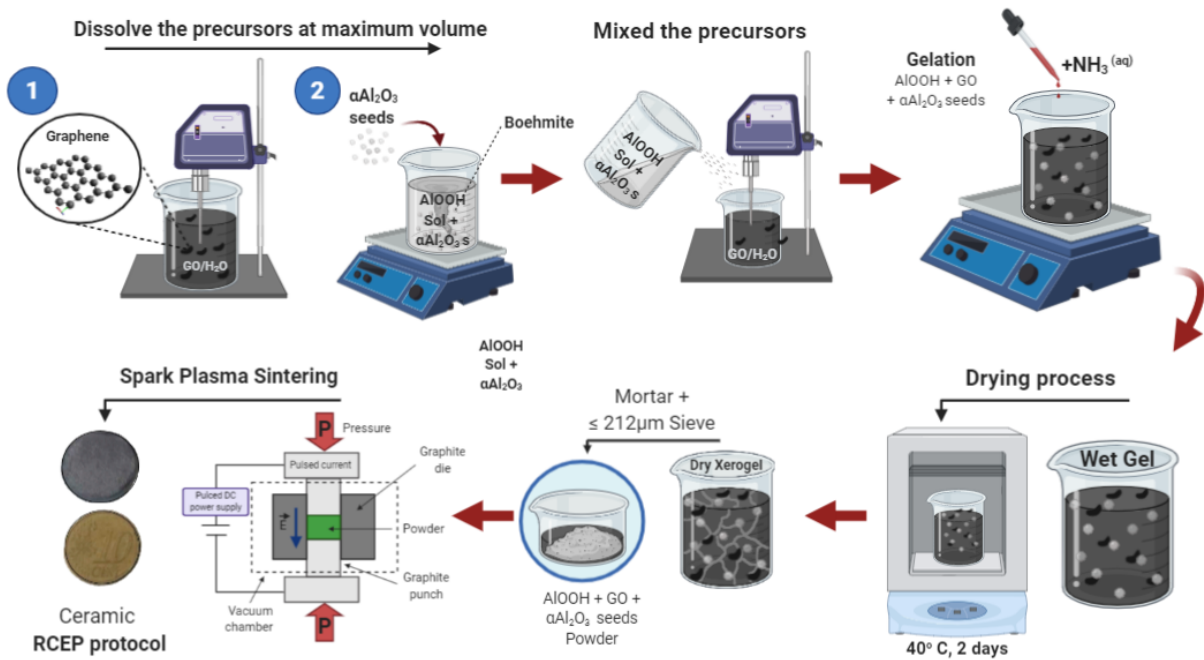


Figure 3.1: Schematic synthesis process of graphene ceramic matrix composite (GCMC), followed the procedure reported by Rivero-Antunez et al¹⁹.

3.1.3 Sample preparation for mechanical properties analysis

As shown in Fig. 3.2, powder was calcined in Spark Plasma Sintering (SPS) at 1300°C to promote the dehydroxylation of aluminum oxides (boehmite sol gel) to reach the alumina phase ($\alpha - Al_2O_3$)²⁷. After that, the sintered samples was prepared for micro and nanomechanical characterization following the RCEP protocol reported by Rivero-Antunez et al. From left to right, GO/ α -Al₂O₃ powder after the sieving process was sintered in SPS. Followed by the rectified

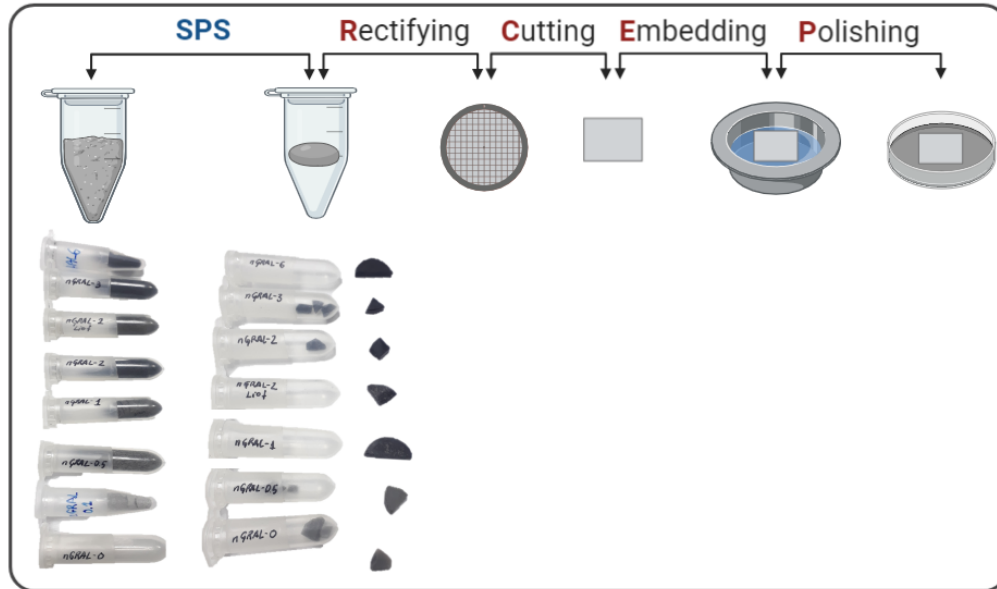


Figure 3.2: Schematic representation of RCEP preparation protocol.

process on glass sample holder ($0.5 \mu\text{m}$ diamond slurry), cuts the sample in a rectangular prism, embedded sample prism in transparent thermoplastic acrylic mounting material, and finally, polished sample for the respective characterization¹⁹.

3.2 Characterization techniques

3.2.1 X-ray Diffraction

Powder and sintered samples X-ray diffraction (XRD) patterns were recorded on a XRD Bruker diffractometer D8I-90 CuK ($\lambda = 0.1542 \text{ nm}$) operating at 40 kV and 30 mA. Sample stages were used to allow the sample to be easily placed in the X-ray beam avoiding undesired reflections. All crystalline phases present in our samples were identified following reported patterns diffraction files.

3.2.2 Thermogravimetric Analyses

Thermal gravimetric analysis (TGA) of materials was carried out using standard procedure with a STD Q600, TA Instruments. Typically, samples were heated at 10 °C/min from room temperature up to 1000 °C under an air flux (100 mL/min). We have paid special to the mass losses within the thermal range corresponding to the boehmite-dehydroxylation from 200 to 450 °C and the range in which carbonaceous phases burn out under an oxidative atmosphere from 450 to 650 °C.

3.2.3 N₂ Physisorption

Nitrogen adsorption/desorption measurements were carried out by using a Micromeritics ASAP 2010 (Accelerated Surface Area and Porosimetry System) which provides high quality surface area (BET) and porosity measurements, working at 77 K and equipped with a pressure transducer resolution of 104 mm Hg). Typically, samples were degassed at 150 °C during 2 h under a N₂ flux prior to N₂ physisorption analysis. Specific surface area, specific pore volume, pore size, and pore size distribution (PSD) were determined considering standard models for the analysis (BET and BJH, respectively).

3.2.4 Densities

The densities of all the sintered samples studied were measured by Archimedes's method using distilled water, 3.985 and 2.1 g/cm³ as the theoretical bulk density of alumina and Gs respectively. In a typical procedure, the theoretical densities of the unknown samples were computed through equation 1 and by weighting both densities, considering the weight percentage of each phase¹⁹.¹⁰⁷. In equation 3.1, ρ_A and ρ_G denote the theoretical densities of the alumina matrix and graphene respectively, while χ denotes the wt.% of Gs in the biphasic composite.

$$\rho_{theoretical} = \frac{\rho_1 \rho_2}{\rho_1 \frac{\chi}{100} + \rho_2 (1 - \frac{\chi}{100})} \quad (3.1)$$

3.2.5 Scanning Electron Microscopy

Scanning Electron Microscopy (SEM) images were acquired by using a scanning electron microscope (Hitachi S5200) with a field emission gun (SEM-FEG). The operation voltage ranged

from 5 to 20 kV, a work distance between 8 to 10 mm and magnification from 4000x to 12000x depending on the samples. Samples were typically placed on aluminum sample-holders with double-sided tape and then metalized for 60 seconds with a 20 nm thick gold layer (Sputter Coating Quorum Q105R) prior to observation.

3.2.6 Raman spectroscopy

Raman spectroscopy measurements were carried through a Horiba LabRAM HR Evolution Raman Spectrometer coupled with a CCD camera and excited by solid-state red/green laser lines ($\lambda=514$ nm and $\lambda=633$ nm) and equipped with a microscope configuration using a 100x objective and a spectral resolution of 0.35 cm^{-1} . All spectra were recorded at room temperature. Prior to spectra measurements, the spectrometer was calibrated using the 520 cm^{-1} peak of silicon as a reference. The Raman signal was recorded in the range of 100 to 3000 cm^{-1} with a 600 grooves mm^{-1} grating. In a typical measurement, the recording time was settled to 20 s with 10 acquisitions depending on the Raman intensity. All spectra were analyzed using Origin Pro software.

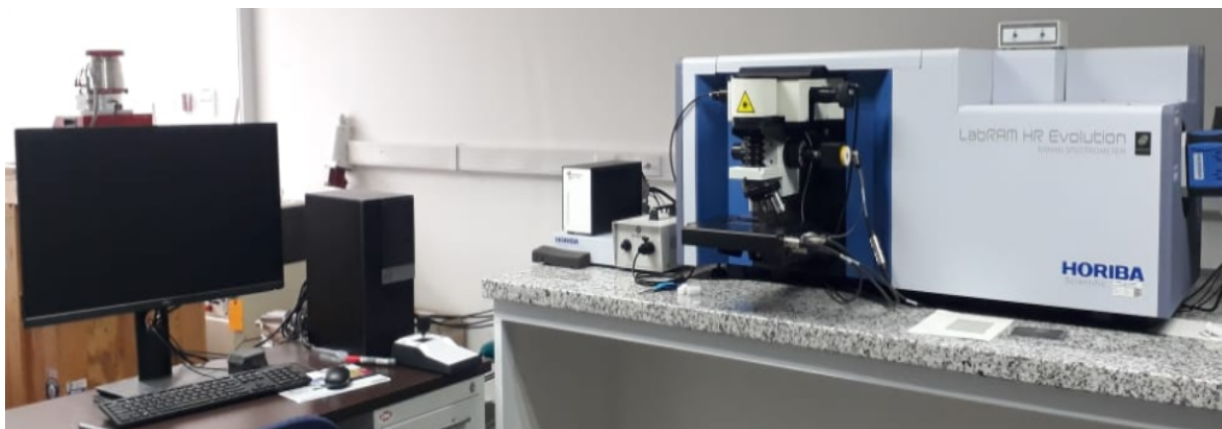


Figure 3.3: Raman equipment at Yachay Tech University

3.2.7 X-ray photoelectron spectroscopy

XPS experiments were performed at normal emission using a PHI VersaProbe III Physical-Electronics system, equipped with a 180 hemispherical electron energy analyzer and excited by a monochromatized Al $K\alpha$ source with an energy of 1486.6 eV. The X-ray spot had a diameter of 50 μm and the X-ray source was placed at 45° relative to the substrate surface. Mutipak Version 9.8.0.19 (Ulvac-phi, Inc.) was used to assess the atomic concentration. All photoemission spectra were fitted by using a convoluted Gaussian function with a Lorentzian function after a Shirley background subtraction. The software used for these purpose was Origin-Pro 2018. The Full Width at Half Maximum (FWHM) of the peaks was calculated from equation 3.2 as follow:

$$FWHM = 0.5346 * wL + \sqrt{0.2166 * wL * wL + wG * wG} \quad (3.2)$$

where “wL” is the Lorentzian FWHM, and “wG” the Gaussian FWHM



Figure 3.4: XPS equipment at Yachay Tech University

3.2.8 Mechanical properties

Hardness and fracture toughness was performed using Buehler Wilson VH1150 MicroVickers Hardness Tester with 10 kp of load and 10 s dwell time. For each sample 7 indentations were realized. Fracture toughness (KIC) was estimated by Vickers Indentation Fracture (VIF) method,

which employs Shetty's model shown in equation 1. for median cracks. This equation has been proved as the most accurate for alumina polycrystalline ceramics, showing that: .

$$K_{IC} = 0.0223(E/H)^{\frac{1}{2}}P/C^{\frac{3}{2}} \quad (3.3)$$

Where, E is the elastic modulus in GPa, H is the hardness in GPa, P is the applied load indentation in N and c is the distance from the center of the print to crack in m^{127,19}. Scanning Electron Microscopy (SEM) was employed to analyze the crack propagation, fracture surface and microstructures of GCMC.

Chapter 4

Results & Discussion

4.1 Characterization equipment

4.1.1 X-ray Diffraction

XRD is a rapid, non-destructive and common analytical experimental technique which allows us to characterize structurally all the considered boehmite and graphene precursors, as well as the sintered composite ceramics samples researched. The X-rays scattered by the crystals provide univocal information about their crystalline structure. Fig. 4.1 shows selected XRD patterns from samples series: i.- as-received graphene oxide, ii.- GRAL3-s sintered samples. Boehmite precursor and GRAL-p series (powder composites samples) exhibit typical diffraction pattern files from Boehmite (AlOOH), PDF: 00-005-0190, and were reported elsewhere (data not shown)^{27, 19}. All the XRD patterns were measured in a range of 2θ from 10° to 70° . The intensity of the diffraction peaks in Fig. 4.1 indicates the presence of the crystalline phase in the samples. The Gs diffractogram exhibits strong diffraction peaks at $2\theta = 10.53^\circ$ which corresponds to the (001) crystal planes with a spacing of 0.81 nm attributed to the presence of oxygen groups and structural defects, which are typical for graphene oxide samples^{128, 129}. In the same way, GRAL3-s shows identical diffraction peaks at 25.57, 35.13, 37.78, 43.35, 52.54, 57.48, 66.50, and 68.2° attributed to (012), (104), (110), (113), (024), (116), (214), and (300) crystallographic planes of the stable crystalline phase $\alpha\text{-Al}_2\text{O}_3$ (JCPDS-ICDD No. 46-1212)^{130, 131}. These diffractograms indicate the complete phase conversion of boehmite in -alumina, ie. corundum phase upon baking

process¹³². As expected, the crystalline signatures in both ceramic composites were comparable and correspond to pure corundum. The latter reveals that upon baking, a single and stable crystalline corundum phase is present in these samples^{27,19}. It is worth mentioning, that for the carbon contents considered in this work, the broad peaks observed in the pure Gs diffractogram were not detected in either as-prepared powders or sintered ceramic composites due to the amount of graphene was too low. In Fig. A2 of the appendix information (AI) we have plotted all the DRX diffractograms for the sintered GCMC - GRALX-s series where X denotes the solid content of Gs wt.% of the samples.

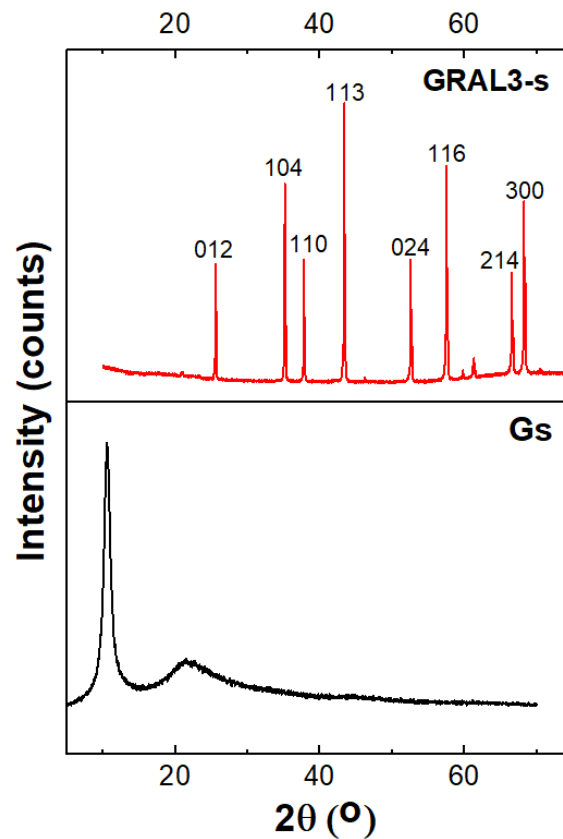


Figure 4.1: Selected X-ray powder diffraction patterns, from bottom to top: i.- as-received graphene oxide (Gs) and ii.- GRAL3-s sintered samples with 3 wt.% Gs content respectively. The stable crystalline phase $\alpha\text{-Al}_2\text{O}_3$ (corundum) is observed and follows the pattern diffraction file: $\alpha\text{-Al}_2\text{O}_3$, PDF: 00-043-1484

4.1.2 Thermogravimetric Analysis

TGA is a versatile and widely used analytical technique which allows us to determine the composite's thermal stability and its fraction of volatile phases by assessing the weight changes that occur as the sample is heated at a constant rate. In our case, TGA analysis allowed us to characterize the thermal stability of graphene and the GRAL powder composites series. In Fig. 4.2 (a) we observe the weight loss of graphene oxide at two different temperature rates 2°C and 10°C respectively. As observed on the TGA curve at a rate of 2°C min⁻¹ (black curve) in Fig. 4.2 (a), the first weight loss takes place below 100°C due to the elimination of water molecules. In the range of 100°C to 200°C, 40% of mass loss takes place suggesting the decomposition of oxygen-containing functional groups hydroxyl (-OH), carbonyl (-O) and carboxyl (-OOH) in the form of water, carbon dioxide, and carbon monoxide (Surekha, Kuila). At this temperature, it is also expected to obtain reduced graphene oxide (rGO)⁸². In spite of the absence of an oxidative atmosphere, an apparent weight loss up to 53% of mass occurred gradually for temperatures above 400°C due to the combustion of the carbon species¹³³. It is important to mention that other contributions that should be taken into account, during thermogravimetric analysis, deals with the fact that some of the outer graphene layers were gently dragged by the Argon flux during heating. The latter is corroborated by the TGA curve for Gs at a rate of 10°C min⁻¹ (red curve of Fig. 4.2 (a)), where an apparent weight loss of 100% takes place above 150°C. Likewise, during the optimization of the fabrication process for alumina/graphene ceramics matrix composite (GCMC), we tried another route by incorporating an intermediate calcination of the boehmite/graphene powders in an inert atmosphere of argon prior to sintering. These pre-calcination strategies are often used to promote the dehydroxylation of the aluminum hydroxides and the better development of the stable crystalline phase of $\alpha - Al_2O_3$ when baked. In Fig. A1 of the appendix information, macroscopic pictures of boehmite/graphene composites powders (a) before and (b) after calcination in argon atmosphere at 1200°C are observed. The researched sample is the one labeled as GRAL1-p with a nominal graphene oxide content of 1 wt.%. An evident whitening of the sample is observed and accompanied by weight losses similar to that of the graphene present in the composite, and attributed to the exfoliation of the graphene flakes dragged by the argon flux. These results led us to come to the conclusion that the reactive sinterization process would offer a cost-effective route to produce alumina/Gs ceramics avoiding time-and-money-consuming intermediate steps, such as pre-calcination under inert atmosphere.

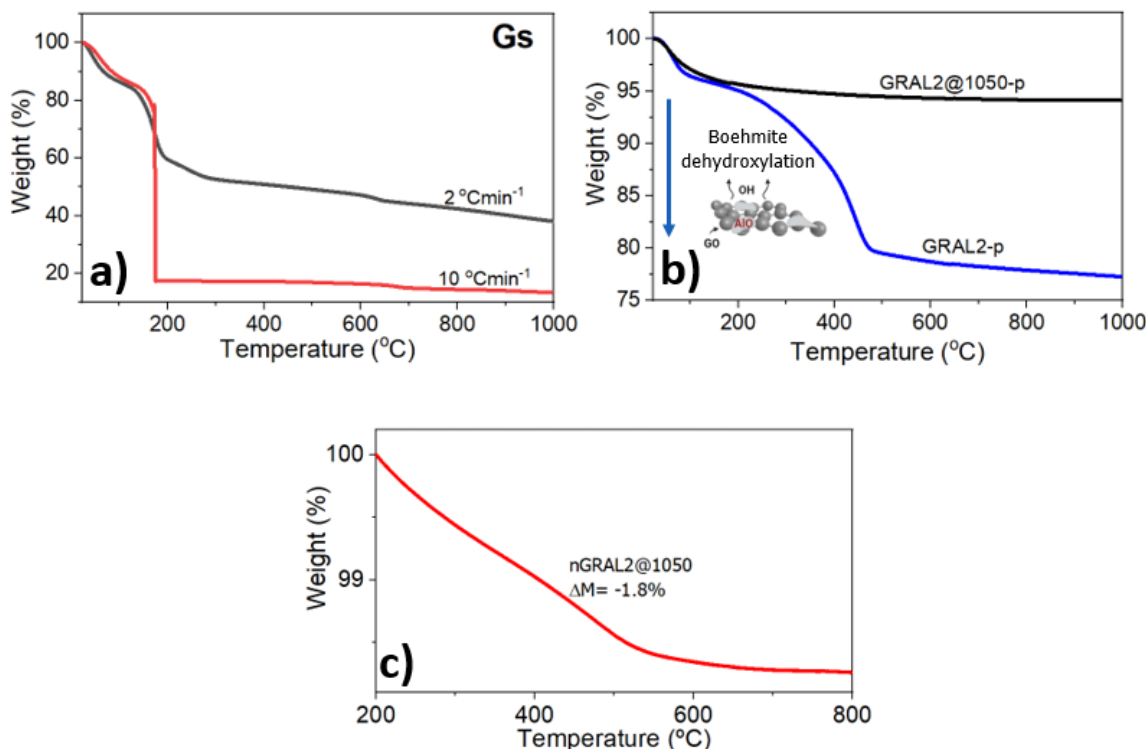


Figure 4.2: Typical Thermogravimetric analysis curves in (a-b) argon atmosphere and (c) under oxidative air atmosphere for: (a) as received graphene oxide flakes (Gs) at two different temperature rates of 2°C and 10°C respectively, (b) boehmite/graphene composites powder GRAL2-p and GRAL2@1050-p (where the label @1050 indicates that the sample was subjected to a pre calcination process at 1050°C in argon) and (c) boehmite/graphene composites GRAL2-p under oxidative atmosphere, where the weight losses due to the burnout of the carbon of the samples is observed and comparable to the expected carbon content.

Alike, Fig. 4.2 (b) shows the TGA curves in argon atmosphere for powder boehmite/graphene samples GRAL2-p and GRAL2@1050-p (calcined at 1050°C in argon). An important weight loss is observed for GRAL2-p (blue continuous line) to temperatures below 500°C, attributed to boehmite dehydroxylation which corresponds to stoichiometrically weight losses around -15%^{27,19}. On the contrary, GRAL2@1050-p (black continuous line) remains almost constant in the same region of temperatures. On the other hand, we perform TGA analysis of the GRAL2-p

sample under oxidative atmosphere conditions in order to allow carbon burnout, and assess the carbon content of the composites. This curve is plotted in Fig. 4.2 (c), and exhibits a well defined weight loss about -1.8%^{134, 132, 135}.

4.1.3 Nitrogen physisorption analysis

Nitrogen adsorption is widely used for the determination of the surface area and pore size distribution of porous materials such as ceramics. In our case, this technique has been employed to study the representative nanostructural features of the samples. The adsorption isotherms of N₂ at 77°C for the boehmite/graphene matrix composites powders (GBMC-p) series fabricated by the sol-gel method are plotted in Fig. 4.3. The most relevant parameters such as specific surface area (S_{BET}), pore size diameter (D_p) and volume (V_p) obtained by nitrogen physisorption experiments are summarized in Table 4.1. The corresponding textural characteristics for graphene oxide flakes (Gs) exhibit typically a combination of type I and IV isotherm and a hysteresis loop at a P/P₀ between 0.2 and 0.9, comparable to those reported previously (data not shown). The type of isotherms/pore were assigned according to the IUPAC (International Union of Pure and Applied Chemistry) classification. The typical specific surface area (S_{BET}) reported for Gs is 47 m²g⁻¹, with a characteristic pore diameter of 2 nm and comparable with those researched in this work^{136, 137}.

Sample	Specific surface area S_{BET} (m ² /g)	Pore volume V_P (cm ³ /g)	Pore size diameter D_P (nm)
GRAL0-p	157.22	0.335	6.86
GRAL0.5-p	156.26	0.340	7.05
GRAL1-p	168.59	0.354	6.97
GRAL2-p	164.09	0.339	6.96
GRAL3-p	165.01	0.325	7.09
GRAL6-p	99.16	0.350	10.45

Table 4.1: Specific surface area (S_{BET}), pore size diameter (D_p) and volume (V_p) obtained by nitrogen physisorption experiments for the boehmite/graphene matrix composites (GBMC-p) powders series fabricated by the sol-gel method

On the other hand, the adsorption–desorption isotherm plots for the GBMC-p in Fig. 4.3 revealed typical type IV isotherm curves and a hysteresis loop at a P/P_0 between 0.2 and 0.9 in all cases, corresponding to mesoporous structures. No significant differences are observed for the as prepared sample series containing graphene if compared with the bare boehmite xerogels. Only the composite with higher Gs wt.% content (GRAL6-p) exhibits lower specific surface area which can be attributed to some aggregation of the graphene flakes provoked during the collapse of the structure throughout the drying at room temperature and consistent with the literature, where is widely known that nanocarbon nanomaterials tend to agglomerate at higher concentrations^{1, 25, 27, 30 43}. These results, lead us to conclude that the characteristic values of the nanostructure parameters of the boehmite xerogels composites remain almost constant for Gs contents below 6 wt.%, and they are comparable to those reported previously in the literature^{27, 19, 136, 137}.

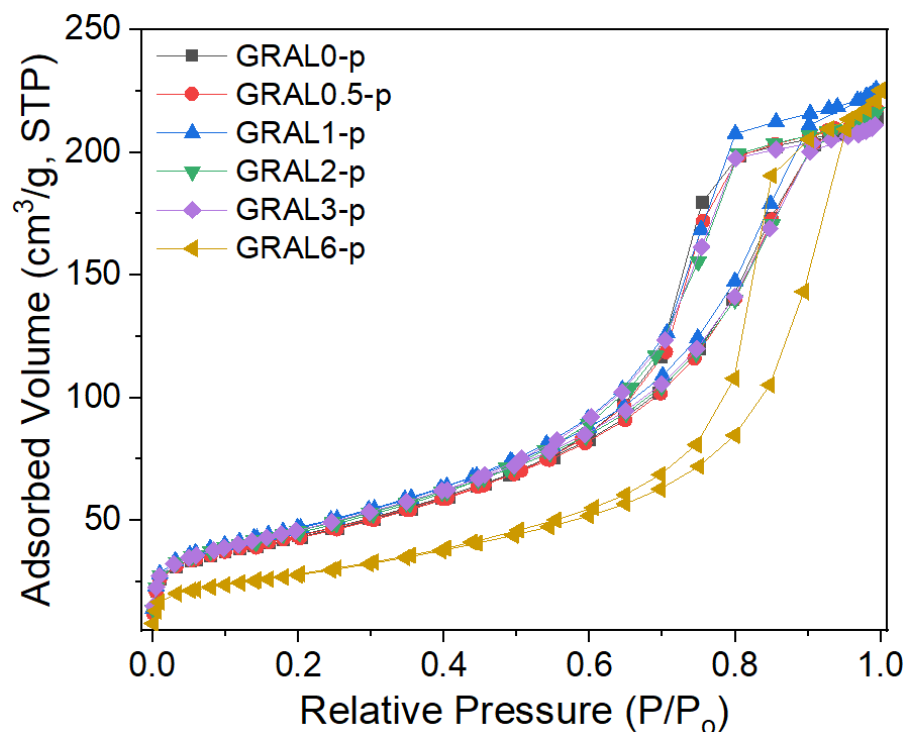


Figure 4.3: Adsorption isotherms of N₂ at 77 °C for the boehmite/graphene matrix composites powders (GCMC-p) series fabricated by the sol-gel method

4.1.4 Densities

Fully dense and fine-grained stable crystalline phases of $\alpha\text{-Al}_2\text{O}_3$ obtained at lower sinterization temperatures, were readily achieved by combining graphene nanoparticles with $\alpha\text{-Al}_2\text{O}_3$ seeds. In Table 4.2 we have summarized the theoretical density and relative density of all synthered GCMC ceramics at different Gs content obtained through the Archimedes method^{19, 138}. It is worth mentioning that the stable crystalline phase transformation of $\alpha\text{-Al}_2\text{O}_3$ occurs by nucleation and grain growth under high temperatures conditions. For instance, a low intrinsic nucleation density would result in large spacing between nucleation sites, that is why a large number of researchers have attempted to control the transformation and the final microstructure of alumina-based ceramics by using additives, by seeding or by controlling the sintering parameters. Most of these attempts focused on the improvement of the intrinsic mechanical properties by controlling not only the density but also the average grain size. In this context, MgO, carbonaceous and other 2 dimensional nanofillers have proven to be useful because they usually restrict in a singular manner the grain growth during sintering process^{4, 139, 24 19, 47, 140}. In the present work, all sample ceramic series studied exhibited almost 100% of relative densities. This feature is of major relevance regarding the mechanical properties of bulk ceramics and should be taken into consideration when performing comparisons with similar materials, besides, it might indicate that better mechanical values would be expected.

Sample	Theoretical bulk density (g/cm ³)	Relative density (%)
GRAL0-s	3.985	99.7 ± 0.03
GRAL0.5-s	3.967	99.7 ± 0.12
GRAL1-s	3.949	100.4 ± 0.70
GRAL2-s	3.914	100.2 ± 0.20
GRAL3-s	3.880	100.8 ± 0.10
GRAL6-s	3.781	100.8 ± 0.04

Table 4.2: Theoretical bulk density and relative density of all synthered GCMC ceramics at different Gs content obtained through the Archimedes method

4.1.5 Scanning Electron Microscopy

SEM was used to research the micro/nano structure in all precursors, xerogels powder and sintered samples investigated. It also provided useful information about the assessment of the quality of the graphene phase dispersion within the boehmite/graphene xerogel powders and the sintered ceramic composites^{139,24,47,140}. The surface morphology of alumina ceramic was also analyzed. In Fig. 4.4 (a) a typical SEM image for as received graphene oxide flakes (Gs) can be observed. It exhibits a non-regular shape, showing a highly wrinkled or even rippled shape which is characteristic in this kind of carbonaceous 2D nanostructures¹⁴¹. On the other hand, In Fig. 4.4 (b) a representative SEM image for the composite xerogel powder GRAL6-p fabricated by the sol-gel method is shown. The common wrinkled texture of the boehmite-like structure and morphology nanoporous xerogel is appreciated, where a well defined and separated graphene flakes can be clearly identified and comparable to those reported in the literature^{139,24,19,47,4,140}. As a matter of fact, The basic building blocks of the boehmite gel exhibit the characteristic orthorhombic shape with average size about to 25 nm in total agreement with the N₂ physisorption estimates discussed previously. SEM observations revealed the absence of graphene agglomerations suggesting the efficacy of this fabrication approach.

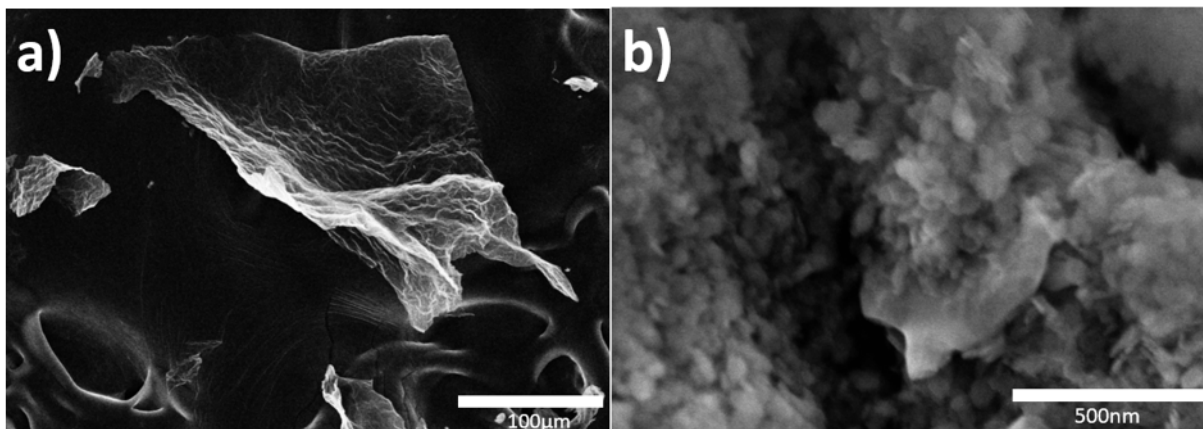


Figure 4.4: Scanning Electron Microscopy (SEM) of representative scanning electron microscopy (SEM) images for (a) as received graphene oxide flakes (Gs) and (b) composite xerogel powder GRAL6-p fabricated by the sol-gel method

On the other hand, Fig. 4.5 shows typical SEM images for sintered samples from top to bottom:

(a) GRAL0-s, (b) GRAL2-s and (c) GRAL6-s with 0, 2 and 6 wt.% Gs content respectively. These micrographs correspond with an in-plane view of the sintered samples. As expected, all samples exhibit high density and homogeneous crystal structure with evident apparent grain boundaries, which are often attributed to a well established particles rearrangement during the $\alpha\text{-Al}_2\text{O}_3$ phase transformation throughout the baking process. The previous fine-micro-grained-like structure is characteristic of stable crystalline phase $\alpha\text{-Al}_2\text{O}_3$ (corundum)^{139, 24, 47, 140, 142, 28}. Similar to the previous work, the alumina grain size of the composite material researched was below 3 microns in average, and it was inhibited, with a clear trend to smaller grain sizes when the graphene flakes additives content increased in the sintered samples. It is important to note that typically, the grain size in crystalline $\alpha\text{-Al}_2\text{O}_3$ phases ranges from 2-12 microns and above depending on the nature of the precursor properties, the additives, and sintering conditions^{24, 47, 140}. At this scale, where Gs flakes are immersed in alumina grains, we would not be able to detect any intragranular location of the carbonaceous phase. On the contrary, all these observations lead us to conclude that most of them are distributed along grain boundaries with an intergranular location, forming a barrier that obstructs the growth of alumina and comparable to those reported in the literature^{139, 24, 19, 47, 4, 140, 74, 26}. Interestingly, the sintered GRAL6-s sample showed a particular grain morphology. In spite of this sample exhibits fully dense hallmarks as indicated by N₂ physisorption measurements, an evident discontinuity between neighboring grains were observed, suggesting the presence of a porous structure, which is often observed in low-dense ceramics. These observations lead us to conclude that such behavior would be attributed to the presence of high graphene content in the sample (6 wt.%).

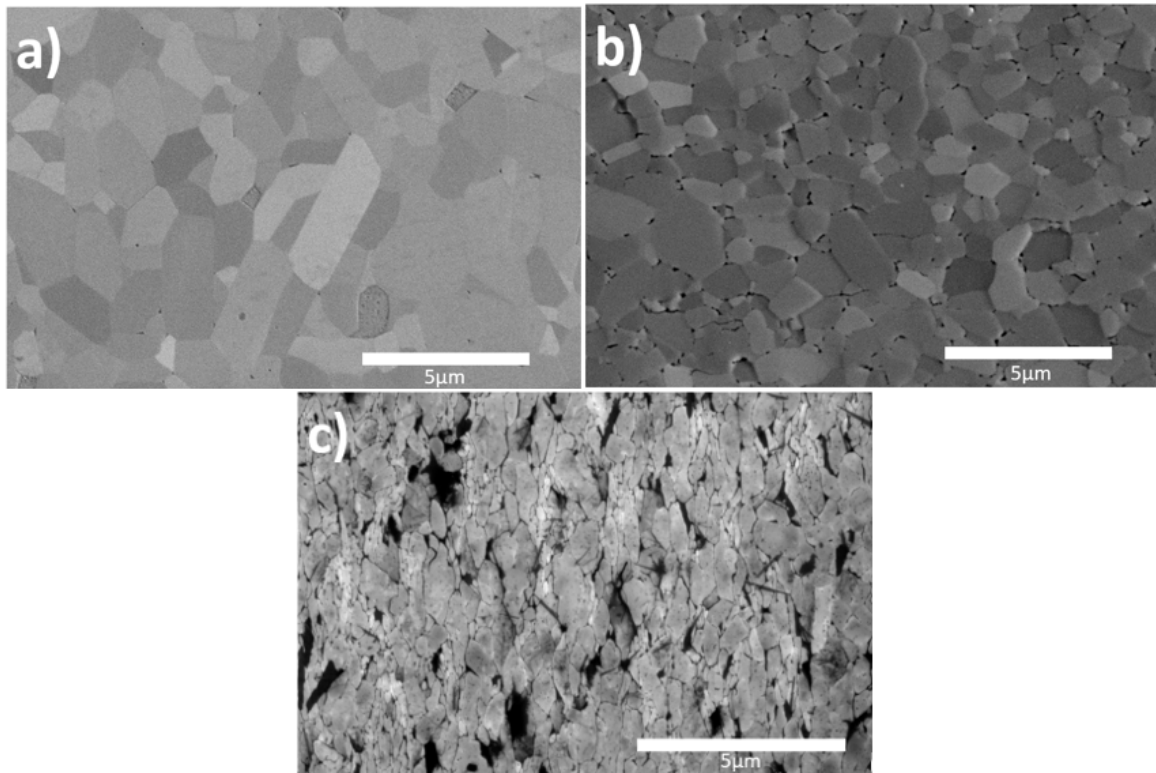


Figure 4.5: Representative scanning electron microscopy (SEM) images for sintered samples from top to bottom: (a) GRAL0-s, (b) GRAL2-s and (c) GRAL6-s with 0, 2 and 6 wt.% Gs content respectively. All samples exhibit fine-micro-grained-like characteristics of stable crystalline phase $\alpha\text{-Al}_2\text{O}_3$ (corundum).

4.1.6 Raman spectroscopy

Raman spectroscopy is a versatile and powerful technique that provides univocal information about the chemical composition of material through the vibrational modes of molecules. Clarifying the quality of crystal, stress and strain state, the amount of material present in the sample, and photoluminescence phenomenon. For nanocarbon materials composites, this technique has been widely used as an absolute fingerprint, to monitor the carbon-integrity throughout the whole sample processing^{47, 29, 27, 143}. We have used Raman spectroscopy to research all our precursors, powders and sintered ceramics based on aluminium oxide and graphene. In Fig. A3 of the appendix information (AI) we have plotted representatives Raman spectra excited by red and green laser lines for precursors. Fig. A3 (a) shows a typical spectra for graphene oxide flakes and exhibits characteristic features with a strong peak around 1350 cm^{-1} , called D-band which is related to disorder or the defect band¹⁴⁴, and G and 2D-bands located at 1600 cm^{-1} and 2700 cm^{-1} respectively¹⁴⁵. The G band offers valuable information about the vibrational modes due to in plane stretching C-C carbons atoms. As reported in the literature, depending on the numbers of graphene layers G and 2D bands would also show changes in shape, position, and intensity^{146, 147}. Fig. A3 (b) shows typical spectra for a polycrystalline boehmite with well defined bands peaking at $363, 454, 495, 671, 1048\text{ cm}^{-1}$.^{27, 148} On the other hand, Fig. A3 (c) shows typical features for a single crystalline $\alpha - \text{Al}_2\text{O}_3$ seeds phase. It is worth mentioning, that in these case, the Raman signal was collected in the range of 200 to 1800 cm^{-1} due to the presence of a strong signal attributed to the photoluminescence of the material²⁷. The major peaks observed with green lasers are located at $378, 418, 645, 751\text{ cm}^{-1}$.²⁷ Interestingly, when the samples were excited with a red laser typical, the classic bands peaks located at 378 and 418 cm^{-1} were barely observed. However, a very strong signal coming from the samples were observed at 1370 , and 1400 cm^{-1} . These characteristic bands at higher wavelengths, are commonly ascribed to the photoluminescence and demonstrate univocally the presence of Cr^{3+} ions impurities in the samples. These elements are often found as an impurity of the $\alpha - \text{Al}_2\text{O}_3$ material¹⁴⁹. Typically, ions with an incomplete 3d shell (Cr^{3+}) replace some of the Al^{3+} ions present in the $\alpha - \text{Al}_2\text{O}_3$ lattice. The Cr^{3+} ions are marked as R1 and R2 on the spectra and they are often explained in terms of the $2E \rightarrow 4A_2$ transition of the Cr^{3+} d3 configuration¹⁵⁰. For the sake of clarity, in Fig. A3 (d) we plotted the photoluminescence of $\alpha - \text{Al}_2\text{O}_3$ seeds in an absolute wavelength scale. As observed, the spike-like Cr^{3+} signal appears as a single line at 693 and 694.5 nm respectively using a red

laser¹⁴⁹. In contrast, this signal can not be observed with the green laser line, because it is out of the range. In Fig. A4, typical Raman spectra for the composite xerogel powder GRAL0-p fabricated by the sol-gel method is shown. As expected, both spectra exhibit characteristic peaks of boehmite (located at 363, 496, 677 and 1050 cm^{-1}), with a weak but observable photoluminescence signal coming from Cr^{3+} ions present as impurities in the $\alpha - \text{Al}_2\text{O}_3$ seeds and located at 1370, and 1400 cm^{-1} respectively^{148, 27, 150}. The nominal seeds solid content percentage in all the samples researched in this work is low (2 wt.%) in comparison to the boehmite.

For its part, in Fig. 4.6, Raman spectra for the composites powder GRALX-p series fabricated by the sol-gel method excited with both green and red laser lines are shown. X denotes the graphene solid content percentage within the sample: 0, 0.1, 0.5, 1, 2, 3, and 6 wt.% respectively. As expected, all the spectra exhibit well defined D, G, and 2D peaks around at 1350, 1597, and 2706 cm^{-1} respectively coming from the graphene flakes, accompanied by a very weak but observable characteristic bands of boehmite located at 363, 496, 677 and 1050 cm^{-1} ¹⁵¹. An apparent increase of the Gs signal intensity if compared with the boehmite signal is observed. For the sake of clarity, in Fig. 4.7, we have plotted the Raman peak intensities I_G/I_{boeh} ratios as a function of the Gs wt.% in the samples for 532 nm and 633 nm excitation wavelengths laser, where a clear trend is observed. As a matter of fact, this intensities ratio scales with the Gs content up to reaching a threshold above 3 wt.% Gs.

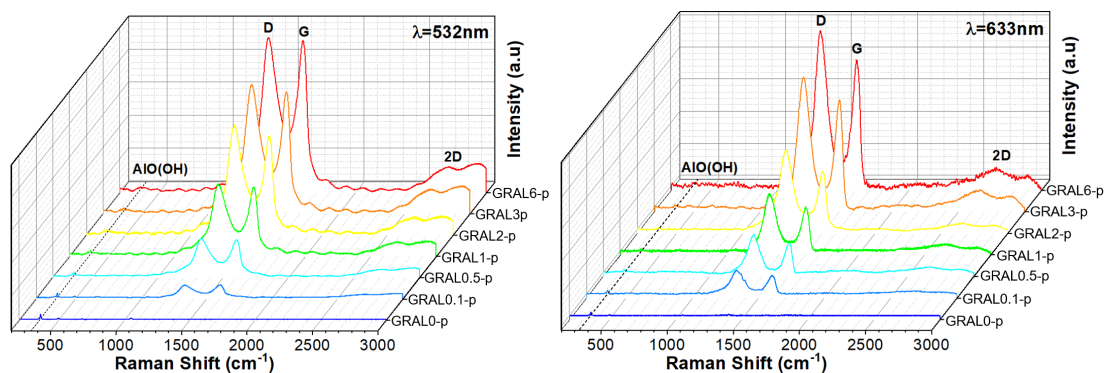


Figure 4.6: Raman spectra for the composite powder GRALX-p series fabricated by the sol-gel method excited with both green and red laser lines (X denotes the graphene solid content percentage within the sample). Spectra were normalized with respect to the boehmite(AIO(OH)) peak. D, G and 2D bands are marked. All spectra were shifted along the Y axis for clarity.

Sample	532 nm		633 nm	
	I_D/I_G	I_{2D}/I_G	I_D/I_G	I_{2D}/I_G
GRAL0.1-p	0.98	0.27	1.28	0.14
GRAL0.5-p	1.04	0.22	1.27	0.18
GRAL1-p	1.04	0.20	1.30	0.15
GRAL2-p	1.13	0.17	1.36	0.10
GRAL3-p	1.06	0.17	1.21	0.16
GRAL6-p	1.01	0.16	1.24	0.15

Table 4.3: Intensities I_D/I_G and I_{2D}/I_G ratios for Raman peaks of Bohemite/graphene composites at 532 nm and 633 nm laser

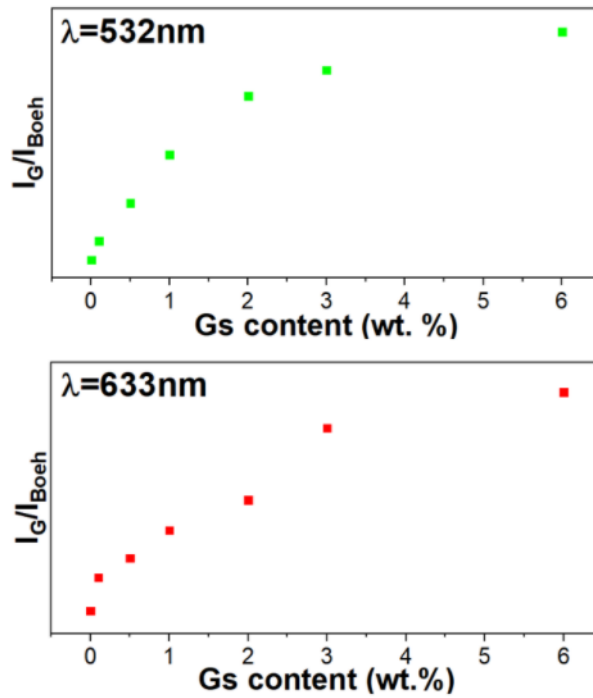


Figure 4.7: Raman peak intensities I_G/I_{boeh} ratios as a function of the Gs wt.% in the bohemite/graphene powder composites GRALX-p for 532 nm and 633 nm excitation wavelengths laser

The presence of the graphene-like fingerprints in all the samples researched (See Fig. 4.6),

demonstrates that the structure of the Gs is preserved throughout the sintered process, and they are comparable to those shown in Fig. A3¹⁵². We also have noted a slight down-shift of the 2D peak up to 2670 cm^{-1} for red laser excitation, often ascribed to a consequence of reducing the number of graphene layers in the sample¹⁴⁴. It is worth mentioning that 2D peak is very sensitive to graphene folding. Furthermore, we can characterize the level of disorder in graphene using the intensities ratio I_D/I_G of Raman spectra, is reported in the literature. If a defect density in graphene increases, I_D/I_G would begin to increase accordingly¹¹⁹. Conversely, the I_{2D}/I_G ratio provides invaluable information about crystallinity²⁷ and also allows to estimate the disorder present in the carbon network. Besides, many authors claim that it is much more reliable to use the 2D band, because it is always present in carbonaceous structures, if compared with the D band which appears only when defects arise in the carbon lattice. For instance, it is expected that I_{2D}/I_G decreases with respect to a doped structure¹⁴⁶. In Table 4.3, we have summarized the I_D/I_G and I_{2D}/I_G ratios for all boehmite/graphene composites (GRALX-p). As observed, the I_D/I_G ratios do not show significant changes, while I_{2D}/I_G ratios for green laser, continuously decrease when the concentration of Gs increases from 0.27 to 0.16, matching those reported in the literature^{119,150}. On the contrary, I_{2D}/I_G ratio for red laser exhibits undefined trend. It is worth noting that all spectra collected with a red laser present a huge photoluminescent background that might affect the accuracy of I_{2D}/I_G values.

Similarly, in Fig. 4.8, spectra for the sintered ceramic GRALX-s series fabricated by the sol-gel method and reactive spark plasma sintering (rSPS) are shown. X denotes the graphene solid content percentage within the sample: 0, 0.5, 1, 2, 3, and 6 wt.% respectively. In contrast with powder samples, the expected well defined D, G, and 2D peaks around at 1350 , 1597 , and 2706 cm^{-1} coming from the graphene flakes are observed only for samples with graphene content above 3 wt.%. Likewise, weak but noticeable characteristic bands of single crystalline $\alpha - Al_2O_3$ phase located at 378 , 418 , 578 , and 751 cm^{-1} are clearly present in the spectra²⁷, and comparable to those of the alumina precursor fingerprints shown in Fig. A2. These results corroborate that upon calcination at 1300°C (during sintering), the boehmite will transform in the crystalline $\alpha - Al_2O_3$ phase. As expected, very intense Raman peaks located at 1370 , and 1400 cm^{-1} are clearly observed, ascribed to the photoluminescence due to the Cr^{3+} ions impurities present in the samples^{150,149}. This photoluminescence often is the responsible to quench the Raman signal of other species such as the carbonaceous one. Due to the lack of G band in all ceramics samples

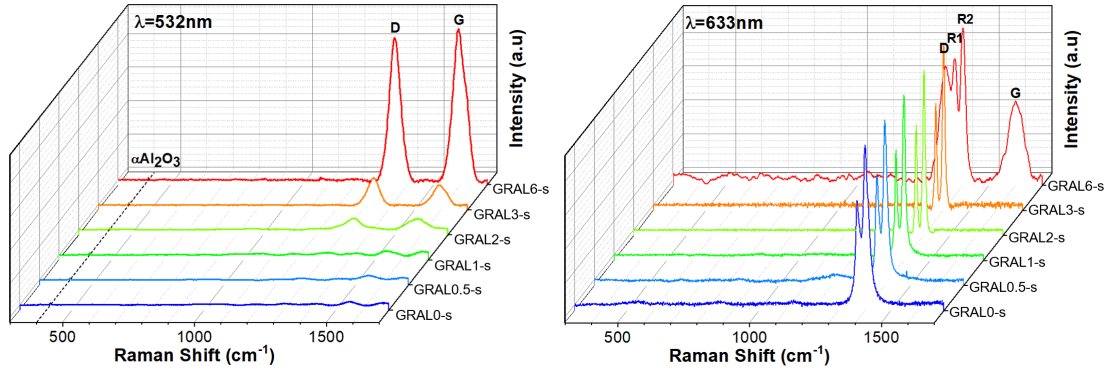


Figure 4.8: Raman spectra for the sintered ceramic GRALX-s series fabricated by the sol-gel method and reactive spark plasma sintering (rSPS), excited with both green and red laser lines (X denotes the graphene solid content percentage within the samples). Spectra were normalized with respect to the $\alpha - Al_2O_3$ peak. D, G and 2D bands and the relevant bands for $\alpha - Al_2O_3$ and Cr^{+3} ions (R1 and R2) are marked. All spectra were shifted along the Y axis for clarity

researched, we were incapable to evaluate the Raman peak intensities ratios as a function of the Gs wt.% in these samples for both 532 nm and 633 nm excitation wavelengths. However, a clear trend is observed in the Raman peak intensities I_G/I_{Alu} ratios as a function of the Gs wt.% in the alumina/graphene sintered composites ceramics GRALX-s for 532 nm excitation wavelengths. As a matter of fact, this ratio scales from 5 up to 60 with the content of graphene as observed in Table 4.4^{75, 74, 153, 26}

Sample	ID/IAlumina
GRAL0-s	0
GRAL2-s	5.2
GRAL3-s	12.19
GRAL6-s	63.75

Table 4.4: Raman peak intensities I_G/I_{Alu} ratios as a function of the Gs wt.% in the alumina/graphene sintered composites ceramics GRALX-p for 532 nm excitation wavelengths laser

4.1.7 X-ray Photoelectron Spectroscopy

The chemical compositions of the samples were analyzed by XPS. This technique allows us to analyze the composition and functional group type of our precursor, boehmite/graphene powders and alumina/graphene sintered ceramic composites (GCMC). Survey scans and closer spectra to the Al 2p and O 1s regions were performed for all samples. Also, the O1s core level signal was taken into account for the appropriate cases. Focusing first on the surveys on the alumina seeds precursor, and the bare alumina sintered samples (GRAL0-s) without graphene, in Fig. 4.10 (a) as expected, the main visible peaks in our spectra are related with Al 2p and O 1s regions and some KLL Auger transitions of oxygen. In addition, The spectrum for the alumina seed shows small peaks in the region of Fe 2p and Ni 2p, which might be attributed to some impurities coming from the samples, or often expected to be residual only in the external surfaces of our samples. Remarkably when the content of graphene increases in our samples up to 2, 3 and 6 wt.% An equivalent increase in the C region of the surveys are observed. (See Fig. 4.10 (a)). To get a deeper insight into the chemical environment of our graphene samples, a closer spectra of the O 1s and Al 2p regions were acquired for samples with and without graphene. Fig. 4.10 b-c and Fig. 4.10 d-e, respectively. At this point it is worth mentioning that each spectrum has been fitted with a Voigt profile by taking into account a Gaussian contribution associated with the resolution of our spectrometer. On the one hand, in Fig. 4.10 (b) the Al 2p signal of the GRAL sample without graphene has been fitted using a single Voigt peak characterized by a Lorentzian and Gaussian weight of a Lorentzian 0.23 and 2.01 eV, respectively, with a full width at half maximum (FWHM) of 2.13 eV. However, when the XPS spectrum from the samples with graphene (GCMC) are analyzed, it cannot be fitted exclusively by a single peak with a FWHW of 2.13 eV, and additional component at higher binding energies is need to be included in order to take into account the contribution of graphene interacting with oxygen (Fig. 4.10 (c)). On the other hand, the O1s signal without graphene is fitted exclusively by a single Voigt peak characterized by a Lorentzian and Gaussian weight of a Lorentzian 0.1 and 2.9 eV, respectively, with a full width at half maximum (FWHM) of 2.99 eV (See Fig. 4.10 (c)). Nonetheless, once graphene is included into the ceramic matrix a new component appears in the XPS spectrum at higher binding energies (See Fig. 4.10 (d)). Here, the spectra have been fitted with a Voigtian profile taking into account a Gaussian contribution associated with the resolution of our spectrometer with monochromated X-ray source. Our XPS results show that once graphene is added to our CGMC new chemical

environments are present in the O1s and Al2p regions, showing an interaction of the graphene with the alumina samples. These results are in agreement with those reported previously in the literature^{154, 28, 155, 123, 156, 44}. Fig. A5 of the appendix information shows the XPS surveys and high resolution for the precursors. We also show the details about the atomic percentage for all the samples in Table A1 to Table A5 of the appendix (AI).

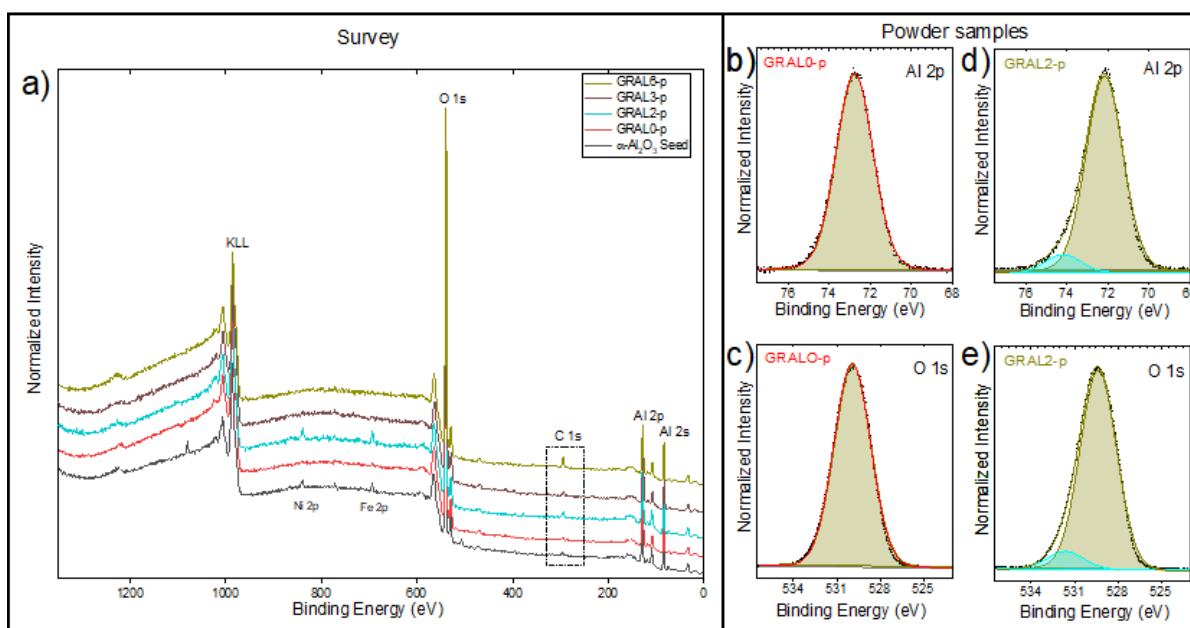


Figure 4.9: X-ray photoelectron spectroscopy spectrum for three precursor elements and the GCMC (a) general survey of the precursor and powder samples with different graphene content, (b) Al 2p spectrum of GRAL with 0% graphene (c) Al 2p spectrum of GRAL with 2% graphene, (d) O1s spectrum of GRAL with 0% graphene (e) O1s spectrum of GRAL with 2% graphene

Similarly, characteristic chemical bonds features are observed for the sintered samples (see in Fig. 4.10). For Al2p region, an additional peak at higher binding energies is included, using the same FWHM summarized in Table A.4, suggesting the interaction of graphene with aluminum. The Al 2p shoulder peak at 72.6 eV is contributed to Al–Al bonds¹⁵⁴. In Fig. 4.10 (b), GRAL2-s the remarkable peak at ~74 could be attributed to Al–O–C (aluminum oxycarbide)¹⁵⁵. Moreover, the characteristic peaks at 528 and 530–531 eV are reported for Al–O and Al–OH respectively¹⁵⁵. Comparing the Fig. 4.10 (c) and Fig. 4.10 (c) (d), a noticeable decrease of Al–OH after the

sinterization process is observed and attributed to the dehydroxylation of boehmite to α alumina phase¹⁵⁷. Moreover, as observed in the Fig. A.5 of the appendix information (AI), the XPS high resolution O1s region are shown. Indicating oxygen-containing reactive groups Al-C-O, C-C, and C-O located at 283.2 284 eV, and \sim 286 eV. Which are comparable to those reported in the literature^{158, 154, 159, 156, 140}. Comparing the atomic content percentage we noted an increase of the Al-O-C, accompanied by a significant C=C and C-O bonds decrease in sintered samples. These results suggest that rSPS mechanisms influence the initial growth of graphene at the Al_2O_3 surface¹⁵⁹. The elimination of carbonyl and hydroxyl groups activated carbon and hydrogen atoms. On the other hand, the carbon atoms are able to act as nucleation centers to form Al-O-C and Al-Al bonds (Table A.4), which lead to the segregation of the graphene-like structures comparable to those observed in the literature¹⁵⁴.

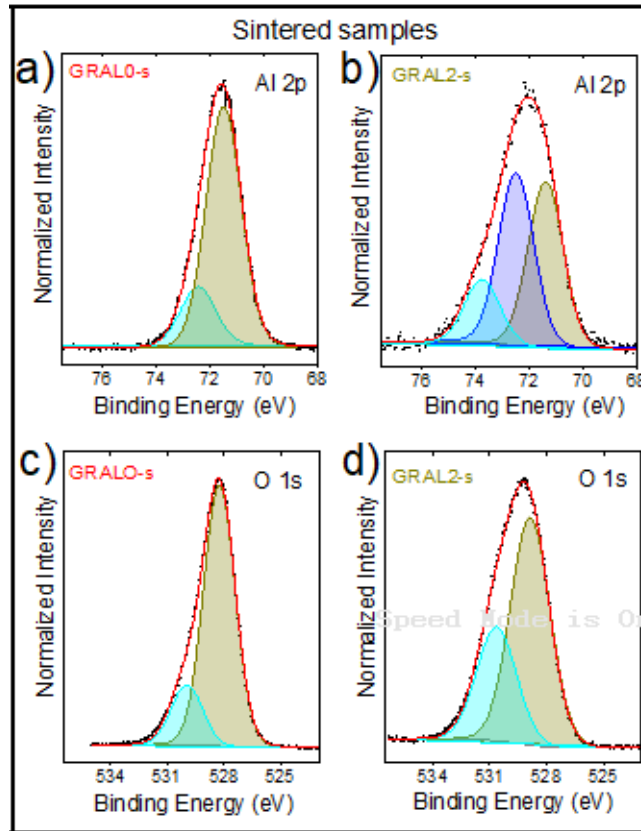


Figure 4.10: X-ray photoelectron spectroscopy spectrum for sintered samples, (a) Al 2p spectrum of GRAL with 0% graphene (c) Al 2p spectrum of GRAL with 2% graphene, (d) O1s spectrum of GRAL with 0% graphene (e) O1s spectrum of GRAL with 2% graphene

4.1.8 Mechanical properties

The Vickers hardness is plotted in Fig. 4.11 and reveals the hardness values of GCMC sintered ceramics series in both in-plane and cross-section. As observed, the in-plane hardness does not show significant changes, and values remain almost constant within the error bars. However, for the cross-section hardness, an interesting behaviour appears. The sample without graphene (bare alumina (GRAL0-s), shows typical hardness about 20.5 GPa. Then, the hardness slightly drops up to values around 18 GPa for GRAL0.5-s and scales up to 20 GPa with the graphene content. In spite of these small observed variations, they remain within the error bar and they don't exhibit any dramatical worsening of the mechanical properties upon the addition of graphene. It is worth mentioning, that the use of a theoretical Young's modulus of 400 GPa for bare alumina, to calculate the hardness would promote an underestimation of their concomitant mechanical properties as reported in the literature¹⁹. Thus, additional characterization through nanoindentation is necessary in order to obtain the most accurate and real Young's modulus experimentally from each one of the samples researched¹⁴².

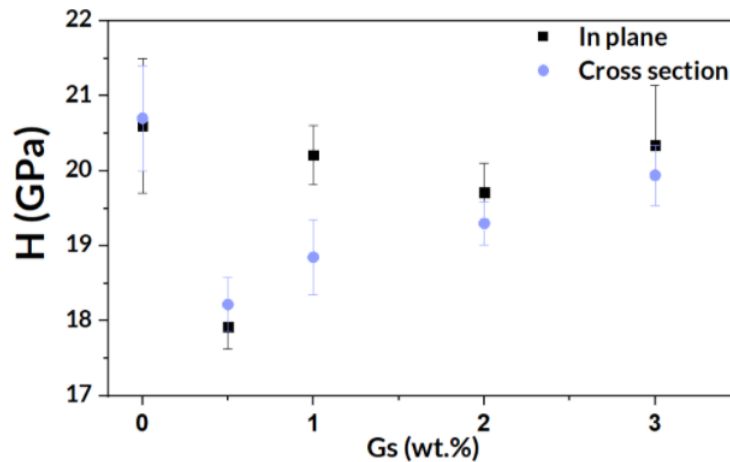


Figure 4.11: Vickers hardness for the GCMC sintered samples series. Error bars correspond with the standard deviation.

For its part, the fracture toughness for the same sample series is shown in Fig. 4.12, and computed from equation 3.3 by Vickers indentation test, using the Shetty's model. As observed, their values also remain almost constant, indicating that the mechanical properties do not show

neither appreciable improvement nor worsening. These results are a bit surprising because all samples studied showed dense structures with 100% densities. In addition, an evident decrease of the alumina grain size was observed as the graphene content increased in the samples as revealed through SEM observations. However we have noticed small black spots in all the samples studied which scales with the graphene content. These micro/nano porous present in the samples can act like fragile points being the responsible for the mechanical properties observed in the samples researched.

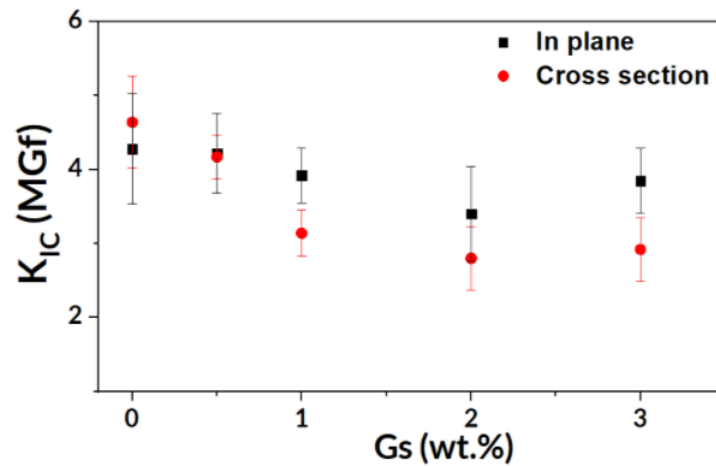


Figure 4.12: Indentation fracture toughness of GCMC sintered samples series calculated with Shetty's equation using a Young's modulus of pure alumina from literature ($E=400$ GPa). Error bars correspond with the standard deviation.

Chapter 5

Conclusions & Outlook

To summarize, in the present work we presented the fabrication of fully-dense alumina/graphene ceramic matrix composite (GCMC) by the sol-gel route and reactive spark plasma sintering, as an alternative methodology to solve one of the current challenges related with the dispersion of the graphene oxide flakes (Gs) within the composite, and to promote the formation of strong bonds between graphene flakes and the ceramic matrix such as Al-O-C oxygen bridges. In order to optimize the dispersion and homogeneity of Gs within the material during the fabrication, maximum volume (MV) strategy was used. This volume ensures the maximum volume in which boehmite will form a physic gel but with the lowest graphene concentration to guarantee the homogeneous distribution and stabilization of the flakes throughout the whole volume. For its part, reactive sinterization process would offer a cost-effective route to produce alumina/Gs ceramics avoiding time-and-money-consuming intermediate steps, such as pre-calcination under inert atmosphere. The micro/nano structure of these composites were researched by nitrogen physisorption, Raman spectroscopy, electron microscopy and X-ray Photoelectron Spectroscopy (XPS). SEM observations revealed the absence of graphene agglomerations suggesting the efficacy of this fabrication approach. Raman analyses have confirmed the integrity of the graphene along the fabrication process. XPS and Raman provide unique chemical information about the Al-O-C oxygen bridges. Mechanical features such as hardness, Young's modulus and indentation fracture toughness were comparable with those from conventional alumina/graphene CMCs, and suggest that the current approach would offer an appealing route to fabricate reinforced alumina/nanocarbon based ceramics without worsening their mechanical properties.

Appendix A

Long Appendix 1 Heading

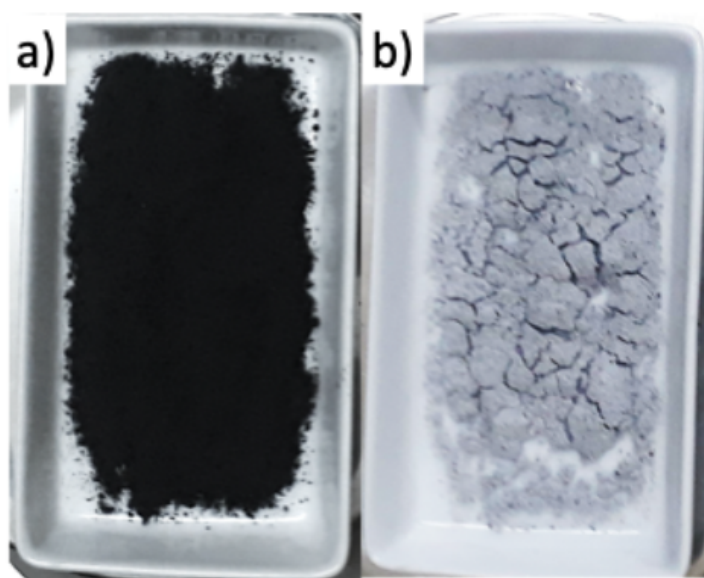


Figure A.1: Macroscopic pictures of boehmite/graphene composites powders: (a) before, (b) after calcination in argon atmosphere at 1200°C. Graphene oxide content in the sample researched corresponds with 1 wt.% and labeled as GRAL1-p

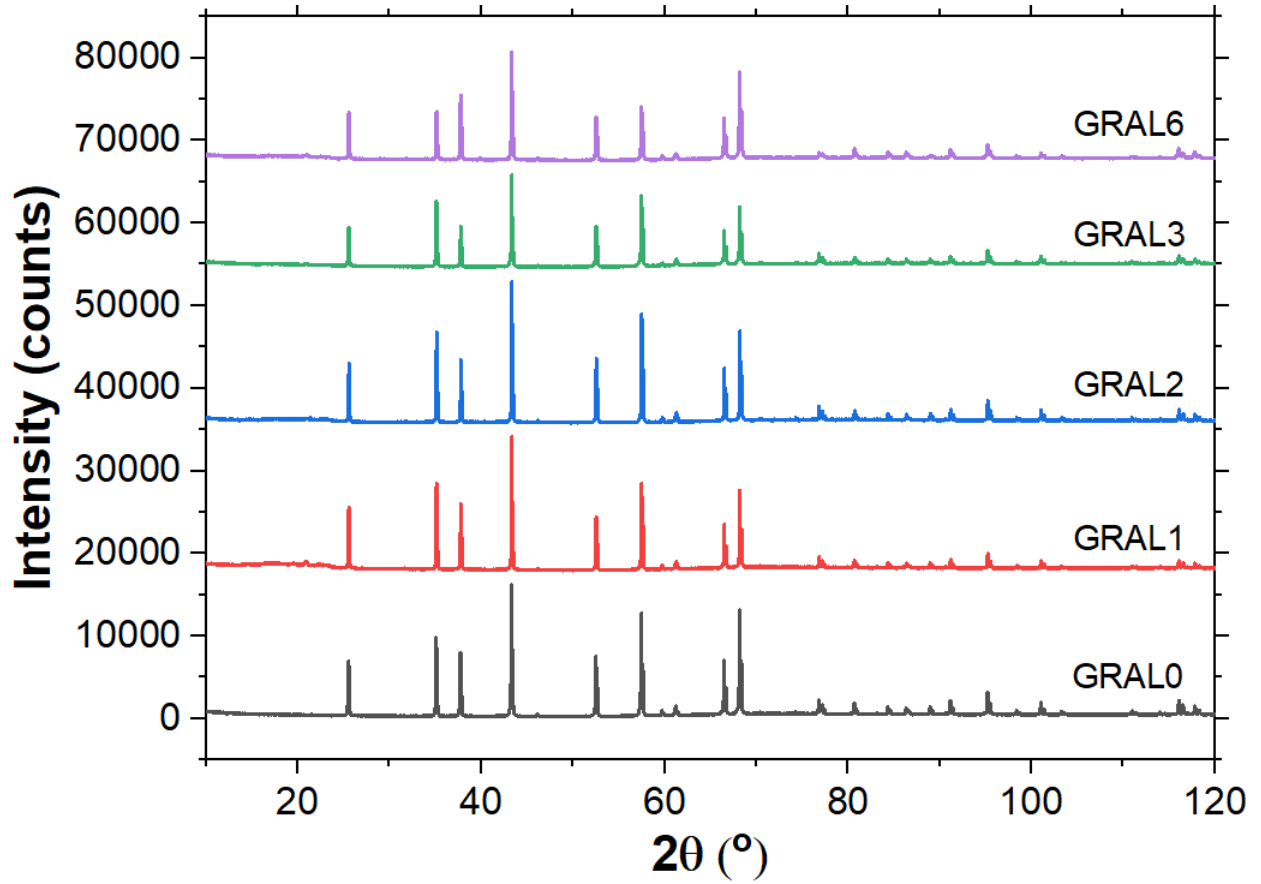


Figure A.2: XRD patterns for alumina/graphene ceramic matrix composites (GCMC) series GRALX-s. (X denotes the Gs wt.%). The stable crystalline phase α - Al_2O_3 (corundum) is observed and follows the pattern diffraction file: α - Al_2O_3 , PDF: 00-043-1484

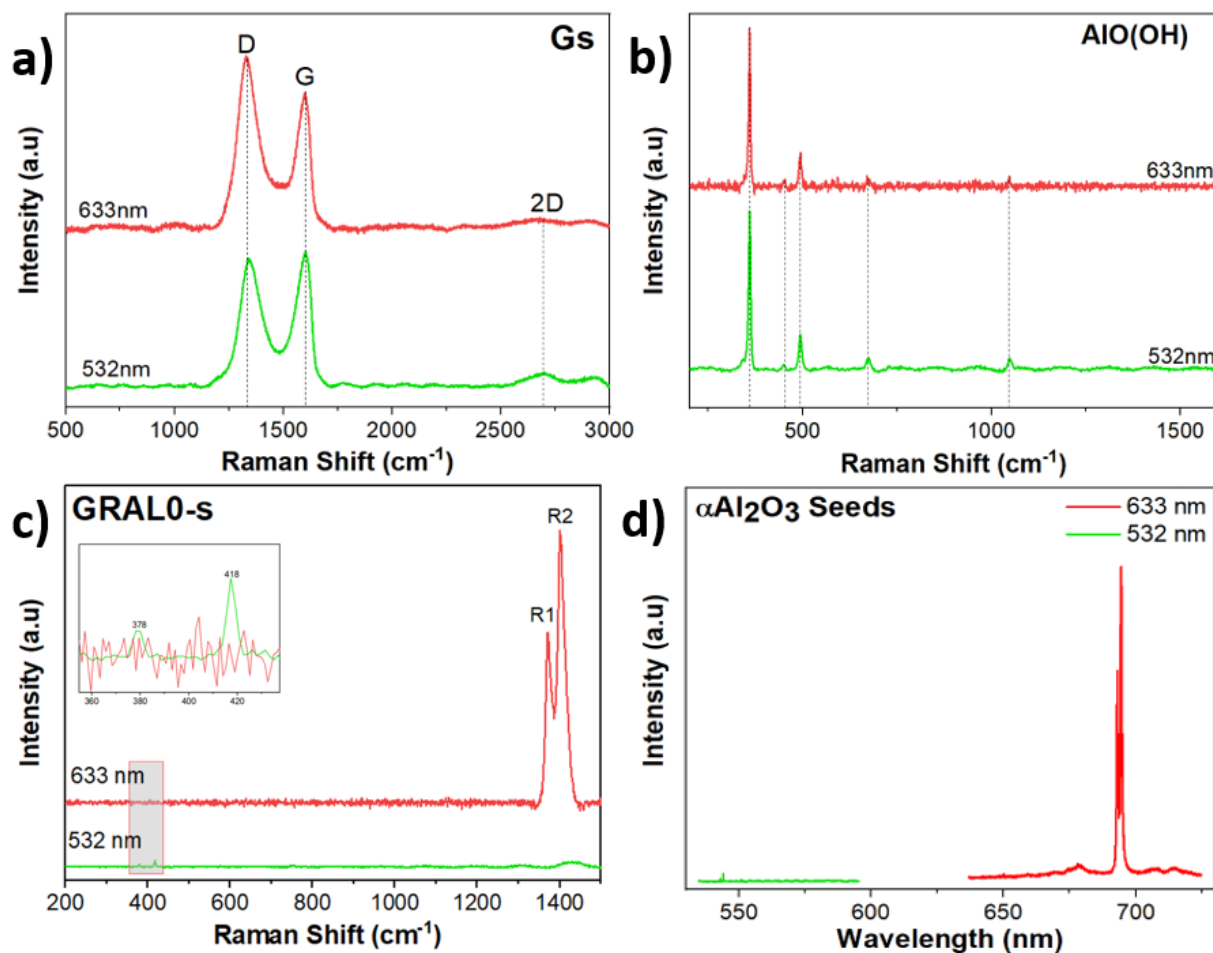


Figure A.3: Representative Raman powder spectra for: as received (a) Graphene Oxide flakes (Gs), (b) Boehmite and (c) Seeds of α -Al₂O₃. For the sake of clarity in (d), Raman spectra of α -Al₂O₃ on absolute wavelength is shown. D, G, G' and the relevant bands for Cr⁺³ ions (R1 and R2) are marked. All spectra were excited with both green and red laser lines ($\lambda = 532$ nm and $\lambda = 633$ nm), normalized either by the G band of graphene or the boehmite band, as well as shifted along the Y axis for clarity.

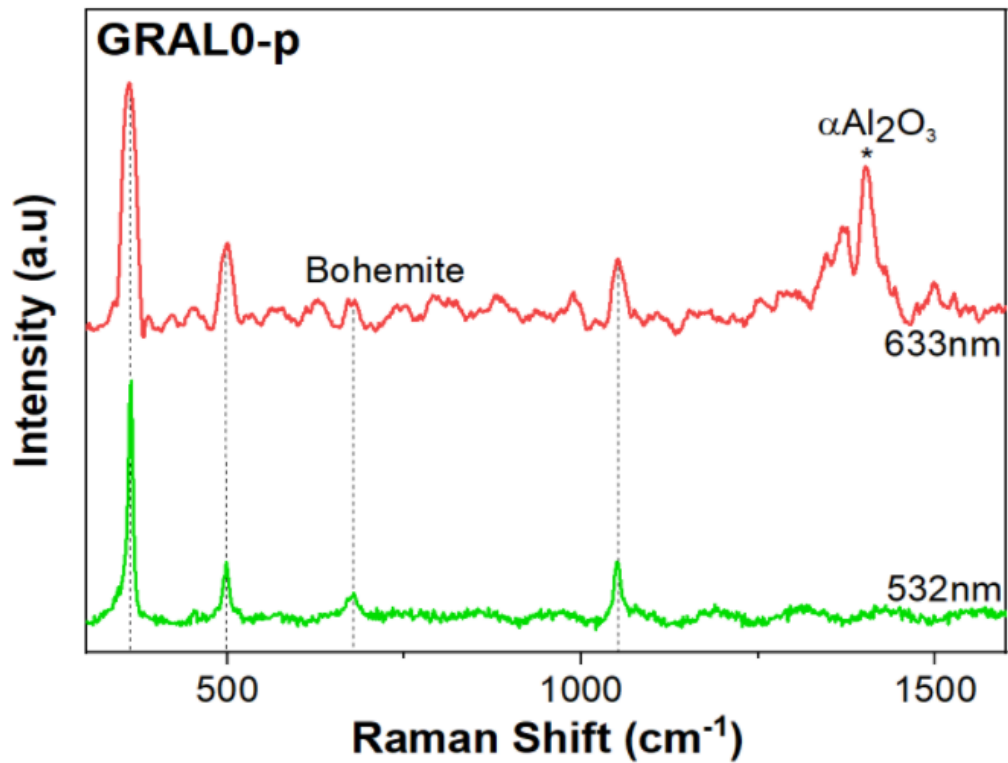


Figure A.4: Typical Raman powders spectra for the composite xerogel powder GRAL0-p fabricated by the sol-gel method. Bohemite and the relevant bands for Cr^{3+} ions (R1 and R2) are marked. All spectra were excited with both green and red laser lines ($\lambda = 532 \text{ nm}$ and $\lambda = 633 \text{ nm}$), normalized by the bohemite band and shifted along the Y axis for clarity.

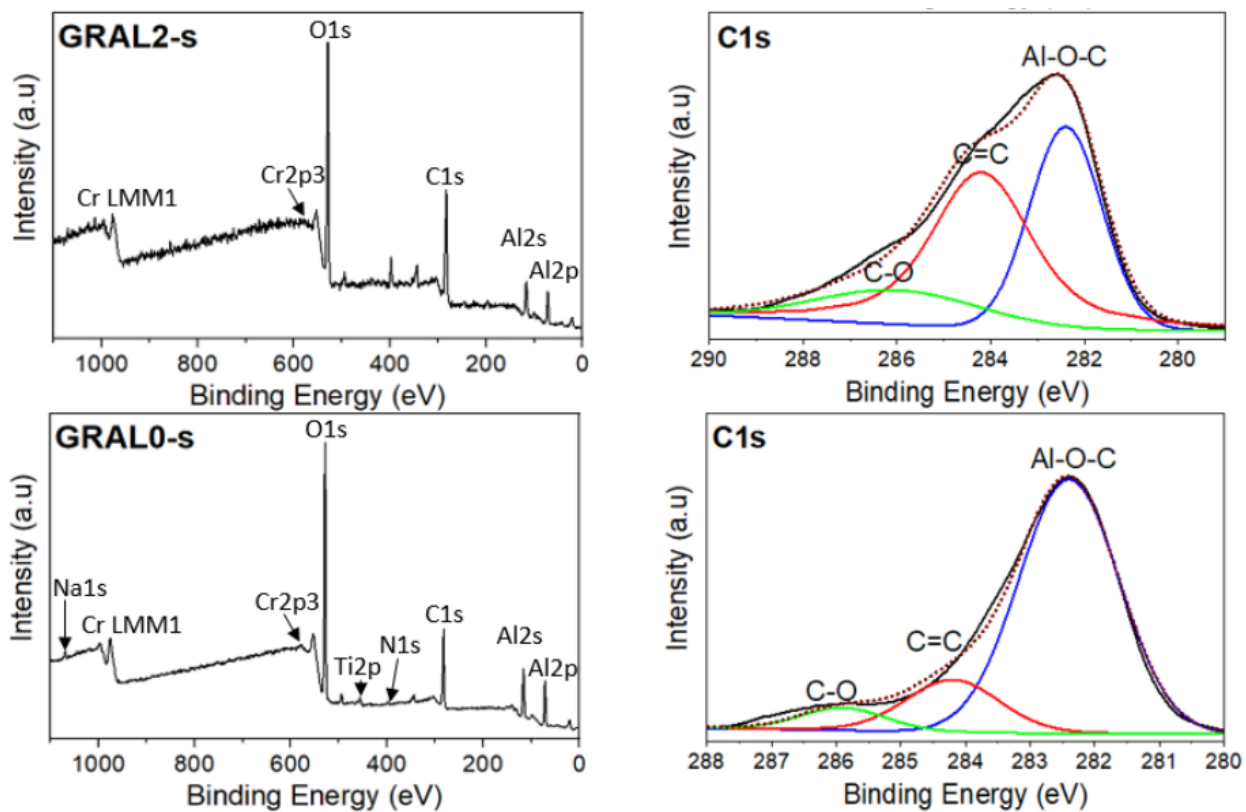


Figure A.5: XPS C1s spectrum for GRAL0-s and GRAL2-s.

Survey XPS - Atomic percentage of elements			
Sample	Boehmite	α -Al ₂ O ₃	GO
Element	Atomic percentage %		
Al2p	14.6	21.3	-
C1s	3.4	11.9	65.6
O1s	80.8	64.6	33.8
Cr _{2p} 3	1.2	1.3	0.3
Na1s	-	0.8	0.3

Table A.1: Atomic percentage of precursor elements

Survey XPS - Atomic percentage of elements		
Sample	GRAL0-p	GRAL2-p
Element	Atomic percentage %	
Al2p	20.1	18
C1s	5.7	6
O1s	73	75.1
Cr _{2p} 3	0.8	0.9
Fe2p3	0.4	-

Table A.2: Atomic percentage of powders samples

Survey XPS - Atomic percentage of elements		
Sample	GRAL0-s	GRAL2-s
Element	Atomic percentage %	
Al2p	6.5	6
C1s	37.5	51.6
O1s	52.6	38
Cr _{2p3}	1.1	0.5
N1s	1	4.3
Na1s	0.4	-
Ti1p	0.8	-

Table A.3: Atomic percentage of sintered samples

Sample	Binding Energy	Peak width	Content
Al2p			
GRAL0-s	71.46	1.56	79.47
	72.43	1.56	20.52
GRAL2-s	71.43	1.56	41.23
	72.48	1.56	42.69
	73.77	1.56	16.07
O1s			
GRAL0-s	528.14	1.98	81.05
	530.02	1.98	18.94
GRAL2-s	528.91	2.48	66.60
	530.69	2.48	33.39

Table A.4: Detail information of typical XPS results of Al2p, and O1s spectra of sintered samples: binding energy, peak width, and content percentage.

Bibliography

- [1] Porwal, H.; Grasso, S.; Reece, M. Review of graphene–ceramic matrix composites. *Advances in Applied Ceramics* **2013**, *112*, 443–454.
- [2] Drouet, C.; Leriche, A.; Hampshire, S.; Kashani, M.; Stamboulis, A.; Iafisco, M.; Tampieri, A. *Advances in Ceramic Biomaterials*; Elsevier, 2017; pp 21–82.
- [3] Peintinger, M. F.; Kratz, M. J.; Bredow, T. Quantum-chemical study of stable, meta-stable and high-pressure alumina polymorphs and aluminum hydroxides. *Journal of Materials Chemistry A* **2014**, *2*, 13143–13158.
- [4] Guo, H.; Li, W. Effects of Al₂O₃ crystal types on morphologies, formation mechanisms of mullite and properties of porous mullite ceramics based on kyanite. *Journal of the European Ceramic Society* **2018**, *38*, 679–686.
- [5] Inam, F.; Bhat, B. R.; Vo, T.; Daoush, W. M. Structural health monitoring capabilities in ceramic–carbon nanocomposites. *Ceramics International* **2014**, *40*, 3793–3798.
- [6] others,, *et al.* Reduced graphene oxide (rGO) based wideband optical sensor and the role of Temperature, Defect States and Quantum Efficiency. *Scientific reports* **2018**, *8*, 1–13.
- [7] Sheka, E. F. Dirac material graphene. *Reviews on Advanced Materials Science* **2018**, *53*, 1–28.
- [8] Markandan, K.; Chin, J. K.; Tan, M. T. Recent progress in graphene based ceramic composites: a review. *Journal of Materials Research* **2017**, *32*, 84–106.

- [9] Dervin, S.; Pillai, S. C. *Sol-Gel Materials for Energy, Environment and Electronic Applications*; Springer, 2017; pp 1–22.
- [10] Epp, J. *Materials characterization using nondestructive evaluation (NDE) methods*; Elsevier, 2016; pp 81–124.
- [11] Thompson, J.; Braun, G.; Tierney, D.; Wessels, L.; Schmitzer, H.; Rossa, B.; Wagner, H.; Dultz, W. Rosalind Franklin’s X-ray photo of DNA as an undergraduate optical diffraction experiment. *American Journal of Physics* **2018**, *86*, 95–104.
- [12] Arvieu, C.; Galy, C.; Le Guen, E.; Lacoste, E. Relative Density of SLM-Produced Aluminum Alloy Parts: Interpretation of Results. *Journal of Manufacturing and Materials Processing* **2020**, *4*, 83.
- [13] Shah, F.; Ruscsak, K.; Palmquist, A. 50 years of scanning electron microscopy of bone—a comprehensive overview of the important discoveries made and insights gained into bone material properties in health, disease, and taphonomy. *Bone Research* **2019**, *7*.
- [14] Jafari, M. J. Application of Vibrational Spectroscopy in Organic Electronics. Ph.D. thesis, Linköping University Electronic Press, 2017.
- [15] McCreery, R. L. *Raman spectroscopy for chemical analysis*; John Wiley & Sons, 2005; Vol. 225.
- [16] Baker, M. J.; Hughes, C. S.; Hollywood, K. A. Raman spectroscopy. *Biophotonics: Vibrational Spectroscopic Diagnostics* **2016**, 3–1.
- [17] Wagner, S.; Niklaus, F.; Mokwa, W.; Lemme, M. C. 2D materials for piezoresistive strain gauges and membrane based nanoelectromechanical systems. Ph.D. thesis, Rheinisch-Westfälische Technische Hochschule Aachen, 2018.
- [18] Alhashmy, H. Fabrication of aluminium matrix composites (amcs) by squeeze casting technique using carbon fiber as reinforcement. Ph.D. thesis, Université d’Ottawa/University of Ottawa, 2012.

- [19] Rivero-Antúnez, P.; Cano-Crespo, R.; Esquivias, L.; de la Rosa-Fox, N.; Zamora-Ledezma, C.; Domínguez-Rodríguez, A.; Morales-Flórez, V. Mechanical characterization of sol-gel alumina-based ceramics with intragranular reinforcement of multiwalled carbon nanotubes. *Ceramics International* **2020**,
- [20] Piconi, C.; Maccauro, G. Zirconia as a ceramic biomaterial. *Biomaterials* **1999**, *20*, 1–25.
- [21] McEntire, B.; Bal, B. S.; Rahaman, M.; Chevalier, J.; Pezzotti, G. Ceramics and ceramic coatings in orthopaedics. *Journal of the European Ceramic Society* **2015**, *35*, 4327–4369.
- [22] Ong, Y. T.; Ahmad, A. L.; Zein, S. H. S.; Tan, S. H. A review on carbon nanotubes in an environmental protection and green engineering perspective. *Brazilian Journal of Chemical Engineering* **2010**, *27*, 227–242.
- [23] Rasheed, A.; Khalid, M.; Rashmi, W.; Gupta, T.; Chan, A. Graphene based nanofluids and nanolubricants—Review of recent developments. *Renewable and Sustainable Energy Reviews* **2016**, *63*, 346–362.
- [24] Porwal, H.; Tatarko, P.; Grasso, S.; Khaliq, J.; Dlouhý, I.; Reece, M. J. Graphene reinforced alumina nano-composites. *Carbon* **2013**, *64*, 359–369.
- [25] Liu, Y.; Jiang, X.; Shi, J.; Luo, Y.; Tang, Y.; Wu, Q.; Luo, Z. Research on the interface properties and strengthening–toughening mechanism of nanocarbon-toughened ceramic matrix composites. *Nanotechnology Reviews* **2020**, *9*, 190–208.
- [26] Centeno, A.; Rocha, V. G.; Alonso, B.; Fernández, A.; Gutierrez-Gonzalez, C. F.; Torrecillas, R.; Zurutuza, A. Graphene for tough and electroconductive alumina ceramics. *Journal of the European Ceramic Society* **2013**, *33*, 3201–3210.
- [27] Esquivias, L.; Rivero-Antúnez, P.; Zamora-Ledezma, C.; Domínguez-Rodríguez, A.; Morales-Flórez, V. Intragranular carbon nanotubes in alumina-based composites for reinforced ceramics. *Journal of Sol-Gel Science and Technology* **2019**, *90*, 162–171.
- [28] Shin, J.-H.; Choi, J.; Kim, M.; Hong, S.-H. Comparative study on carbon nanotube-and reduced graphene oxide-reinforced alumina ceramic composites. *Ceramics International* **2018**, *44*, 8350–8357.

- [29] Dresselhaus, M. S.; Jorio, A.; Hofmann, M.; Dresselhaus, G.; Saito, R. Perspectives on carbon nanotubes and graphene Raman spectroscopy. *Nano letters* **2010**, *10*, 751–758.
- [30] Torres-Canas, F. J.; Blanc, C.; Zamora-Ledezma, C.; Silva, P.; Anglaret, E. Dispersion and individualization of SWNT in surfactant-free suspensions and composites of hydrosoluble polymers. *The Journal of Physical Chemistry C* **2015**, *119*, 703–709.
- [31] Leonov, A. A.; Khasanov, A. O.; Danchenko, V.; Khasanov, O. L. Spark plasma sintering of ceramic matrix composite based on alumina, reinforced by carbon nanotubes. 2017.
- [32] Yazdani, B.; Xia, Y.; Ahmad, I.; Zhu, Y. Graphene and carbon nanotube (GNT)-reinforced alumina nanocomposites. *Journal of the European Ceramic Society* **2015**, *35*, 179–186.
- [33] He, T.; Li, J.; Wang, L.; Zhu, J.; Jiang, W. Preparation and consolidation of alumina/graphene composite powders. *Materials transactions* **2009**, *50*, 749–751.
- [34] Choi, W.; Lahiri, I.; Seelaboyina, R.; Kang, Y. S. Synthesis of graphene and its applications: a review. *Critical Reviews in Solid State and Materials Sciences* **2010**, *35*, 52–71.
- [35] Li, D.; Kaner, R. B. Graphene-based materials. *Nat Nanotechnol* **2008**, *3*, 101.
- [36] Stoller, M. D.; Park, S.; Zhu, Y.; An, J.; Ruoff, R. S. Graphene-based ultracapacitors. *Nano letters* **2008**, *8*, 3498–3502.
- [37] Liang, J.; Wang, Y.; Huang, Y.; Ma, Y.; Liu, Z.; Cai, J.; Zhang, C.; Gao, H.; Chen, Y. Electromagnetic interference shielding of graphene/epoxy composites. *Carbon* **2009**, *47*, 922–925.
- [38] Walker, L. S.; Marotto, V. R.; Rafiee, M. A.; Koratkar, N.; Corral, E. L. Toughening in graphene ceramic composites. *ACS nano* **2011**, *5*, 3182–3190.
- [39] Goenka, S.; Sant, V.; Sant, S. Graphene-based nanomaterials for drug delivery and tissue engineering. *Journal of Controlled Release* **2014**, *173*, 75–88.
- [40] others., *et al.* Graphene-based liquid crystal device. *Nano letters* **2008**, *8*, 1704–1708.

- [41] Wang, X.; Zhi, L.; Müllen, K. Transparent, conductive graphene electrodes for dye-sensitized solar cells. *Nano letters* **2008**, *8*, 323–327.
- [42] Mittal, G.; Dhand, V.; Rhee, K. Y.; Park, S.-J.; Lee, W. R. A review on carbon nanotubes and graphene as fillers in reinforced polymer nanocomposites. *Journal of Industrial and Engineering Chemistry* **2015**, *21*, 11–25.
- [43] Zakri, C.; Blanc, C.; Grelet, E.; Zamora-Ledezma, C.; Puech, N.; Anglaret, E.; Poulin, P. Liquid crystals of carbon nanotubes and graphene. *Philosophical Transactions of the Royal Society A: Mathematical, Physical and Engineering Sciences* **2013**, *371*, 20120499.
- [44] Saha, A.; Basiruddin, S.; Rayb, S.; Royc, S.; Janaa, N. R. Electronic supplementary information Functionalized graphene and graphene oxide solution via polyacrylate coating.
- [45] Dasari, B. L.; Morshed, M.; Nouri, J. M.; Brabazon, D.; Naher, S. Mechanical properties of graphene oxide reinforced aluminium matrix composites. *Composites Part B: Engineering* **2018**, *145*, 136–144.
- [46] Hrubovčáková, M.; Múdra, E.; Bureš, R.; Kovalčíková, A.; Sedlák, R.; Girman, V.; Hvizdoš, P. Microstructure, fracture behaviour and mechanical properties of conductive alumina based composites manufactured by SPS from graphenated Al₂O₃ powders. *Journal of the European Ceramic Society* **2020**, *40*, 4818–4824.
- [47] Zhou, B.-Y.; Fan, S.-J.; Fan, Y.-C.; Zheng, Q.; Zhang, X.; Jiang, W.; Wang, L.-J. Recent progress in ceramic matrix composites reinforced with graphene nanoplatelets. *Rare Metals* **2019**, 1–16.
- [48] Golla, B. R.; Mukhopadhyay, A.; Basu, B.; Thimmappa, S. K. Review on ultra-high temperature boride ceramics. *Progress in Materials Science* **2020**, *111*, 100651.
- [49] Mukhopadhyay, A.; Raju, G.; Basu, B. *MAX phases and ultra-high temperature ceramics for extreme environments*; IGI Global, 2013; pp 49–99.
- [50] Saeedi Heydari, M.; Ghezavati, J.; Abbasgholipour, M.; Mohammadi Alasti, B. Various types of ceramics used in radome: A review. *Scientia Iranica* **2017**, *24*, 1136–1147.

- [51] Fahrenholtz, W. G.; Hilmas, G. E. Ultra-high temperature ceramics: materials for extreme environments. *Scripta Materialia* **2017**, *129*, 94–99.
- [52] Li, J.; Hastings, G. *Handbook of biomaterial properties*; Springer, 2016; pp 339–352.
- [53] Manicone, P. F.; Iommetti, P. R.; Raffaelli, L. An overview of zirconia ceramics: basic properties and clinical applications. *Journal of dentistry* **2007**, *35*, 819–826.
- [54] Scales, J. T.; Goddard, D. Prosthetic acetabular devices. 1972; US Patent 3,698,017.
- [55] Mittelmeier, H.; Karpf, K.; Moser, H. Hip joint prosthesis. 1975; US Patent 3,894,297.
- [56] Zeibig, A.; Locke, H. Ceramic implant. 1976; US Patent 3,979,779.
- [57] Xia, H.; Zhang, X.; Shi, Z.; Zhao, C.; Li, Y.; Wang, J.; Qiao, G. Mechanical and thermal properties of reduced graphene oxide reinforced aluminum nitride ceramic composites. *Materials Science and Engineering: A* **2015**, *639*, 29–36.
- [58] De Aza, A.; Chevalier, J.; Fantozzi, G.; Schehl, M.; Torrecillas, R. Crack growth resistance of alumina, zirconia and zirconia toughened alumina ceramics for joint prostheses. *Biomaterials* **2002**, *23*, 937–945.
- [59] Ito, H.; Nunome, K.; Sugimoto, M.; Tanaka, K.; Matsubara, K.; Yamamoto, Y.; Ito, M. Alumina-based sintered body insulator for spark plugs. 2003; US Patent 6,559,579.
- [60] Buchberger, W.; Winsauer, K. Alumina as stationary phase for ion chromatography and column-coupling techniques. *Journal of Chromatography A* **1989**, *482*, 401–406.
- [61] Lei, J.-F.; Will, H. A. Thin-film thermocouples and strain-gauge technologies for engine applications. *Sensors and Actuators A: Physical* **1998**, *65*, 187–193.
- [62] Shelleman, R.; Messing, G.; Kumagai, M. Alpha alumina transformation in seeded boehmite gels. *Journal of Non-Crystalline Solids* **1986**, *82*, 277–285.
- [63] Trunov, M. A.; Schoenitz, M.; Zhu, X.; Dreizin, E. L. Effect of polymorphic phase transformations in Al₂O₃ film on oxidation kinetics of aluminum powders. *Combustion and flame* **2005**, *140*, 310–318.

- [64] Trunov, M. A.; Schoenitz, M.; Dreizin, E. L. Ignition of aluminum powders under different experimental conditions. *Propellants, Explosives, Pyrotechnics: An International Journal Dealing with Scientific and Technological Aspects of Energetic Materials* **2005**, *30*, 36–43.
- [65] Fang, C.; Pu, M.; Zhou, X.; Lei, W.; Pei, L.; Wang, C. Facile Preparation of Hydrophobic Aluminum Oxide Film via Sol-Gel Method. *Frontiers in Chemistry* **2018**, *6*, 308.
- [66] Rother, R. N.; DeArmitt, C. Composites using nano-fillers. *Particulate-filled polymer composites* **2003**, 489–514.
- [67] Marquis, D. M.; Chivas-Joly, C.; Guillaume, É. *Properties of nanofillers in polymer*; INTECH Open Access Publisher, 2011.
- [68] Malek, O.; González-Julián, J.; Vleugels, J.; Vanderauwera, W.; Lauwers, B.; Belmonte, M. Carbon nanofillers for machining insulating ceramics. *Materials Today* **2011**, *14*, 496–501.
- [69] others., *et al.* Ultrasensitive strain sensors made from metal-coated carbon nanofiller/epoxy composites. *Carbon* **2013**, *51*, 202–212.
- [70] Lou, Y.; Liu, G.; Liu, S.; Shen, J.; Jin, W. A facile way to prepare ceramic-supported graphene oxide composite membrane via silane-graft modification. *Applied surface science* **2014**, *307*, 631–637.
- [71] Zhan, G.-D.; Kuntz, J. D.; Wan, J.; Mukherjee, A. K. Single-wall carbon nanotubes as attractive toughening agents in alumina-based nanocomposites. *Nature materials* **2003**, *2*, 38–42.
- [72] Peigney, A.; Garcia, F. L.; Estournes, C.; Weibel, A.; Laurent, C. Toughening and hardening in double-walled carbon nanotube/nanostructured magnesia composites. *Carbon* **2010**, *48*, 1952–1960.
- [73] Sun, J.; Gao, L.; Iwasa, M.; Nakayama, T.; Niihara, K. Failure investigation of carbon nanotube/3Y-TZP nanocomposites. *Ceramics International* **2005**, *31*, 1131–1134.
- [74] Wang, K.; Wang, Y.; Fan, Z.; Yan, J.; Wei, T. Preparation of graphene nanosheet/alumina composites by spark plasma sintering. *Materials Research Bulletin* **2011**, *46*, 315–318.

- [75] Lee, B.; Koo, M. Y.; Jin, S. H.; Kim, K. T.; Hong, S. H. Simultaneous strengthening and toughening of reduced graphene oxide/alumina composites fabricated by molecular-level mixing process. *Carbon* **2014**, *78*, 212–219.
- [76] Liu, J.; Yan, H.; Jiang, K. Mechanical properties of graphene platelet-reinforced alumina ceramic composites. *Ceramics International* **2013**, *39*, 6215–6221.
- [77] Wang, J.; Deng, S.; Liu, Z.; Liu, Z. The rare two-dimensional materials with Dirac cones. *National Science Review* **2015**, *2*, 22–39.
- [78] Lakshmanan, R.; Maulik, N. Graphene-based drug delivery systems in tissue engineering and nanomedicine. *Canadian journal of physiology and pharmacology* **2018**, *96*, 869–878.
- [79] Ramadoss, A.; Kim, S. J. Facile preparation and electrochemical characterization of graphene/ZnO nanocomposite for supercapacitor applications. *Materials Chemistry and Physics* **2013**, *140*, 405–411.
- [80] Lawal, A. T. Graphene-based nano composites and their applications. A review. *Biosensors and Bioelectronics* **2019**, *141*, 111384.
- [81] Jianguo, S.; Xinzhi, W.; Chang-Tang, C. Preparation and characterization of graphene oxide. *Journal of Nanomaterials* **2014**, 276143.
- [82] Chen, J.; Yao, B.; Li, C.; Shi, G. An improved Hummers method for eco-friendly synthesis of graphene oxide. *Carbon* **2013**, *64*, 225–229.
- [83] Lavin-Lopez, M. d. P.; Paton-Carrero, A.; Sanchez-Silva, L.; Valverde, J.; Romero, A. Influence of the reduction strategy in the synthesis of reduced graphene oxide. *Advanced Powder Technology* **2017**, *28*, 3195–3203.
- [84] Ganguly, A.; Sharma, S.; Papakonstantinou, P.; Hamilton, J. Probing the thermal deoxygenation of graphene oxide using high-resolution in situ X-ray-based spectroscopies. *The Journal of Physical Chemistry C* **2011**, *115*, 17009–17019.
- [85] Maharubin, S.; Zhang, X.; Zhu, F.; Zhang, H.-C.; Zhang, G.; Zhang, Y. Synthesis and applications of semiconducting graphene. *Journal of Nanomaterials* **2016**, 2016.

- [86] Dudina, D. V.; Mukherjee, A. K. Reactive spark plasma sintering: successes and challenges of nanomaterial synthesis. *Journal of Nanomaterials* **2013**, 2013.
- [87] Ullattil, S. G.; Periyat, P. *Sol-Gel Materials for Energy, Environment and Electronic Applications*; Springer, 2017; pp 271–283.
- [88] Carter, C. B.; Norton, M. G. *Ceramic Materials*; Springer, 2013; pp 411–422.
- [89] Riffat, S. B.; Qiu, G. A review of state-of-the-art aerogel applications in buildings. *International Journal of Low-Carbon Technologies* **2013**, 8, 1–6.
- [90] Hwang, G. L.; Hwang, K. C. Carbon nanotube reinforced ceramics. *Journal of Materials Chemistry* **2001**, 11, 1722–1725.
- [91] Shen, Z.; Johnsson, M.; Zhao, Z.; Nygren, M. Spark plasma sintering of alumina. *Journal of the American Ceramic Society* **2002**, 85, 1921–1927.
- [92] Tyrpekl, V.; Berkmann, C.; Holzhäuser, M.; Köpp, F.; Cologna, M.; Wangle, T.; Somers, J. Implementation of a spark plasma sintering facility in a hermetic glovebox for compaction of toxic, radiotoxic, and air sensitive materials. *Review of Scientific Instruments* **2015**, 86, 023904.
- [93] Cavaliere, P.; Sadeghi, B.; Shabani, A. *Spark Plasma Sintering of Materials*; Springer, 2019; pp 3–20.
- [94] Sun, S.-K.; Zhang, G.-J.; Wu, W.-W.; Liu, J.-X.; Suzuki, T.; Sakka, Y. Reactive spark plasma sintering of ZrC and HfC ceramics with fine microstructures. *Scripta Materialia* **2013**, 69, 139–142.
- [95] Kohli, R. *Developments in Surface Contamination and Cleaning*; Elsevier, 2012; pp 107–178.
- [96] Cullity, B. D. *Elements of X-ray Diffraction*; Addison-Wesley Publishing, 1956.
- [97] Suryanarayana, C.; Norton, M. G. *X-ray diffraction: a practical approach*; Springer Science & Business Media, 2013.

- [98] Vishwakarma, V.; Uthaman, S. *Smart Nanoconcretes and Cement-Based Materials*; Elsevier, 2020; pp 241–255.
- [99] Bragg, W. L. The diffraction of short electromagnetic waves by a crystal. **1929**,
- [100] Vacuum, T. Thermogravimetric Analysis. **2019**,
- [101] Zainal, N. F. A.; Saiter, J. M.; Halim, S. I. A.; Lucas, R.; Chan, C. H. Thermal analysis: basic concept of differential scanning calorimetry and thermogravimetry for beginners. *Chemistry Teacher International* **2020**, *1*.
- [102] Prime, R. B.; Bair, H. E.; Vyazovkin, S.; Gallagher, P. K.; Riga, A. Thermogravimetric analysis (TGA). *Thermal analysis of polymers: Fundamentals and applications* **2009**, 241–317.
- [103] Sing, K. S. Physisorption of nitrogen by porous materials. *Journal of Porous Materials* **1995**, *2*, 5–8.
- [104] others,, *et al.* On the use and abuse of N₂ physisorption for the characterization of the pore structure of shales. 2016.
- [105] Biran, A.; Pulido, R. L. *Ship hydrostatics and stability*; Butterworth-Heinemann, 2013.
- [106] Cruz, N. *Autonomous underwater vehicles*; BoD–Books on Demand, 2011.
- [107] Weibel, A.; Flaureau, A.; Pham, A.; Chevallier, G.; Esvan, J.; Estournès, C.; Laurent, C. One-step synthesis of few-layered-graphene/alumina powders for strong and tough composites with high electrical conductivity. *Journal of the European Ceramic Society* **2020**, *40*, 5779–5789.
- [108] de Terris, T.; Andreau, O.; Peyre, P.; Adamski, F.; Koutiri, I.; Gorny, C.; Dupuy, C. Optimization and comparison of porosity rate measurement methods of Selective Laser Melted metallic parts. *Additive Manufacturing* **2019**, *28*, 802–813.
- [109] Jin, W.; Xu, W.; Liang, H.; Li, Y.; Liu, S.; Li, B. *Emulsions*; Elsevier, 2016; pp 1–36.

- [110] Ferreira, L. M.; Cervi, V. F.; Gehrcke, M.; da Silveira, E. F.; Azambuja, J. H.; Braganhol, E.; Sari, M. H.; Zborowski, V. A.; Nogueira, C. W.; Cruz, L. Ketoprofen-loaded pomegranate seed oil nanoemulsion stabilized by pullulan: selective antiglioma formulation for intravenous administration. *Colloids and Surfaces B: Biointerfaces* **2015**, *130*, 272–277.
- [111] Zhou, W.; Apkarian, R.; Wang, Z. L.; Joy, D. *Scanning microscopy for nanotechnology*; Springer, 2006; pp 1–40.
- [112] Raval, N.; Maheshwari, R.; Kalyane, D.; Youngren-Ortiz, S. R.; Chougule, M. B.; Tekade, R. K. *Basic Fundamentals Of Drug Delivery*; Elsevier, 2019; pp 369–400.
- [113] Stokes, D. *Principles and practice of variable pressure/environmental scanning electron microscopy (VP-ESEM)*; John Wiley & Sons, 2008.
- [114] Pendse, D.; Chin, A. Cathodoluminescence and Transmission Cathodoluminescence. **2001**,
- [115] Vernon-Parry, K. Scanning electron microscopy: an introduction. *III-Vs Review* **2000**, *13*, 40–44.
- [116] Chen, W.; Wang, J.; Wan, F.; Wang, P. Review of optical fibre sensors for electrical equipment characteristic state parameters detection. *High Voltage* **2019**, *4*, 271–281.
- [117] Long, D. A. Raman spectroscopy. *New York* **1977**, 1–12.
- [118] Malard, L.; Pimenta, M. A.; Dresselhaus, G.; Dresselhaus, M. Raman spectroscopy in graphene. *Physics reports* **2009**, *473*, 51–87.
- [119] others., *et al.* Raman spectroscopy of graphene and related materials. *New developments in photon and materials research* **2013**, *1*, 1–20.
- [120] Hertz, H. Ueber einen Einfluss des ultravioletten Lichtes auf die electrische Entladung. *Annalen der Physik* **1887**, *267*, 983–1000.
- [121] Einstein, A. On a heuristic point of view concerning the production and transformation of light. *Annalen der Physik* **1905**, 1–18.

- [122] Chastain, J.; King Jr, R. C. Handbook of X-ray photoelectron spectroscopy. *Perkin-Elmer Corporation* **1992**, *40*, 221.
- [123] Moulder, J. F.; Stickle, W. F.; Sobol, P. E.; Bomben, K. D. Handbook of X-ray photoelectron spectroscopy: a reference book of standard spectra for identification and interpretation of XPS data; Physical Electronics: Eden Prairie, MN, 1995. *Google Scholar There is no corresponding record for this reference* **2000**,
- [124] Okpalugo, T.; Papakonstantinou, P.; Murphy, H.; McLaughlin, J.; Brown, N. High resolution XPS characterization of chemical functionalised MWCNTs and SWCNTs. *Carbon* **2005**, *43*, 153–161.
- [125] Quinn, G. D.; Bradt, R. C. On the Vickers indentation fracture toughness test. *Journal of the American Ceramic Society* **2007**, *90*, 673–680.
- [126] Giannakopoulos, A.; Larsson, P.-L.; Vestergaard, R. Analysis of Vickers indentation. *International journal of solids and structures* **1994**, *31*, 2679–2708.
- [127] Quinn, G. D. Fracture toughness of ceramics by the Vickers indentation crack length method: a critical review. 2007.
- [128] Zhang, L.; He, Y.; Feng, S.; Zhang, L.; Jiao, Z.; Zhan, Y.; Wang, Y. Preparation and tribological properties of novel boehmite/graphene oxide nano-hybrid. *Ceramics International* **2016**, *42*, 6178–6186.
- [129] Ban, F.; Majid, S.; Huang, N.; Lim, H. Graphene oxide and its electrochemical performance. *Int. J. Electrochem. Sci* **2012**, *7*, 4345–4351.
- [130] Feret, F. R.; Roy, D.; Boulanger, C. Determination of alpha and beta alumina in ceramic alumina by X-ray diffraction. *Spectrochimica Acta Part B: Atomic Spectroscopy* **2000**, *55*, 1051–1061.
- [131] Caiut, J.; Floch, N.; Messaddeq, Y.; Lima, O. J. d.; Rocha, L. A.; Ciuffi, K. J.; Nassar, E. J.; Friedermann, G. R.; Ribeiro, S. J. Cr³⁺ doped Al₂O₃ obtained by non-hydrolytic sol-gel methodology. *Journal of the Brazilian Chemical Society* **2019**, *30*, 744–751.

- [132] Kim, S.-M.; Lee, Y.-J.; Jun, K.-W.; Park, J.-Y.; Potdar, H. Synthesis of thermo-stable high surface area alumina powder from sol–gel derived boehmite. *Materials Chemistry and Physics* **2007**, *104*, 56–61.
- [133] Surekha, G.; Krishnaiah, K. V.; Ravi, N.; Suvarna, R. P. FTIR, Raman and XRD analysis of graphene oxide films prepared by modified Hummers method. 2020.
- [134] Kumar, C. S.; Hareesh, U.; Damodaran, A.; Warriar, K. Monohydroxy aluminium oxide (Boehmite, AlOOH) as a reactive binder for extrusion of alumina ceramics. *Journal of the European Ceramic Society* **1997**, *17*, 1167–1172.
- [135] Viswabaskaran, V.; Gnanam, F.; Balasubramanian, M. Mullitisation behaviour of calcined clay–alumina mixtures. *Ceramics International* **2003**, *29*, 561–571.
- [136] Guerrero-Fajardo, C. A.; Giraldo, L.; Moreno-Piraján, J. C. Graphene Oxide: Study of Pore Size Distribution and Surface Chemistry Using Immersion Calorimetry. *Nanomaterials* **2020**, *10*, 1492.
- [137] Segal, F. M.; Correa, M. F.; Bacani, R.; Castanheira, B.; Politi, M. J.; Brochsztain, S.; Triboni, E. R. A novel synthesis route of mesoporous γ -alumina from polyoxohydroxide aluminum. *Materials Research* **2018**, *21*.
- [138] Cardarelli, F. Ceramics, refractories, and glasses. *Materials handbook: a concise desktop reference* **2008**, 593–689.
- [139] Yalamaç, E.; Trapani, A.; Akkurt, S. Sintering and microstructural investigation of gamma–alpha alumina powders. *Engineering Science and Technology, an International Journal* **2014**, *17*, 2–7.
- [140] Shah, W.; Luo, X.; Guo, C.; Rabiou, B.; Huang, B.; Yang, Y. Preparation and mechanical properties of graphene-reinforced alumina-matrix composites. *Chemical Physics Letters* **2020**, *754*, 137765.
- [141] Deng, S.; Berry, V. Wrinkled, rippled and crumpled graphene: an overview of formation mechanism, electronic properties, and applications. *Materials Today* **2016**, *19*, 197–212.

- [142] Cygan, T.; Wozniak, J.; Kostecki, M.; Petrus, M.; Jastrzębska, A.; Ziemkowska, W.; Olszyna, A. Mechanical properties of graphene oxide reinforced alumina matrix composites. *Ceramics International* **2017**, *43*, 6180–6186.
- [143] Narvaez-Muñoz, C. P.; Carrion-Matamoros, L. M.; Vizuete, K.; Debut, A.; Arroyo, C. R.; Guerrero, V.; Almeida-Naranjo, C. E.; Morales-Flórez, V.; Mowbray, D. J.; Zamora-Ledezma, C. Tailoring organic–organic poly (vinylpyrrolidone) microparticles and fibers with multiwalled carbon nanotubes for reinforced composites. *ACS Applied Nano Materials* **2019**, *2*, 4302–4312.
- [144] others,, *et al.* Characterizing graphene with Raman spectroscopy. *Thermo fisher scientific* **2010**, 51946.
- [145] López-Díaz, D.; Lopez Holgado, M.; García-Fierro, J. L.; Velazquez, M. M. Evolution of the Raman spectrum with the chemical composition of graphene oxide. *The Journal of Physical Chemistry C* **2017**, *121*, 20489–20497.
- [146] Ferrari, A. C. Raman spectroscopy of graphene and graphite: Disorder, electron–phonon coupling, doping and nonadiabatic effects. *Solid state communications* **2007**, *143*, 47–57.
- [147] Lyon, K.; Preciado-Rivas, M. R.; Zamora-Ledezma, C.; Despoja, V.; Mowbray, D. J. LCAO-TDDFT- k - ω : spectroscopy in the optical limit. *Journal of Physics: Condensed Matter* **2020**, *32*, 415901.
- [148] Doss, C.; Zallen, R. Raman studies of sol-gel alumina: finite-size effects in nanocrystalline AlO (OH). *Physical Review B* **1993**, *48*, 15626.
- [149] Tuschel, D. Photoluminescence spectroscopy using a Raman spectrometer. *Spectroscopy* **2016**, *31*, 14–21.
- [150] Hakkar, S.; Achache, S.; Sanchette, F.; Mekhalif, Z.; Kamoun, N.; Boumaza, A. Characterization by Photoluminescence and Raman Spectroscopy of the Oxide Scales Grown on the PM2000 at High Temperatures. *Journal of Molecular and Engineering Materials* **2019**, *7*, 1950003.

- [151] Wall, M. The Raman spectroscopy of graphene and the determination of layer thickness. *Thermo Sci* **2011**, *5*.
- [152] Krishnamoorthy, K.; Jeyasubramanian, K.; Premanathan, M.; Subbiah, G.; Shin, H. S.; Kim, S. J. Graphene oxide nanopaint. *Carbon* **2014**, *72*, 328–337.
- [153] Sun, J.; Gao, L.; Jin, X. Reinforcement of alumina matrix with multi-walled carbon nanotubes. *Ceramics international* **2005**, *31*, 893–896.
- [154] Zhou, M.; Lin, T.; Huang, F.; Zhong, Y.; Wang, Z.; Tang, Y.; Bi, H.; Wan, D.; Lin, J. Highly conductive porous graphene/ceramic composites for heat transfer and thermal energy storage. *Advanced Functional Materials* **2013**, *23*, 2263–2269.
- [155] Lee, J. S.; Kim, H. S.; Park, N.-K.; Lee, T. J.; Kang, M. Low temperature synthesis of α -alumina from aluminum hydroxide hydrothermally synthesized using $[\text{Al}(\text{C}_2\text{O}_4)_x(\text{OH})_y]$ complexes. *Chemical engineering journal* **2013**, *230*, 351–360.
- [156] Hu, L.; Wang, W.; He, Q.; Wang, A.; Liu, C.; Tian, T.; Wang, H.; Fu, Z. Preparation and characterization of reduced graphene oxide-reinforced boron carbide ceramics by self-assembly polymerization and spark plasma sintering. *Journal of the European Ceramic Society* **2020**, *40*, 612–621.
- [157] Ingram-Jones, V. J.; Slade, R. C.; Davies, T. W.; Southern, J. C.; Salvador, S. Dehydroxylation sequences of gibbsite and boehmite: study of differences between soak and flash calcination and of particle-size effects. *Journal of Materials Chemistry* **1996**, *6*, 73–79.
- [158] Narula, C. K.; Weber, W. H.; Ying, J. Y.; Allard, L. F. Incorporation of lanthanides in alumina matrices by a sol–gel process employing heterometallic alkoxides, $M[\text{Al}(\text{OPr}i)_4]_3$, as precursors. *Journal of Materials Chemistry* **1997**, *7*, 1821–1829.
- [159] Zhang, X.; An, Y.; Han, J.; Han, W.; Zhao, G.; Jin, X. Graphene nanosheet reinforced ZrB₂–SiC ceramic composite by thermal reduction of graphene oxide. *Rsc Advances* **2015**, *5*, 47060–47065.